Ion Beam Modifications of Boron Nitride By Ion Implantation

Ronald Machaka

A dissertation submitted in fulfillment of the requirements for the
Master of Science in Material Science Physics degree to the Faculty of Science,
University of the Witwatersrand, Johannesburg.

2006

THE WORK CONTAINS NO MATERIAL WHICH HAS BEEN ACCEPTED FOR THE AWARD FOR ANY OTHER DEGREE OR DIPLOMA IN ANY UNIVERSITY OR ANY OTHER TERTIARY INSTITUTION AND, TO THE BEST OF MY KNOWLEDGE AND BELIEF, CONTAINS NO MATERIAL PREVIOUSLY PUBLISHED OR WRITTEN BY ANY OTHER PERSON, EXCEPT WHERE DUE REFERENCE HAS BEEN MADE IN THE TEXT.

I GIVE CONSENT TO THIS COPY OF MY THESIS, WHEN DEPOSITED IN THE UNIVERSITY LIBRARY, BEING AVAILABLE FOR LOAN AND PHOTOCOPYING.

SIGNED:

RONALD MACHAKA

(MAY 23, 2007)

to my caring and supportive father Renwell ndatenda...

Acknowledgements

Like in any case, the list may not be exhaustive yet many people took some time off their busy lives to share ideas, discuss their own experiences, and review many drafts of this document. I wish to thank my supervisor and mentor, Prof TE Derry, by far the greatest immediate influence on the thesis for recommending this research area and for his untiring and enthusiastic supervision throughout the project. Prof JE Lowther, Dr TE Mosuang, and Dr VL Solozhenko for generously sharing their publications with me. I wish to thank N Makau and G Amolo for the numerous stimulating discussions, for their assistance with various experimental and theoretical aspects of this work from the planning to the analysis of data. I am also very grateful for the support and advice I got from M Madhuku. I wish to thank Prof JD Comins, R Erasmus, B Mathe, and C Sumanya for making the Raman measurements and SBS measurements possible. I extend my gratitude to R Erasmus for his patience with my samples, for kindly cooperation on both experiments and co-authoring a few publications. Your comments were so valuable that most of them I could not resist incorporating in this document. I wish to thank N Jackson for helping me with the ion implantations and Raman measurements for the energies between 200 keV and 850 keV. I wish to thank Dr D Billing, Prof L Shonin, and W Matiza for their assistance with the XRD measurements. I am indebted to Prof M Witcomb and his staff for helping with the SEM measurements. I wish to thank M Rebak for the precision work and for providing the hexagonal boron nitride samples that were used in the preliminary studies. I wish to thank the staff at iThemba LABS, CoE in Strong Materials, the School of Physics, and fellow postgraduate students: Clemence, Emmanuel, Kuda, Masimba, Roy, and Naison for their support. I am grateful to my parents, CoE in Strong Materials, iThemba LABS (Gauteng), and the School of Physics for their financial assistance. I wish attribute the completion of this work to the moral support, and the unbelievable understanding of those closest and dearest to me; my parents, my wife Sibu, brothers - Lee and Stan, and sisters - Jane, Sylvia, and Pipi.

Ndatenda!

Abstract

The search for alternative methods of synthesizing cubic boron nitride (*c*BN), one of the hardest known materials, at low thermo-baric conditions has stimulated considerable research interest due to its great potential for numerous practical industrial applications. The practical applications are motivated by the material's amazing combination of extraordinarily superior properties. The *c*BN phase is presently being synthesized from graphite-like boron nitride modifications at high thermo-baric conditions in the presence of catalytic solvents or by ion–beam assisted (chemical and physical) deposition methods. However, the potential and performance of *c*BN have not been fully realized largely due to central problems arising from the aforementioned synthesis methods.

The work reported in this dissertation is inspired by the extensive theoretical investigation of the influence of defects in affecting the transformation of the hexagonal boron nitride (*h*BN) phase to the *c*BN phase that was carried out by Mosuang and Lowther (*Phys Rev B* ***66****, 014112* (2002)). From their investigation, using an *ab-initio* local density approach, for the B, C, N, and O simple defects in *h*BN, they concluded that the defects introduced into *h*BN could facilitate a low activation–energy hexagonal-to-cubic boron nitride phase transformation, under less extreme conditions.

We use ion implantation as a technique of choice for introducing 'controlled' defects into the hot–pressed polycrystalline 99.9% *h*BN powder samples. The reasons are that the technique is non–equilibrium (not influenced by diffusion laws) and controllable, that is the species of ions, their energy and number introduced per unit area can be changed and monitored easily. We investigate the structural modifications of *h*BN by ion implantation. Emphasis is given to the possibilities of influencing a low activation–energy *h*BN-to-*c*BN phase transformation. The characterization of the structural modifications induced to the *h*BN samples by implanting with He^+ ions of energies ranging between 200 keV and 1.2 MeV, at fluences of up to 1.0×10^{17} ions·cm^{-2}, was accomplished by correlating results from X-Ray Diffraction (XRD), micro-Raman (μ-Raman) spectroscopy measurements, and two-dimensional X-Y Raman (2D-Raman) mapping measurements. The surface to-

pography of the samples was investigated using Scanning Electron Microscopy (SEM). Efforts to use Surface Brillouin Scattering (SBS) were hampered by the transparency of the samples to the laser light as well as the large degree of surface roughness. All the implantations were carried out at room temperature under high vacuum.

2D-Raman mapping and μ-Raman spectroscopy measurements done before and after He^+ ion irradiation show that an induced *h*BN-to-*c*BN phase transformation is possible: nanocrystals of *c*BN have been observed to have nucleated as a consequence of ion implantation, the extent of which is dictated by the fluences of implantation. The deviation of the measured spectra from the Raman spectra of single crystal *c*BN is expected, has been observed before and been attributed to phonon confinement effects. Also observed are phase transformations from the pre-existing *h*BN modification to: (a) the amorphous boron nitride (*a*BN), (b) the rhombohedral boron nitride (*r*BN) modifications, (c) crystalline and amorphous boron clusters, which are a result of the agglomeration of elementary boron during and immediately after ion implantation. These transformations were observed at high energies. Unfortunately, the XRD measurements carried out could not complement the Raman spectroscopy outcomes probably because the respective amounts of the transformed materials were well below the detection limit of the instrument used in the former case.

Nomenclature

BN	boron nitride
*a*BN	amorphous boron nitride
*c*BN	cubic boron nitride
n-*c*BN	nanocrystalline cubic boron nitride
*h*BN	hexagonal boron nitride
*r*BN	rhombohedral boron nitride
*w*BN	wurtzite boron nitride
*t*BN	turbostratic boron nitride
HPHT	high pressure and high temperature
dE	energy lost by an ion traversing in matter
dx	distance traversed
S	stopping power (subscripts t, n & e denote total, nuclear & electronic, respectively)
N	number of scattering elements
σ	scattering cross sections
x	depth in matter
$n(x)$	density of implants/implanted species
ϕ	dose, fluence, or the number of ions per unit area
R_p	mean projected range
ΔR_p	average deviation in R_p
E_d	displacement energy
G	Gibbs free energy
U	internal energy
p	pressure
V	volume
T	absolute temperature
S	entropy

PVD	physical vapour deposition
CVD	chemical vapour deposition
μ-RS	micro-Raman spectroscopy
2D-RS	two-dimensional X-Y Raman mapping/spectroscopy
XRD	X-ray diffraction
GIXRD	glancing/grazing incidence angle XRD
SBS	surface Brillouin scattering/spectroscopy
SEM	scanning electron microscopy
He^+	alpha particles
H^+	proton particles
TRIM	transport of ions in matter
m/q	mass–charge ratio
CCD	charge coupled detector
d-spacing	lattice plane separation
hkl	Miller index
FWHM	Full Width at Half Maximum
FPI	Fabry–Perot Interferometer
$\theta - 2\theta$	XRD scattering geometry
TO	transverse–optical phonon mode
LO	longitudinal–optical phonon mode
$\vec{E}_{inc}$	incident/exciting electromagnetic wave
ν_n	vibrational frequency of a vibrational state n
ξ_k	normal coordinate of a molecular vibration
ω_k	normal frequency of a normal vibration
$\vec{q}_k$	wavevector
$\vec{r}$	position vector
ω_i	frequency of the exciting source
μ_i	induced dipole moment
$\tilde{\alpha}_{ij}$	polarizability tensor

Contents

List of Figures

List of Tables

Chapter 1

Introduction

1.1 Motivation

The amazing combination of superior mechanical, physical, chemical, optical, electronic and thermal properties of cubic boron nitride (*c*BN) makes it a very useful and promising material for a wide variety of industrial applications and has stimulated considerable academic interest. This promise has driven research on *c*BN for over 50 years. As a result the material has found many applications that include being used as an abrasive material (grinding and polishing) and in high temperature semiconductor devices (owing to the high thermal and hardness values) as well as in photonic devices (owing to the wide bandgap).

*c*BN was first synthesized by Wentorf Jr. in 1956 under extreme high pressure and high temperature (HPHT) conditions by and since then efforts have been made to synthesize this material at relatively low pressures (relative to those used in the direct HPHT synthesis methods) in order to make the process more commercially viable and therefore be of practical use to industry. The synthesis of *c*BN and other diamond-like phases is normally done under HPHT conditions though the catalytic method is presently the main method of obtaining *c*BN on an industrial scale.

The recent situation in the search for new superhard materials indicates that the synthesis of materials with hardness exceeding that of diamond is unlikely. Research has therefore been refocused on the search for new superhard phases to synthesize materials more useful than diamond, rather than harder than diamond. Research has also been refocused to finding more 'practical' ways to synthesize the existing and new materials for industrial use.

In the research work carried out by Mosuang and Lowther on the influence of defects in affecting the transformation of *h*BN to *c*BN investigated using the *ab-initio* local density approach for the simple defects B, C, N, and O, the results suggested that defects introduced in the hexagonal phase could facilitate a transformation to the cubic phase. The work reported herein seeks to investigate experimentally the possibility of using ion implantation as a technique of influencing the structural transformation from the soft hexagonal boron nitride phase to the ultrahard cubic phase of boron nitride under less extreme conditions of temperature and pressure. Raman spectroscopy and X-ray diffraction are the main experimental techniques used to characterize the irradiated materials. Scanning electron microscopy and surface Brillouin scattering were also used to reveal the nature of the sample surfaces.

1.2 Thesis Outline

This thesis is organized as follows: Chapter 2 gives an overview of the principles that govern and characterize the transport of energetic ions propagating in matter. The chapter also includes the stopping mechanisms and the resultant disruption of the pre-existing lattice structure caused by the ions as they come to rest. A detailed treatment of the material under investigation, boron nitride, is given in Chapter 3. The phase diagram, the structures and physico-chemical properties of the hexagonal and cubic phases, the synthesis of *c*BN, as well as the mechanisms underlining the hexagonal to cubic phase transformations are also discussed. Chapter 4 describes the experimental details; this includes the theory of the experimental techniques employed, the experimental setups including the methods and practices of the respective techniques. Chapter 5 discusses and analyses the results obtained from performing the experimental techniques and methods described in Chapter 4. Chapter 6 summarized the results obtained and discussed in Chapter 5 whilst Chapter 6 concludes the research and also goes as far as suggesting routes to future work. In Appendix A, the theory of the Raman scattering process is discussed.

Chapter 2

Principles of Ion Implantation

2.1 Introduction

The surface layer of a solid material plays a participatory role in all the material's interactions with its external environment for example in friction, wear, oxidation, fatigue, impact among others, therefore the industrial applications of most materials are largely dependent on their surface characteristics.

Ion implantation is a harsh and non–equilibrium technique of modifying the structural, physical and chemical characteristics of thin films, and surface layer properties of solid state materials, to depths of less than a micrometre [1]. It is achieved by the bombardment of the solid material with high energy charged particles. Most of the implants will come to rest within a shallow layer of the host material, creating many point defects in the stopping process. It is the added atoms and/or the interactions of the created defects that changes the host material's properties. For example, nitrogen ion implantation into a wide range of materials improves their surface hardness and wear resistance, ion beams have been successfully used to synthesize new metastable phases of remarkable properties that are otherwise unattainable by any other technique thermodynamically, semiconductor material doping is a good example.

Ion implantation has been used in a wide variety of fields both as a powerful research tool for investigating solid state material processes and properties, and as a means of controllably modifying the electrical, physical, chemical, mechanical and optical properties of solid surfaces [2]. The method of introducing ions into a solid material requires high voltage equipment that can electrostatically accelerate the ions and direct them onto the target material. A detailed description of the ion implanter is given in the *Experimental*

Techniques chapter.

2.2 The Physics of Ion Implantation

2.2.1 Introduction

The passage of an energetic ion moving in matter is characterized by interplay of several scattering processes as a result of the Coulombic interactions of the projectile ions with the solid target's nuclei and electron clouds. These interaction mechanisms involve the transfer of momentum or energy, in some cases the transfer of charges between the interacting parties. The predominance and contribution of each of the several interaction processes is reflected by its respective interaction cross section.

This section focuses on the propagation and subsequent stopping processes of the energetic ions in the target material; ion implantation.

2.2.2 Ion Stopping in Matter

When an energetic ion is implanted into a target material, it rapidly decelerates; transferring its momentum to the target material's atoms and electrons. The ion will eventually come to rest at some depth below the surface [1]. This energy which is lost in a succession of Coulomb interactions between the projectile ion and the material in which it traverses is deposited to the atoms that make up the target material. These energy loss mechanisms have traditionally been separated into two distinct processes based on their characteristics and the energy regimes in which they are predominant; at high propagation velocities the *electronic energy loss mechanism* dominates the ion stopping, also known as electronic stopping or inelastic energy loss. At low propagation velocities the *nuclear energy mechanism* dominates, also known as nuclear stopping or the elastic energy loss mechanism [1, 3, 4, 5, 6, 7].

The other processes that are known to take place include the generation of phonons – leading to the local heating of the target material, charge exchange (between the projectile and the target nuclei), the sputtering and degradation of the target surface atoms, nuclear reactions, the emission of high energy radiation (bremsstrahlung and Cherenkov[§] radia-

[§]Is the radiation emitted by a charge moving faster than the local speed of light $\frac{c}{\eta}$ moving past a target atom in a medium, η is the refractive index of the medium. Sometimes spelt as Cerenkov. This effect reduces to bremsstrahlung if its speed is less than that of the local speed of light

tion) and the emission of other secondary particles such as Auger electrons [5]. These processes are characterized by very low scattering cross section as compared to nuclear and electronic interactions and are hence deemed negligible hereinafter.

The nuclear and electronic stopping criteria are normally quantified by their respective 'stopping powers' S, theoretical quantities given as the energy dE lost by an ion as it traversed a distance dx in matter. The arithmetic sum of the two stopping powers (nuclear stopping power S_n and electronic stopping power S_e) is called the total stopping power, S_t as in equation 2.1 [3, 8].

$$S_t = -\left[\left(\frac{dE}{dx}\right)_n + \left(\frac{dE}{dx}\right)_e\right] \tag{2.1}$$

The equation 2.2 shows how the total interaction cross section, σ_t, relates to the total stopping power of the material as well as the number of scattering centres in the target materials, N.

$$\sigma_t = -N\left[\left(\frac{dE}{dx}\right)_n + \left(\frac{dE}{dx}\right)_e\right] \tag{2.2}$$

This parameter is relevant only for computational purposes; in practice, the implant final penetration depth as well as the amount of lattice damage created as a result of the ion stopping in matter are of critical importance [3].

Electronic Energy Loss Mechanism

Electronic stopping is often dominant in the beginning of the incident ion's path in the implanted material, that is when the ion velocity is relatively high [1, 6] as illustrated in fig 2.1.

The electronic stopping arises from the inelastic interactions between the projectile ion nucleus (and its electrons) and the electrons of the target atoms. These interactions normally result in the excitations and at times ionization of the target atoms [7]. The slowing down can also be attributed to the "viscous drag" the projectile nucleus experiences when it interacts with the target atoms' cloud of electrons as a result of the electrostatic attractions of charges of opposite polarities [1]. Hence electronic stopping is also known as the inelastic energy loss mechanism.

At such high energies, and also taking into consideration the nature of the interactions, the cross section of any displacement is low, hence the passage of the ion at such energies is characterized by slight trajectory deflections, behaving like its 'ripping through' the

cloud of electrons. The variation of the electronic stopping power, S_e with energy, E (or velocity) in Region I depicted in fig 2.1 is given in equation 2.3 [9].

$$S_e \propto -E^{0.5} \tag{2.3}$$

The electronic stopping reaches a maximum at projectile velocities comparable to the Bohr velocities of the valency electrons of the target atoms (Region II). At relativistically high projectile velocities, in the Bethe – Bloch formalism, the electronic stopping decreases as the projectile is stripped of all its valence electrons, becomes smaller and virtually sees neither the target nuclei nor its sea of electrons [2, 3, 7] this is illustrated in fig 2.1. This region (III) is not covered in the present work.

Nuclear Energy Loss Mechanism

At the projectile ion's end-of-range, when the ion has slowed down significantly, the electronic stopping cross section becomes small and the duration which the projectile nucleus spends in the vicinity of each target nucleus also becomes sizable. As a result, the cross section of the binary nuclear collisions will become large and will start dominating the ion stopping process [9].

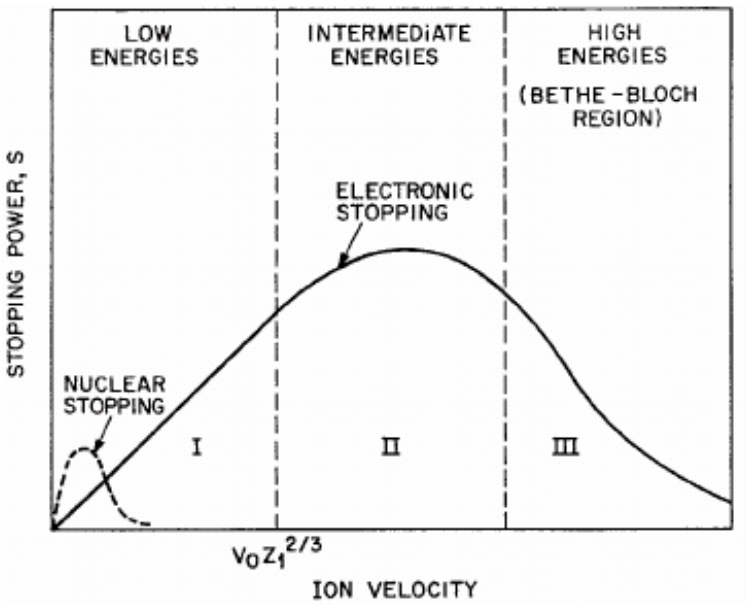

Figure 2.1: *Nuclear and electronic components of the ion stopping power as a function of ion velocity.*

The projectile ion and target nucleus interaction is generally considered a binary collision interaction between the two nuclei. The nuclear stopping power in this region (I) has an inverse square dependence on energy [3], as shown in equation 2.4 and fig 2.1.

$$S_n \propto -E^{-2} \tag{2.4}$$

These nuclear interactions involve large amounts of energy, much greater than the struck atom's lattice displacement energy E_d. This mechanism is therefore largely responsible for the massive disruption of the specimen lattice structure that follows ion irradiation.

Range and Range Distribution of Implants

The ion loses its energy in a series of random discrete collisions and subsequent ion deflections. Hence the energy loss process itself is a stochastic process. It therefore follows that the energy loss per collision, the total path length of penetration and the final density distribution of the implanted ions in matter also have a random variation from ion to ion.

In theory, the final density of implants $n(x)$, irrespective of the species, is statistically distributed as a function of the depth x and may be roughly approximated by a Gaussian distribution [2, 3, 4]. The parameters used to define this distribution are the mean projected range R_p, the average deviation from the mean projected range $\triangle R_p$ and the total number of ions per unit area ϕ. The implant density as a function of depth is then given by equation 2.5 below. The statistical parameters in equation 2.5 are illustrated schematically in fig 2.2.

$$n(x) = \frac{\phi}{\triangle R_p \sqrt{2\pi}} \cdot exp\left\{-\frac{(x - R_p)^2}{2 \cdot \triangle R_p^2}\right\} \tag{2.5}$$

2.2.3 Radiation Damage

After a series of inelastic electronic collisions and a few elastic knock–on collisions during the high energy regime of the ion trajectory, the projectile's momentum drops drastically. As the ion traverses in this low energy regime the nuclear stopping power which has an inverse square relationship with the ion energy becomes the dominant stopping mechanism as illustrated in equation 2.4 [3, 7]. This is because at low energies the

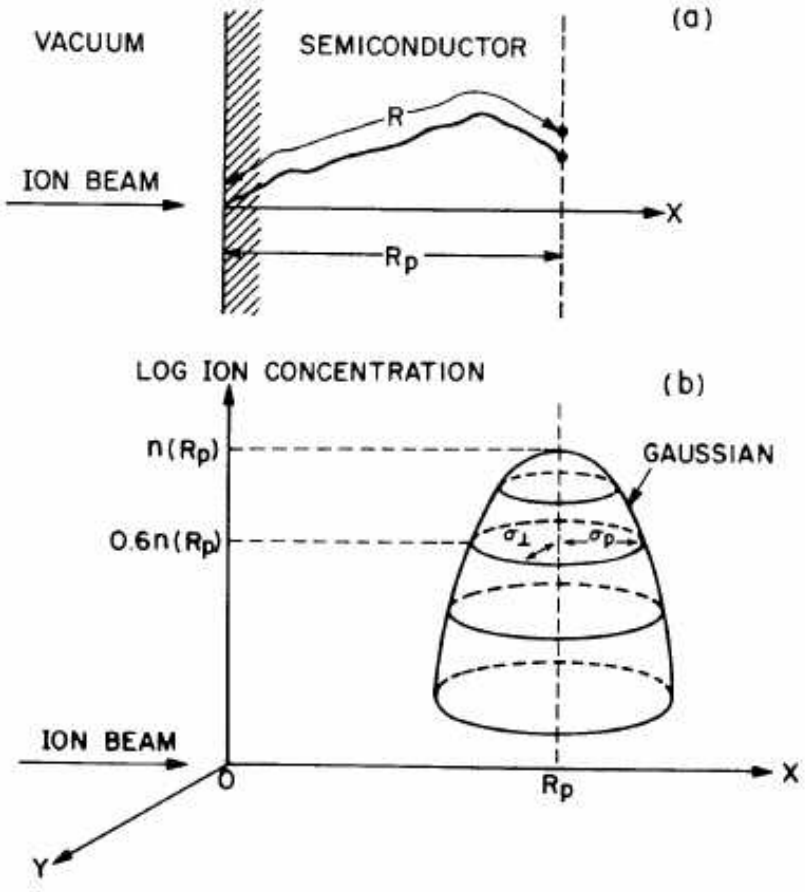

Figure 2.2: *A three dimensional distribution (depth and lateral) of the implant concentration with respect to the depth of the implanted material after [4].*

projectile spends more time in the vicinity of the target nuclei hence the cross section of ballistic nuclear collisions becomes greater.

The disruption of the preexisting lattice atomic arrangement as a result of the ion bombardment is what is known as *radiation damage*. The projectile ion embarks on vigorous displacement collisions with the target nuclei and if their energy is greater than the displacement energy of that material, E_d (which is the energy required to create a Frenkel pair that has a separation greater than the recombination radius, so inhibiting spontaneous recombination) then the target atom is dislodged from its lattice position leaving a vacancy site [10, 11]. The recoil atom, in turn, if it has recoil energy much greater than E_d will further cause the creation of Frenkel pairs. The result is a cascade of displacements in very short time duration (as compared to the time of flight of the projectile ion). This is known as a collision cascade and is characterized by a very large number of Frenkel

pair defects in a small volume surrounding the ion track, this phenomenon is known as a *displacement spike* which is an amorphous state [1, 6, 12, 13]. Fig 2.3 summarizes this phenomenon [6].

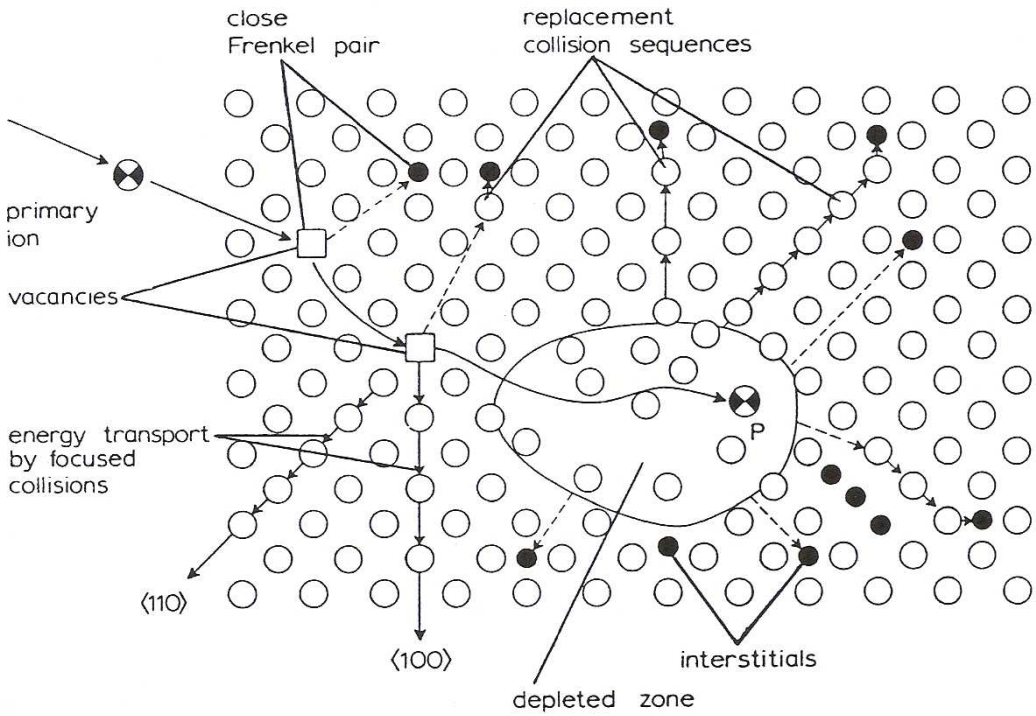

Figure 2.3: *A schematic representation of the collision cascade process showing the collision cascade and the focused collision sequence extending beyond the main cascade regime, after [6].*

However, if the ion or recoil energy drops below E_d, then the projectile is no longer capable of ejecting the target nuclei from their stable lattice positions. Instead they lose their energy through 'hard' collisions that induce large amplitude vibrations without leaving their lattice sites (which are essentially potential wells). The collision–induced vibration energy is shared by the neighbouring nuclei and appears as a source of heat. This region normally develops into a plasma–like structure; this structure develops rapidly ($\sim 10^{-12}$s) and is known as a *thermal spike*. This is one of the contributions to the sample heating during ion implantation [4]. Thermal spikes occur at the centre of displacement spikes; this region is also characterized by very high compressive stresses and high thermal energy [11].

The final damage configuration depends on the ion implantation conditions such as

the implantation dose, on the implantation temperature, on the properties of the target material, as well as on the massiveness (with respect to the target nuclei) and swiftness of the projectile ions [1, 14].

The point defects of the same sign (that is either interstitials or vacancies) may further interact during and after the ion implantation to form extended defects (disordered regions which extend over a large region of a solid) in the form of dislocation loops, grain boundaries, impurity clusters/agglomerations, crystalline/amorphous inclusions, voids or gaseous inclusions. Agglomeration proceeds by either diffusion/migration to other sites or annihilation by recombining with one another at defect recombination sites such as the surface or grain boundaries or other crystallographic extended defects that might act as defect sinks. Defects may also cluster to form extended defects in order to reduce the strain energy as well as the free energy of the system. Agglomeration is a transient process, the defect interactions are largely governed by the temperatures at which the implantation is done or at which the sample is annealed as well as the respective defect migration energies [5, 6, 15, 16].

When a typical group III-nitride material is implanted with gaseous ionic species, the atoms of the gaseous species, either the implants or nitrogen atoms from the nitride compound, have been observed to agglomerate to form gas molecules and subsequently a fine distribution of bubbles leading to the volume expansion of the sample; a good example is $N^+ \mapsto GaN$ [15, 17, 18]. However, ion implantation experiments of $F^+ \mapsto$ diamond under ambient temperature has also shown that the volume expansion can arise due to the agglomerations of interstitials and that the expansion is linearly proportional to the ion dose [19].

According to the studies on ‘point defect engineering’ in ion implanted diamond carried out by Derry and co–workers [16]; there exist different temperature regimes that govern the mobility of point defects in the damage cascade caused by the implanted ion. Generally at very low temperatures (typically less than 320K in diamond) all the point defects are immobile. At higher temperatures (typically between 320K and 800K in diamond) the interstitials become mobile whilst the vacancies remain immobile, whilst at even higher temperatures (typically greater than 800K in diamond) all the primary defects are mobile [16]. The general rule is that the mobility of the interstitials is larger than that of the vacancies. However, if the individual primary defects cluster and form secondary defect agglomerations or dislocation loops they become immobile and very stable even at high temperatures.

2.2.4 Channelling

So far, the discussion assumes that the implanted material is amorphous. In practice the crystal orientation influence on the ion penetration is called the *channelling effect*. When an ion beam is well aligned with a low–index crystallographic direction of a single crystal, for example ⟨100⟩ in *c*BN, there is a massive reduction in the yield of small impact–parameter interaction processes; hence few vigorous knock–on collisions [20, 21].

In amorphous materials the projectile interacts chaotically with the individual atoms in the material. On the contrary, the charged particles moving along axes or planes of symmetry of a crystal interact only with the nuclear planes or chains instead of the individual lattice atoms that constitute the planes. The ion beam in this case is not scattered chaotically but is instead gently and collectively steered by a succession of gentle lower energy–loss large impact–parameter collisions with 'walls' of atomic rows and planes that form the 'channels'. Hence the ion beam penetrates deeper into the sample than a similar ion traversing with the same energy but in an amorphous material [7, 9] as the probability of nuclear encounters is much less.

Chapter 3

Boron Nitride

3.1 Introduction

The compositional tetrahedron **B−C−N−Si** has stimulated considerable experimental and theoretical interests, one of the reasons being that it is within this system that most of the hardest known materials of superior chemical and physical properties are found. Such compounds include the hypothetical βC_3N_4, diamond (C), metastable boron carbonitride phases (BC_2N, BC_4N), cubic boron nitride (*c*BN) and silicon carbide (SiC) [22, 23].

The primary emphasis in this work is on *c*BN. Boron nitride (BN) is a binary compound of boron and nitrogen, the elements which straddle carbon in the periodic table of elements; this makes BN isoelectronic to carbon. However, there are significant differences in the properties of carbon and boron nitride, primarily due to the differences in chemical bonding: BN has mixed covalent and ionic bonding while bonding in carbon is completely covalent. As a result, both *h*BN and *c*BN have lower mechanical strength, thermal conductivity and Debye temperatures than their carbon counterparts, but larger lattice constants and energy bandgaps. There are practical differences between BN and carbon as well. *c*BN can be doped either n- or p-type, but diamond is readily doped only p-type. Both phases of boron nitride are more resistant to oxidation than their carbon counterparts, due to the formation of a non–volatile boron oxide [24].

Four primary crystalline polymorphic modifications of BN are known and are shown in Table 3.1: hexagonal boron nitride – *h*BN, rhombohedral boron nitride – *r*BN, cubic boron nitride – *c*BN and wurtzite boron nitride – *w*BN. These are analogous to graphite, rhombohedral graphite, diamond and hexagonal diamond respectively [25, 26, 27, 28, 29]. The *c*BN and *w*BN modifications are both hard, dense and diamond-like phases. They

are characterized by high density 3-dimensional sp^3 hybridized B — N bonds; these two phases however have different packing sequences of the closest packed diatomic planes and structural arrangements. The *r*BN and *h*BN are softer and graphite–like, having 2-dimensional sp^2 hybridized B — N bonds that form hexagonal-linked layers. Likewise the respective packing sequences of the two structures distinguish them [27, 29, 30].

Structural phase	*a*(Å)	*c*(Å)	Atomic positions
*h*BN	2.50	6.66	B: (0,0,0),($\frac{2}{3}$, $\frac{1}{3}$, $\frac{1}{2}$)
			N: ($\frac{2}{3}$, $\frac{1}{3}$,0),(0,0,$\frac{1}{2}$)
*r*BN	2.50	9.99	B: (0,0,0),($\frac{2}{3}$, $\frac{1}{3}$, $\frac{1}{3}$),($\frac{1}{2}$, $\frac{2}{3}$, $\frac{2}{3}$)
			N: ($\frac{2}{3}$, $\frac{1}{3}$,0),($\frac{1}{3}$, $\frac{2}{3}$, $\frac{1}{3}$),(0,0,$\frac{1}{2}$)
*c*BN	3.62	-	B: (0,0,0),($\frac{1}{2}$, $\frac{1}{2}$,0),(0,$\frac{1}{2}$, $\frac{1}{2}$),($\frac{1}{2}$,0,$\frac{1}{2}$)
			N: ($\frac{1}{4}$, $\frac{1}{4}$, $\frac{1}{4}$),($\frac{3}{4}$, $\frac{1}{4}$, $\frac{3}{4}$),($\frac{1}{4}$, $\frac{3}{4}$, $\frac{3}{4}$),($\frac{3}{4}$, $\frac{1}{4}$, $\frac{3}{4}$)
*w*BN	2.55	4.42	B: (0,0,0),($\frac{1}{3}$, $\frac{2}{3}$, $\frac{1}{2}$)
			N: (0,0,$\frac{3}{8}$),($\frac{1}{3}$, $\frac{2}{3}$, $\frac{7}{8}$)

Table 3.1: *Structural data for the boron nitride phases, after [30]. The structural diagrams of the four phases are also presented in [30].*

In addition to the crystalline phases, BN also exists in two disordered phases: turbostratic boron nitride – *t*BN, a partially disordered graphitic phase, with random stacking of the hexagonal sp^2 bonded basal layers, as well as an amorphous boron nitride phase – *a*BN, which is characterized by atomic level disorder [27, 28, 29].

The transformation of one structural phase into another is theoretically possible. This is as a result of the variety of polymorphic modifications that exist as brought about by the ability of BN to have a variety of local bonding. The progress of the structural phase transformation can however be hindered by the energy barrier of the respective transformation. As a result the transformation that follows is a result of the alteration that occurs to the atom–to–atom local bonding or the local electronic structure that accompanies the shearing of the planes in the transformed structure.

3.2 Phase Diagram of BN

A phase is a homogeneous portion of matter whose physico-chemical properties are similar throughout. The phase diagram of BN (fig 3.1) gives a graphical representation of the states and phases of equilibrium at any given pressure and temperature condition. The

underlying quantity which determines the stability of a phase is its Gibbs free energy, *G*, a thermodynamic function which is given by equation 3.1, where *p* is the pressure, *V* is the volume, *U* is the system's internal energy, *T* is the absolute temperature, and *S* is the system's entropy.

$$G = U + pV - TS \tag{3.1}$$

Given the conditions of high pressure the system shifts towards a stable and steric arrangement of low specific volume, to minimize its free energy. BN has many allotropic phases some of which are metastable in nature; for the purposes of this study, we are only interested in the stable *c*BN and *h*BN phases and their phase diagram.

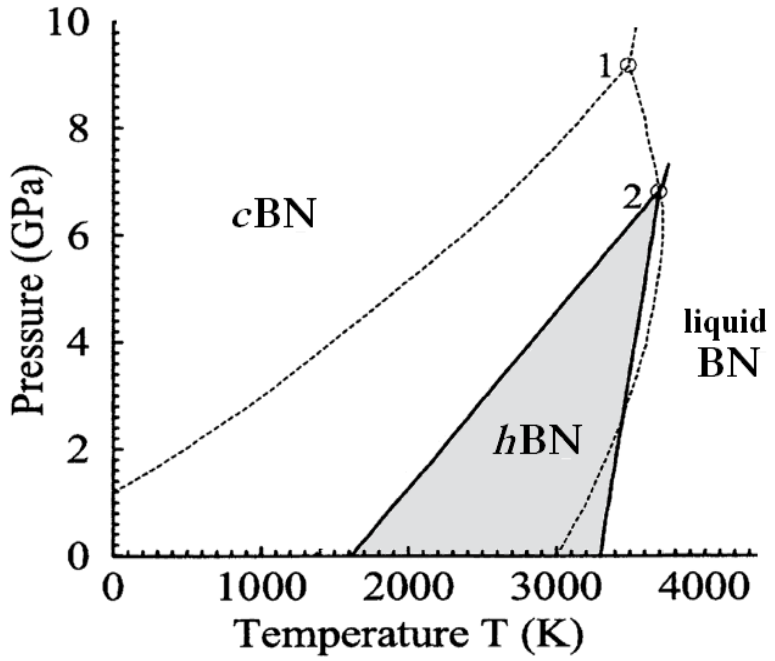

Figure 3.1: *The generally accepted phase diagram of boron nitride is shown in the solid line (1) and the dotted line (2) shows the Corrigan–Bundy phase diagram [31, 33]*

The equilibrium line of the *c*BN and *h*BN phases was determined by free energy calculations. The difference between the two phases' Gibbs free energies is zero where the two phases coexist [31, 32].

The phase diagram of BN that is shown in fig 3.1, shows that the low temperature region has a strikingly different form from that of carbon where diamond is metastable under ambient thermobaric conditions. Instead, the *c*BN phase is thermodynamically stable at temperatures up to 1600K, because the equilibrium line intersects the temperature

axis (and not the pressure axis slightly below 2GPa as previously conceived) at about 1570K [25, 33]. In addition to its thermostability at ambient conditions, as a result of *c*BN's low molar volume, it is characterized by a wide region of thermodynamic stability at high pressures, for this reason and its wide variety of superior properties it can be useful under extremely tough applications in engineering and in industry [34].

3.3 Hexagonal Boron Nitride

In their 2001 paper [35], Solozhenko and co-workers described *h*BN as: "The most commonly used form of boron nitride ... a basis for many advanced technologies."

3.3.1 The Structure of *h*BN

The *h*BN crystal structure is shown in fig 3.2. The *h*BN crystal lattice comprises flat or nearly flat basal planes formed by atoms arranged into a network of regular B_3N_3 hexagons or hexagonal rings. Each hexagonal ring has three boron atoms and three nitrogen atoms, with each boron atom bonded to three nitrogen atoms (nearest–neighbours) in the same plane. The hexagonal rings of the same layer are bonded through localized sp^2 hybridization while the adjacent layers are of relatively weaker bonding arising from the delocalized π orbitals [29].

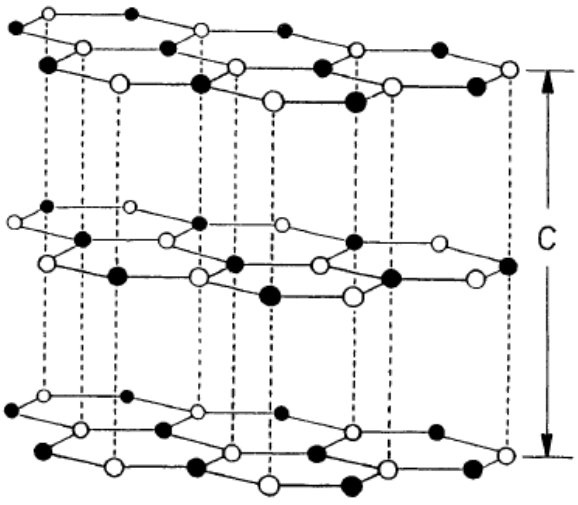

Figure 3.2: *The structure of hBN*

The basal planes are stacked in the *c*-direction in such a way that each hexagon (or

each boron atom) of layer A sits directly above the hexagon (or a nitrogen atom) of layer A′ in that fashion, hence the *h*BN is often denoted the AA′AA′ . . . stacking sequence (see fig 3.2) [28, 36, 37]. The A′ layer notation in *h*BN means that there is a 180° rotation in the atomic arrangements of the layer with respect to layer A, while graphite exhibits an ABAB. . . stacking sequence where only half the atoms in the basal layer A are sitting directly above the atoms in layer B, alternating in that fashion [30].

The *h*BN crystal structure has four atoms in its unit cell. X-ray diffraction data shows that there exist five possible *h*BN structures of different space groups. Among the five possible structures, the $P6_3/mmc$ structure is most commonly accepted one. It is possible for these five structures to be transformed into each other, by translational shearing of one BN basal layer relative to the other layer in the unit cell, or by rotating the BN basal layer around the *c*-axis of the crystal [27, 38].

The in–plane B — N distance is 0.145nm and the interlayer distance is 0.333nm [36, 37]. The *a* lattice parameter of *h*BN is greater than that of graphite whilst the *c* parameter is smaller; this reflects on the different bonding environments between the two compounds; Since the C — C bond is pure covalent it is much stronger and therefore shorter than the B — N bond; whilst the B — N bond is partially ionic and partially covalent, the intralayer (covalent bonding) interaction is reduced and the electrostatic interlayer interaction (Van der Waals interaction) strengthens and hence the interlayer distance *c* of *h*BN is shorter than that of graphite [39].

As a direct consequence of the nature of bonding and the crystal structure, *h*BN has been widely used in vacuum technology and in electronics because it is a good electrical insulator that also has a good thermal conductivity and thermal stability. It has applications in the nuclear energy industry and in research as a refractory material. It is as soft as graphite and hence has been used as a lubricant in many industries. It has been used in almost all the cases of *c*BN synthesis as a starting material or as a critical component of the precursor material.

3.4 Cubic Boron Nitride

Also known as borazon, sphalerite – BN or β BN; *c*BN crystallizes in the zincblende lattice structure [24]. The structure, shown in fig 3.3, has a cubic unit cell, containing four boron atoms and four nitrogen atoms. The position of the atoms within the unit cell is identical to the diamond crystal structure; both structures consist of two fcc sublattices,

offset by one quarter of the distance along a body diagonal (see also table 3.1). Each atom in the structure may be viewed as positioned at the centre of a tetrahedron, with its four nearest atomic neighbours defining the four corners of the tetrahedron; that is, the atoms in the structure are basically arranged in an sp^3 bonded 3-dimensional tetrahedral network of fourfold coordinated atoms. Each boron atom is tetrahedrally surrounded by, and covalently bonded to, four nitrogen atoms [40]. This structure has a lattice parameter of $a = 3.62$Å [40] and a density of $3.49 \text{g} \cdot \text{cm}^{-3}$ [28].

The lattice may also be envisioned as stacked layers of six-membered rings with each ring in the chair conformation, as shown in fig 3.3. In the cubic form, the layers of chairs are joined by staggered bonds and the six-membered rings between the chairs are also chairs. In the directions $\langle 100 \rangle$ the stacking sequence is ABC ABC ABC ... [40].

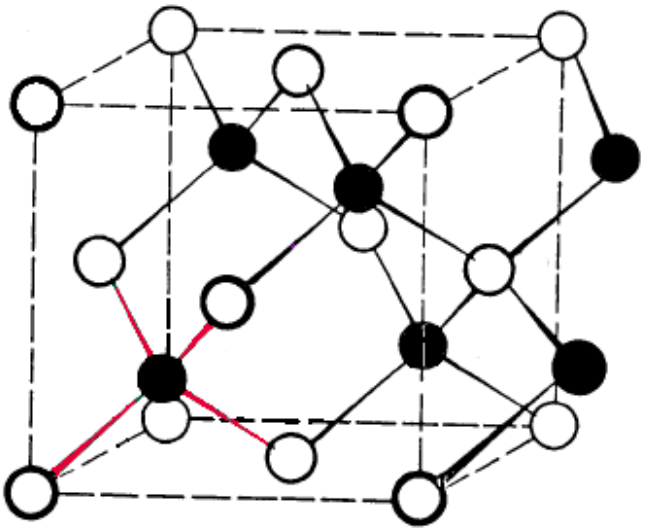

Figure 3.3: *The structure of cBN*

*c*BN has been shown, and has now been accepted generally as being the most thermodynamically stable phase of BN under ambient conditions as opposed to the earlier perception that the most stable phase was *h*BN [41, 42]. The general chemical trend is that if a material is able to form strong covalent bonds, a low coordination is favoured due to the Pauli exclusion and electrostatic repulsion between the bond charges. So since C — C is neutral carbon it is expected to be stable in the layered graphite structure. The bonding in BN is partially ionic and partially covalent so it turns out that the layered structure *h*BN is polar (attributed to the higher ionicity of the B — N bond) as compared to the *c*BN structure, thus *c*BN is the electrostatically favoured structure [43].

A summary of the general properties of *c*BN is given in Table 3.2, where the properties of *c*BN are compared to those of other superhard phases as well as GaAs a common group III – V compound. As a direct result of the bonding nature, *c*BN has a variety of useful properties that includes being the third hardest known material, a very high thermal and chemical stability, high melting temperature, a wide indirect bandgap, the second highest thermal conductivity and it is also the lightest known group III – V compound.

These properties make *c*BN very useful and promising in a wide variety of industrial applications. Its amazing combination of extraordinary mechanical, physical, chemical, optical, electronic and thermal properties make it desirable for use in cutting saws, drill tips, grinders, dies, and wear resistant coatings and a promising material in the semiconductor industry in applications such as diodes, heat conductors and heat sinks. Its light weight coupled with all the above mentioned properties makes it a possible candidate for space applications [49]. This promise has driven research on *c*BN for over the past 50 years, the major setback being that *c*BN does not occur naturally. Various methods have to be adopted to synthesize it.

3.4.1 Synthesis of *c*BN

There exist a variety of methods of synthesizing *c*BN from a variety of low–density modifications of BN. The low–density modification phases are normally derived from *h*BN by mechanical means such as ball–milling. The *h*BN itself is synthesized via the reductive nitridation of naturally occurring boron–based ores using urea–based compounds such as ammonia. In principle, these synthesis methods can be divided into direct and indirect synthesis methods [28]. Direct methods involve the use of single component low-dimensional *h*BN-like modifications as the starting materials to be subjected to the direct high pressure high temperature synthesis conditions. Most of the indirect methods make use of suitable catalyst–solvent systems (multicomponent) in the synthesis process. However, physical and chemical deposition methods are indirect but they do not make use of a catalytic solvent. Essentially, most of these methods make use of high thermobaric conditions.

Direct HPHT synthesis

This is the primary method of *c*BN synthesis through the direct solid state transformation of low-dimensional BN phases like *h*BN under HPHT conditions, the method was first used in 1956. Typical thermobaric conditions to achieve the transformation are

Properties of *c*BN	Values	Remarks and Possible Applications	References
Physical			
· density g·cm^{-3}	3.49	diamond: 3.52, SiC: 3.21, GaAs: 5.32; this makes *c*BN the lightest III – V compound;	[28, 44]
· lattice constant Å	3.62	diamond: 3.57, SiC: 4.36; (for *h*BN; *a*: 2.50 and *c*: 6.66)	[24, 44, 45]
Mechanical			
· Vicker's hardness GPa	60 – 75	diamond: 115, *c*BC_2N: 74, SiC: 39.8 finds numerous applications in abrasion	[28, 44, 46]
· Bulk modulus GPa	847	diamond: 1141, SiC: 130	[24, 44]
Chemical			
· reactivity	low	Oxidation resistant; Performs exceptionally well under very high temperatures; does not react with ferrous materials; wear resistant; a good machining media for hard materials; resistive to corrosive attach; non-toxic;	[28]
Electrical			
· resistivity $\times 10^9 \Omega$ cm	1 – 10	diamond: 10^7, GaAs:10^{-6}	[44]
· dielectric constant	4.10	diamond: 5.50, SiC: 9.60–10.0, GaAs: 12.5;	[44]
Optical			
· band-gap (eV)	6.1 – 6.4	diamond:5.45, SiC: 2.39–3.26, GaAs: 1.43 indirect band-gap; Possible blue light emission material for manufacturing junction and diodes;	[44, 47]
· Transparency		Optically transparent over a wide range of frequencies ; Ideal coating for optical sensors in rugged environments;	
Thermal			
· conductivity W/cm K	13	diamond: 20, SiC: 5; *c*BN is a superb heat sink;	[24, 28, 44]
· stability	high	Stable in air at temp. up to 1400 °C	[28, 48]
· linear expansion coefficient ($\times 10^6$ K$^-$) at 300K	1.15 – 1.9	diamond: 0.81	[24, 44]
· melting temperature	2967 °C	diamond: 3373K can sustain high temperature operations	[28]

Table 3.2: *The general properties cBN in comparison to other superhard materials, after [28, 44]*

$p = 12$GPa, $T = 2000$K [28, 50, 51]. This is a region in the BN phase diagram where the *c*BN is stable and the low dimensional BN phases are metastable. Even though the *c*BN phase is the most stable form of BN, a direct and spontaneous phase transformation from *h*BN to *c*BN is hindered by a very high activation energy barrier [28, 29]. For the same reasons, the thermobaric conditions at which a transformation can be achieved far exceed the phase diagram equilibrium conditions [34].

When a low dimensional BN modification (a thermodynamic system) is subjected to HPHT conditions, it is conceivable that the minimization of the Gibbs free energy of the system (equation 3.1) can easily be achieved by structural transformations that favour a reduction in the molar volume, which is feasible since *c*BN has a lower molar volume compared to low dimensional BN modifications; it therefore characterized by a wide region of thermodynamic stability at high pressures [34, 43].

However, compression alone will not achieve the desired solid state phase transformation. In principle, the change in the B — N bond dimensional order (from sp^2 to sp^3) proceeds by bond breaking and the subsequent bond reconstruction in order to change the bonding nature [28]. So in direct HPHT transformations, the high temperatures overcome the energy barrier of transformation whilst the pressure modifies the electronic and structural bond arrangement of the *h*BN material [52].

Indirect *c*BN Synthesis

The indirect synthesis method involves the use of multicomponent catalyst–solvent precursor material; the catalytic method is presently the main method of obtaining *c*BN at industrial scale. There also exist other indirect synthesis methods in which the starting material is not necessarily a multicomponent catalyst–solvent, for example ion beam assisted deposition methods where boron thin films are the starting materials.

For the past few years efforts have been made to synthesize this material at relatively low pressures (relative to those used in the direct HPHT synthesis methods) in order to make the process more commercially viable and therefore be of practical use to industry.

Catalytic Synthesis

It has been shown that the extreme thermobaric conditions used in direct synthesis methods can be reduced considerably by the use of different solvents or flux precursor materials. These solvents have been shown to affect the kinetics in catalytic ways. The *h*BN is partially dissolved into the flux precursor material forming a eutectic melt mixture;

when moderately high pressures and temperatures are applied to the eutectic composition, the formation of *c*BN crystallites proceeds as a precipitation from the supersaturated intermediate melt composition at slightly lower thermodynamic conditions (as shown on the phase diagram, see *Section 2.2: The Phase Diagram*), as a result of the differences in the solubilities of the eutectic melt composition at different pressures. The sizes of the crystallites depend on the temperature [28, 34] and the reaction kinetics.

The flux precursors are normally alkali and alkaline earth metal nitrides of general formula X_3N_2, the common ones being Mg_3N_2 which forms an Mg_3N_2-BN eutectic system. Some boron nitrides of alkali and alkaline earth metals have been shown to be great catalysts as well, for example Li_3BN_2, $Mg_3B_2N_4$ and $Ca_3B_2N_4$ [28, 34, 53]. Some alloys such as Fe–Al, Ni–Al, Mg–Al and Ag–Cd were also reported as effective catalyst-solvents for the *h*BN to *c*BN phase transformation; the Mg–Al alloy was found to be most effective and has practical utility as it can be handled in air without the use of any glove box [53].

The use of low ordered turbostratic and amorphous boron nitride as the starting materials instead of well crystallized highly ordered hexagonal boron nitride has also been extensively investigated, by JY Huang and co-workers [29, 49]; *c*BN formation could be observed at even lower *p,T* values. Water molecules adsorbed at the surface of the starting material have been observed to be having a catalytic effect in the transformation: the transformation at the surface has been observed to occur at much lower *p,V* conditions than the bulk of the material [28, 29, 49].

The use of some fluids in their supercritical state has been reported for the synthesis of *c*BN at reduced pressures. Singh and co-workers have used a number of liquids in supercritical state namely liquid ammonia, hydrazine and water, along with a number of conventional catalysts namely $MgB_2-Mg_3N_2$, Li_3N and AlN. They have observed spontaneous crystallization of *c*BN at pressures as low as 2GPa in *h*BN$-Li_3N-NH_3$ and *h*BN$-MgB_2-NH_3$ multicomponent systems [41, 53].

Ion Beam Assisted Deposition Synthesis

Ion beam assisted physical vapour deposition (PVD) and chemical vapour deposition (CVD) methods have also been used to synthesize *c*BN thin films *during film growth* at much lower pressure and temperature conditions. Generally, the ion assisted PVD methods used involve the surface bombardment of a supported boron thin film by energetic nitrogen or argon ions under evacuated conditions at room temperature. The films deposited in this way suffer poor adhesion to the substrate as well as cracking as a result

of the high compressive stresses induced by the energetic ions. The CVD methods involve chemical reactions of gaseous reactants on or near the vicinity of a heated substrate surface at atomic levels, making it possible to deposit single monolayers.

3.4.2 The *h*BN–to–*c*BN Phase Transformation

There are two possible mechanisms of direct transformation from low–density phases to the *c*BN phase, the diffusionless martensitic–type transformations involving well crystallized starting materials like *h*BN or *r*BN and the diffusional transformations involving amorphized or poorly crystallized starting materials, for example ball milled *h*BN or *a*BN [29, 49, 51].

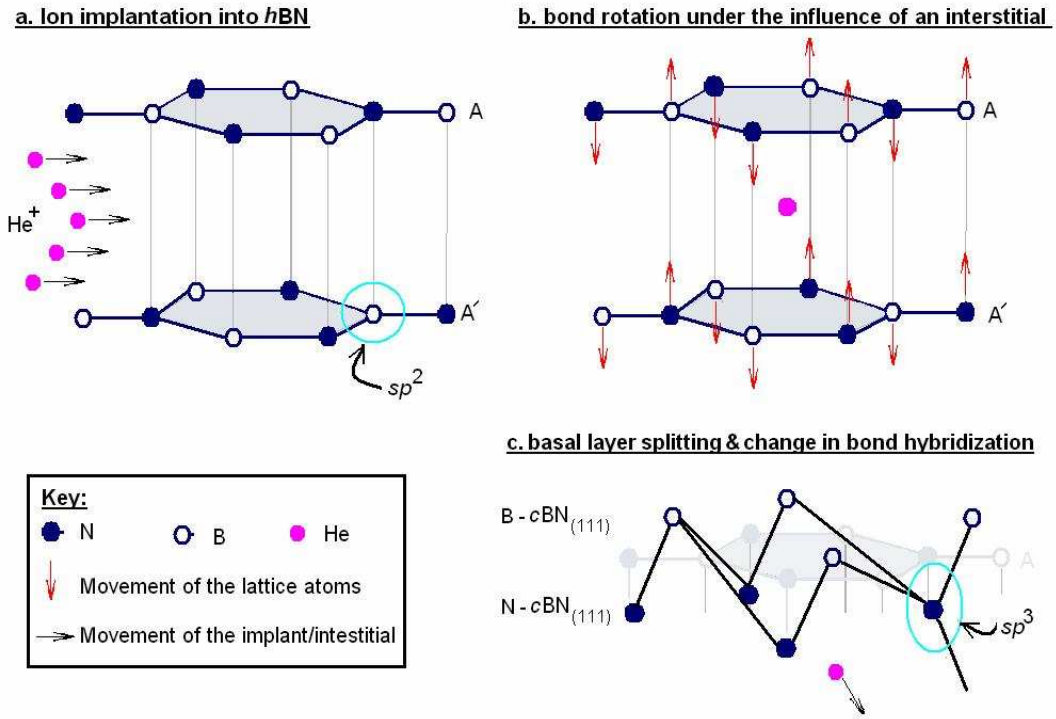

Figure 3.4: *A schematic diagram of the progression of an ion implantation-induced hBN-to-cBN phase transition.*

Generally, the respective characteristics and manner in which the transformation progresses for each mechanism distinguish the two mechanisms. In nucleation mechanisms, changes take place presumably atom–by–atom in such a way that neighbours before the transformation are not necessarily neighbours after the transformation. Hence this mechanism is dubbed: diffusional, the position of each individual atom is governed by the

Fickian diffusion laws. Whilst in the martensitic mechanism the whole group of atoms rearrange simultaneously while retaining their neighbours, only at a somewhat altered separation, it is thus known as a diffusionless mechanism [54], a shear-like transformation is a good example of this transformation mechanism.

Given a comparison of the steric arrangements in *h*BN and *c*BN, it is apparent that the phase transformation is diffusionless. The martensitic–type phase transformation progresses through what has come to be known as the 'progressive buckling and stretching of the basal hexagon' (see fig 3.4). Under high pressure, the flat (0001) B_3N_3 honeycombs in the basal layers lose their flatness as a result of the changes in the electron density in the interatomic and interlayer spaces. The electron density in the space between the B — N bonds of the same layer decreases; this weakens the bond, thereby an increase in the bond length so the B_3N_3 honeycomb becomes stretched. At the same time, the electron density between the boron atom and the nitrogen atom in adjacent layers increases, thus decreasing local interlayer spacing and as a result forms a bond – so the bonding network is now tetrahedral and 3-dimensional. The B_3N_3 honeycomb is buckled into a cubic chair configuration resembling the diamond-like structure [55]. In other words, the HPHT conditions have transfigured a low – density sp^2 bonded network into an sp^3 bonded network of lower specific volume. The pressure effect in this process can also be viewed as inducing bond rotations and inducing a (0001) layer to split into two planes one containing only boron atoms and the other only containing nitrogen atoms – this is easily conceivable if one looks at the initial and final structures [50]. In this case, an atom maintains its neighbour before and after the transformation.

The extreme conditions of phase transformation have been observed to be greatly influenced by the nature of the starting material, altering the grain sizes and/or the crystallinity has been used to reduce the transformation conditions greatly. The diffusional transformation is prevalent in cases were the starting material is not well crystallized. Unlike in the previous case, neighbours before the transformation are not necessarily neighbours after the transformation [28]. Hence transformations of the ball milled *h*BN, *a*BN and *t*BN phases under HPHT are shown to occur at somewhat lower thermobaric conditions.

Chapter 4

Experimental Details

4.1 Introduction

In this work, we investigate the structural modifications of *h*BN by ion implantation and the possibility of using ion implantation as a technique of influencing the *h*BN–to–*c*BN phase transformation under less extreme conditions. This chapter describes the samples and their preparation. The basic principles of the experimental techniques, the specific details and features of the experimental systems that were employed to perform experiments for this thesis are also discussed.

Ion implantation is used in this work as a technique to introduce considerable structural modification to the *h*BN phase. The samples were characterized by Raman spectroscopy and x-ray diffraction (XRD). With these methods one can obtain important information about the nature of a material's structure on a scale of the order of a few lattice constants. The characterization was done before and after ion implantation. Surface Brillouin Scattering (SBS) and Scanning Electron Microscopy (SEM) were also used to obtain more information on the nature of the surface of the initial material.

4.2 Samples and Sample Preparation

Hot–pressed polycrystalline *h*BN powder samples were used throughout this work. The samples used in the preliminary studies were supplied and prepared by Mr M Rebak of the Sample Preparation Lab at iThemba LABS (Gauteng). The samples that were used for the greater part of this study were supplied by Goodfellow® Cambridge Limited (England) in the form of a 15mm diameter rod. The *h*BN powder is generally synthesized

via the *Amide method*. This method is generally the reductive nitridation of boron oxide or other naturally found boron–based ores using urea compounds or ammonia. After the synthesis, the powder is moulded into its final forms via different processes, in this case by the hot–pressing process. A detailed description of the synthesis (including information on the nature and amounts of binders and other additives) could not be provided by the manufacturers as the information is considered classified and a trade secret.

The rod was machined into small circular discs of 0.5mm – 2.0mm thicknesses and diameters ranging from 3.0mm – 8.0mm. Given the polycrystalline and hot–pressed nature of the samples and the fine diamond grit sintered cutting disk used in the sample preparation, little sample polishing was done.

The sample preparation for SEM is relatively easy, the microscope only requires the sample to be electrically conductive; since *h*BN is not, some fine graphite powder is 'sprinkled' evenly on the sample surface (outside the area that is to be investigated) then the sample is mounted on an aluminium sample holder and loaded into the Ultra High Vacuum (UHV) via a sample introduction system. There was no special sample preparation requirement for the ion implantation, Raman spectroscopy, normal XRD and GIXRD (see discussion on Section 4.4.3). However, in the case of SEM, the technique probes the surface topography and the surface composition, among other things, so the sample surface has to be dust and contaminant free. In addition to this, since SEM is done under UHV conditions the samples have to be free of moisture or other solvents (which might vaporize or out–gas while in the vacuum) the samples may be baked at slightly over 100°C for a while to dry completely. Degradation of the samples has been shown to be very sensitive to moisture and several detergents/solvents, for this reason care was taken to ensure the samples were kept in a dry atmosphere, when possible.

4.3 Ion Implantation

4.3.1 Introduction

The ion implantation experiments described in this work were performed at iThemba LABS (Gauteng) formerly the Schonland Research Institute for Nuclear Sciences of the University of the Witwatersrand.

He^+ implantations into *h*BN were performed using the pressurized 1.4 MeV Cockcroft – Walton particle accelerator, "Christine". The samples were implanted at energies between 200 keV and 1.2 MeV to fluences ranging up to 1.0×10^{17} ions/cm^2 at room

temperature.

The damage profiles, the collision details, and the ranges of the implant species in *h*BN, were predicted by the TRIM Monte Carlo simulations which were performed using the *SRIM*® computer program version *2006.01* [56]. Fig 4.1 shows typical simulation outputs: [a] depicts the implant range distribution ($0-2\mu$m below the surface) whilst [b] depicts replacement collision detail, the target vacancies, and the target replacement profiles created by the alpha ions, realized for particles implanted into a virtual *h*BN solid at 200keV. It is clear from this fig that the projected range of the implants, $\sim 1.28\mu$m, is very much smaller than the thickness dimensions of the sample. It is thus very important that only the characterization techniques that are sensitive to the surface layer region must be employed to probe the resultant modifications introduced by the ion beams in this region.

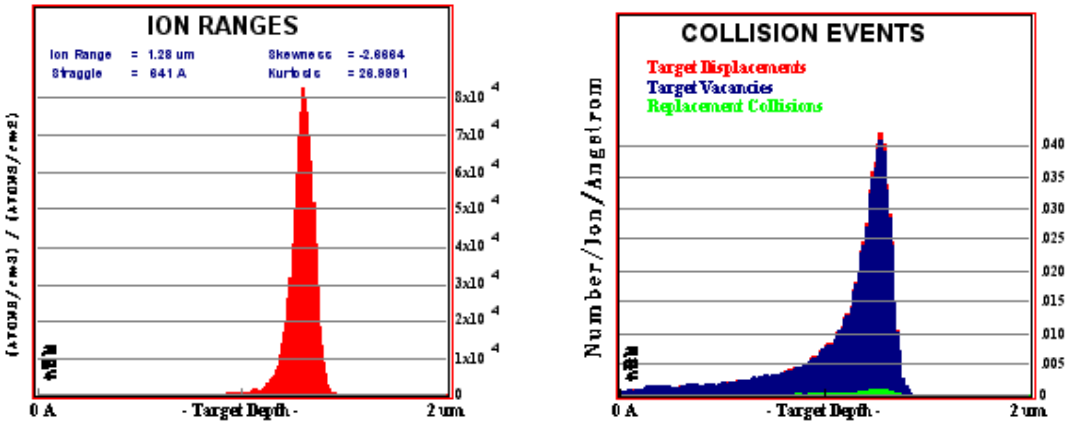

(a) (b)

Figure 4.1: *Shows the outputs of a SRIM2006 Monte Carlo calculation, where He^+ particles were implanted into hBN at 500 keV. [a] depicts the range of the implants whilst [b] depicts replacement collision detail, the target vacancies, and the target replacement profiles created by the implants.*

4.3.2 Instrumentation

The Cockcroft–Walton particle accelerator was converted from a Philips PW5121 electron accelerator to generate positive ions. A schematic diagram is given in fig 4.2. The description of the accelerator presented herein is based on the information given in the following references [57, 58, 59].

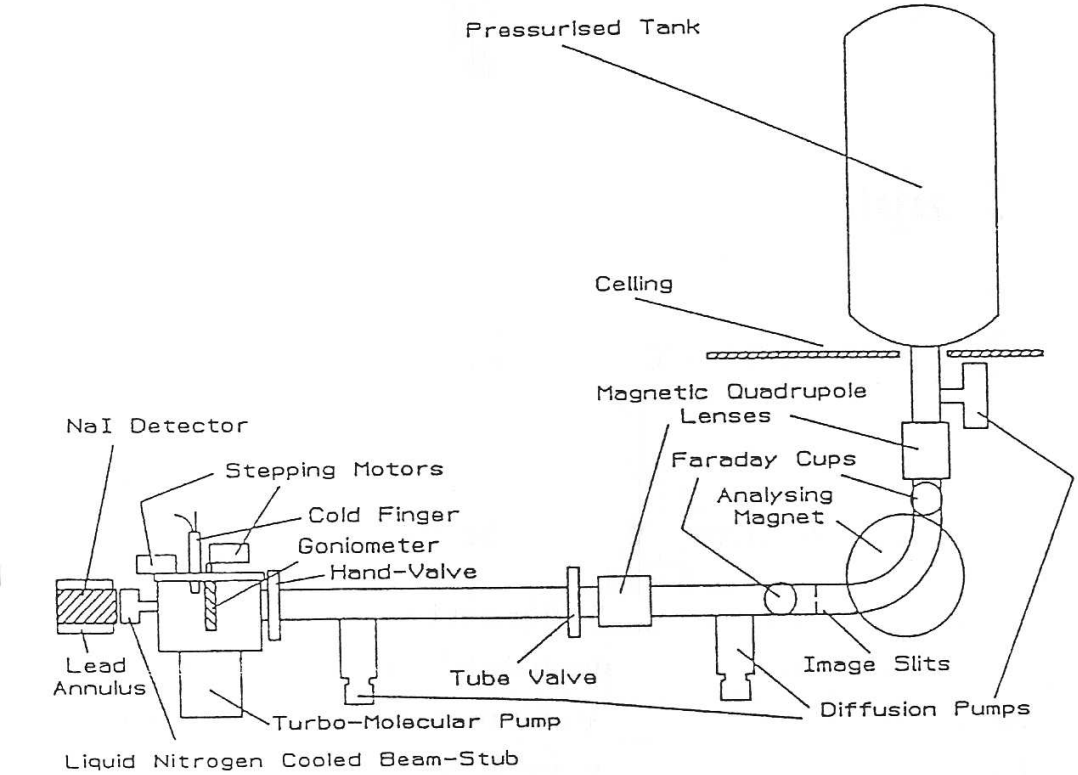

Figure 4.2: *A schematic diagram of the Cockcroft–Walton particle accelerator. After [57-59]*

The accelerator has a radio frequency ion source which ionizes the gas allowing positive charges to be accelerated to the target chamber via the evacuated beamline. Although only $^4He^+$ and sometimes $^1H^+$ ion beams were used in this study; D^+, and $^3He^+$ beams can also be generated and accelerated by this machine. The acceleration voltage is generated by means of a 14 stage voltage stack of doubling circuits — Cockcroft–Walton voltage generator.

The ion source operates at high positive potential so the generated (positive) ions are repelled and accelerated towards the target chamber which sits at ground potential.

Both the Cockcroft–Walton generator and the ion source are housed in a pressurized tank/vessel with an insulating $N_2 - CO_2$ gas mixture to prevent electrostatic discharges.

In the beamline during the beam transportation, the ion beam loses its shape mainly as a result of rapid expansions due to the space – charge[†] effect. This effect is more dominant at low ion propagation energies where the ions are exposed to one another for much longer

[†]also known as the 'blow – up' effect

resulting in significant mutual repulsion of the individual ions causing the beam to diverge away from the main beam axis. The magnetic quadrupole lenses follow immediately after the acceleration stage. The focusing is achieved by making use of magnetic lenses which apply transverse forces to maintain a small beam radius about the main beam axis (other implanters/accelerators also use electrostatic quadrupole lenses or both). The quadrupole lenses operate in a way analogous to that in which the optical lens focuses light.

The accelerator tube is contaminated with small amounts of residual gases and the ion beam itself with unwanted species – by bending the beam over a 90° curve of the analysing magnet, only the desired ion species pass through the magnet's resolution slits and remain in the beamline axis.

The beamline, the analysing magnet and the target chamber are all maintained under high vacuum maintained by the diffusion and turbo-molecular pumps, this minimizes the scattering of the ion beam by the residual gases and particles.

Before entering the target chamber, where the sample is mounted, the beam is collimated by means of two collimators/slits 2.4m apart. We used a square upstream collimator of adjustable dimensions and a 4mm diameter downstream collimator to limit the divergence of the scanned ion beam.

The sample was mounted in the target chamber; where the actual implantation takes place. The chamber is electrically isolated from the vacuum pumps and the rest of the beamline. The dose delivered was measured off the chamber by integrating the current of the ion beam.

4.4 Characterization Techniques

4.4.1 Raman Spectroscopy

Introduction

This section gives the description of the spectrometer, its attachments and how these instruments can be adapted to achieve the various techniques of Raman microscopy. A general discussion of the classical and quantum mechanical theories of Raman scattering is deferred to Appendix A.

Raman Instrumentation

The Raman scattering measurements done in this work were carried out using a Jobin – Yvon T64000 spectrometer at the Raman and Luminescence Laboratory housed in the School of Physics at the University of the Witwatersrand. The schematic diagram of the spectrometer is shown in fig 4.3. It is appropriate that the resolution of the microscope is of the same order as the implantation–affected surface thickness (about 1μm, see also fig 4.1).

Inelastic scattering is a very weak process and the Raman scattered line is also close to the Rayleigh scattered signal which is several orders of magnitude (typically 10^7) stronger. A careful signal processing is therefore necessary if useful information is to be extracted from the scattered signal components.

In the Jobin – Yvon T64000 spectrometer used, the Raman excitation is performed with a coherent and intense argon – ion (Ar^+) laser beam source. However, lasers are not perfectly monochromatic light sources, as they have a finite linewidth and contain a broadband component of spontaneous light radiation from the lasing material. A custom designed laser transmission filter is inserted into the incident beam path between the source and the sample to further narrow the incident beam linewidth [60]. The filtered beam is focused down to a small volume (to the order of $1\mu m^3$) on the sample through the objective. The scattered light is collected by the same objective of a microscope. At this stage the Raman signal is swamped by stray light signals (noise), the Rayleigh signal and other fluorescent signals from the scattering material. A *holographic notch filter*, between the sample and the monochromators provides for the necessary rejection of the unwanted light components swamping up the relatively weak Raman signal before it can be detected and measured by the spectrometer. The holographic notch filter is also custom made to operate at 514.5nm and have a narrow bandpass of down to $\sim 100 cm^{-1}$ [60, 61].

The filtered light is directed to the monochromators, the principal components of the spectrometer; an apparatus designed to measure the distribution of a signal in a particular wavelength region. The monochromator separates a broadband signal into single spectral lines according to wavelengths. Monochromators are based on diffraction grating dispersive systems [60], MONO X in fig 4.3 shows the unit monochromator. However, a single monochromator does not discriminate efficiently to separate the Raman broadband signal. The Jobin – Yvon T64000 spectrometer is a triple monochromator dispersive system as shown in the schematic diagram of the instrument (fig 4.3). In the coupled configuration, a monochromator has the capability for measuring a Raman signal of very low

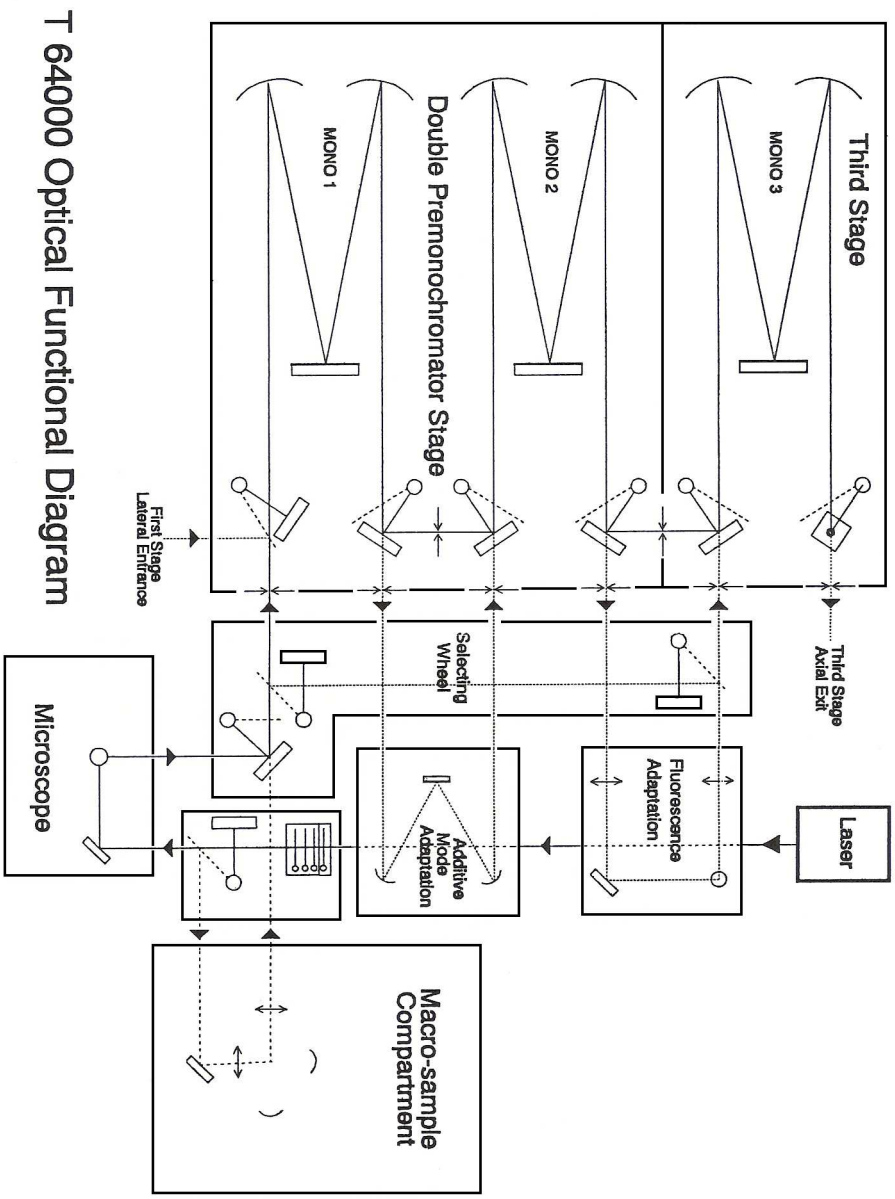

Figure 4.3: *The schematic diagram of the Jobin – Yvon T64000 spectrometer used in this work (courtesy of HORIBA Jobin Yvon Ltd (UK)).*

intensity in a broadband vibration/rotation band with high resolution [60]. However, the Jobin – Yvon T64000 spectrometer can be used in single spectrograph mode if the Raman line is not so close ($\sim$1000cm^{-1}) to the Rayleigh line, without compromising the spectral resolution greatly.

An array of *CCD* detectors is integrated onto the third monochromator exit slit. These optoelectronic devices detect and convert output photons to a digital signal that can be presented, manipulated and stored on to the interfaced computer.

Experimental Detail

The Raman experimental spectrometer system interfaced is to a PC and thus is software controlled. The spectrometer can be operated either in a macro–Raman mode, where measurements are done in the macro–sample compartment, normally for a very large or irregular sample specimen; or in the micro–Raman mode, where the measurements are done on the microscope stage. The laser light can be focused down to 1μm on the sample surface and a spectrum recorded. The spectrometer can also be operated in the 2-D mapping mode, where the computer controlled measurements are carried out on a motorized X-Y microscope stage. It is also possible to operate the spectrograph in a 3-D scanning mode, also known as Confocal microscopy, with the aid of a piezo Z- stage scanner [62]. For the experimental work covered in this thesis, the Raman spectrometer was used in the micro-Raman and 2-D mapping operation modes.

All the Raman experiments in this work were carried out under ambient conditions. A 514.5nm line of an Ar^+ ion laser was used as excitation source, at a beam power of 200mW, using a 20$\times$ objective (spot size $\sim$1.5μm), along with an 1800 grooves/mm grating in the spectrometer and a nitrogen cooled CCD detector. In the first set of Raman measurements, virgin and implanted *h*BN samples were characterized using micro-Raman operated in single spectrograph mode. In the second set of Raman experiments, the data acquisition was modified by the introduction of the motorized X-Y stage for the 2-D mapping measurements under the objective microscope. The mapping is done by sequential translation of the X-Y microscope stage which is software controlled. The sample was firmly held on to the X-Y stage by a self–adhesive tape to prevent (sample) motion out of the beam focus during the 'jacking' stage movements. 2-D mapping experiments were carried out over a 3000μm $\times$ 3000μm square matrix/area, of 20×20 points, covering the entire implanted region for each sample. Measurements of the amplitude, position and broadening of the primary *h*BN peak over the mapped area were carried out and the Ra-

man maps were automatically obtained. The output spectra were measured by a nitrogen cooled CCD detector linked to a computer that displays, analyses and stores the data.

4.4.2 X-ray Diffraction

Introduction

In this study, XRD was used to investigate and identify the BN phases present in the samples – which are hot–pressed powder and polycrystalline in nature and to determine the extent to which ion implantation induces solid–solid phase transformations in *h*BN.

In x-ray powder diffractometry, x-rays are generated within a sealed x-ray tube that is under vacuum. The wavelengths of the x-rays are characteristic of the metal target of the source. Common target metals used in x-ray tubes include Cu, Mo, Fe and Co. In this work we used a Cu (Z = 29) metal target corresponding to a wavelength of 0.154nm for Cu($K\alpha_1$) characteristic radiation [63]. These x-rays are collimated by a set of slits and directed onto the sample at an angle θ. The resultant x-ray diffraction peaks are produced by constructive interference of the monochromatic x-ray beam elastically scattered from each set of lattice planes at specific angles [64]. A typical XRD spectrum consists of a plot of reflected intensities versus the detector angular range, 2θ.

Each diffraction peak is unique, it measures the $d-$spacing of the scattering set of planes [63]. The peak position, intensity and width give information on the material's atomic or molecular composition and arrangement, crystallite distribution and orientation (or planar orientation in single crystals). The intensity of each peak differs from the other peaks in the pattern and reflects the relative strength of the diffraction from the related plane. The *peak intensity* or the area under a diffraction peak (minus the background signal) is used as a quantitative measure of the phase abundance [63].

Following Bragg's law, the position of diffraction peaks and the $d-$spacings that they represent provide information about the location of lattice planes in the crystal structure [64]. It therefore follows that the characteristic set of $d-$spacings generated in a typical x-ray scan profile provides a unique "fingerprint" of the major, minor and trace phases/compounds present in a sample.

A graphical software package for data acquisition and analysis – DIFFRAC^{plus} EVA, in combination with ICDD Powder Diffraction File databases (PDFs), was used in this work for data evaluation and phase identification. This was made possible by the software's search/match option, a capability to do background subtraction and a calculation

of parameters such as lattice parameters from the line profile position [63, 65].

Some parameters of the powder diffraction patterns such as the peak position (2θ), the peak intensity (as a percentage), and the lattice spacing (d_{hkl}) of the scattering planes were recorded, after which a comparison was made with the parameters available in the databases. The scattering planes of separation d_{hkl} satisfy the Bragg diffraction condition: $\lambda = 2d_{hkl} \sin 2\theta$, where *hkl* are the Miller indices which are proportional to the directional cosines of the scattering/diffracting planes whilst λ is the wavelength of the radiation used [63].

To meet the objectives of this study, two complementary x-ray diffraction methods were employed: the normal XRD scattering technique and the grazing incidence angle x-ray diffraction, GIXRD.

X-ray Scattering Techniques

The normal XRD measurement technique is based on the $\theta - 2\theta$ Bragg–Brentano scattering geometry, which probes both the surface and bulk of the sample material. The GIXRD scattering technique is a highly surface sensitive method that is based on a low incidence angle.

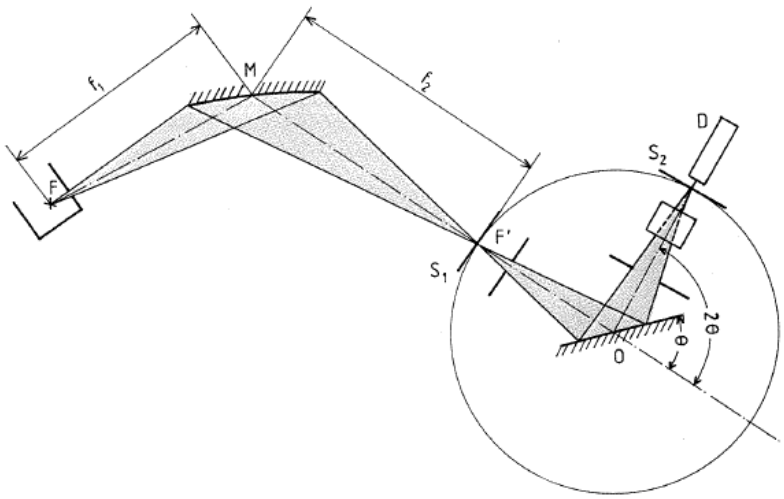

Figure 4.4: *A schematic diagram of a typical powder diffractometer used in the $\theta - 2\theta$ Bragg–Brentano geometry.*

Most of the XRD scan measurements described in this thesis was done using the BRUKER AXS D8 Advance diffractometer in the Jan Boeyens Structural Chemistry Laboratory at the University of the Witwatersrand. The diffractometer was used in the $\theta - 2\theta$

Bragg–Brentano diffraction geometry. A PW1710 Philips powder diffractometer from the School of Processing and Material Engineering was also used in the same geometry of operation. A schematic diagram of a diffractometer operating in the Bragg–Brentano diffraction geometry is shown in fig 4.4. In this geometry, the source is stationary whilst the sample and the detector (D) are in constant motion. It is also essential to note that the source, the sample (at O), and the detector remain on the tangent of the focus circle. In order to maintain these conditions, the detector and the sample are moved in such a way that at any given time the sample surface is at an angle θ whilst the detector maintains a 2θ angle with the incident x-ray beam. In practice, the sample rotates (in a rocking manner about O) at half the angular velocity of the detector [64, 63]. The slit systems (S_1 and S_2) as well as the monochromator/mirror (M) help collimate the x-ray beam before and after scattering of the beam on the sample surface.

4.4.3 Grazing Incidence Angle X-ray Diffraction

The conventional $\theta - 2\theta$ Bragg–Brentano scan diffraction geometry is a bulk material characterization method, it is not useful for the study of ultra thin, graded composition and multi-layered thin films, partly because of poor sensitivity and partly because of the presence of the interfering effect of the substrate. On the other hand, GIXRD enables one to probe the near–surface region [66], by improving surface sensitivity, via a strong interaction, total external reflection and thus limiting penetration.

The GIXRD scan geometry is a slight modification of conventional $\theta - 2\theta$ geometry. Incident pencil–narrow, near parallel, and monochromatic x-ray beams strike the sample surface at a fixed grazing angle that is close to the critical angle for total external reflection (typically less than 1°, depending on the solid material). These conditions are necessitated by the need to prevent the possibilities of interference effects from the sample subsurface and the need to enhance the sensitivity of the diffraction experiment to the surface atoms [65].

Narrow aperture slits are used to collimate the incident radiation whilst the combination of mirrors and filters are used as monochromators.

High energy x-rays have a refractive index of less than unity in most materials. In other words, the material is, for x-rays, less refractive than vacuum. At sufficiently small incidence angles (typically $\sim 1^\circ$) x-rays undergo total external reflection from the sample surface [67].

During the measurement of the GIXRD diffracted profile, unlike in the $\theta - 2\theta$ scan

arrangement, where both the sample and the detector are in synchronized rotational motion, the sample remains fixed whilst the detector rotated through the 2θ angular range. Throughout the measurement, the incident angle and the area under irradiation remains constant.

The diffracted beam optics is also modified to a parallel beam optics; a long Soller slit and a flat plate monochromator (graphite) is incorporated on the diffracted beam side to allow only those beams that are nearly parallel to arrive at the detector. The Soller slit is also instrumental in the rejection of diffuse scattered and background x-rays [67].

For the purposes of this work, wide angle x-ray diffraction profiles were recorded on a Philips PW1710 diffractometer with Cu(K_α) radiation. A glancing angle setup was used for all the measurements with an incidence angle of 1° and exposure times of the order of 20 hours.

4.4.4 Surface Brillouin Scattering

Introduction

Brillouin scattering is the inelastic scattering of an incident optical wave by thermally excited acoustic phonons generated and propagating in matter. It is contact–free and non-destructive. The mechanisms of optical light scattering in opaque and transparent media are different. Transparent media exhibit the *elasto–optical scattering mechanism* whilst Brillouin scattering in an opaque medium is attributed to the small amplitude surface ripples, hence *surface ripple scattering mechanism* [68].

Ion bombardment modifies the surface and near–surface region of the *h*BN sample material. The elasto–optical scattering mechanism is a bulk material phenomenon and is therefore not applicable to this work. In the surface ripple mechanism, the phonons present at the sample surface move in thermal equilibrium with very small amplitudes; that is, ripples. As a result of these ripples that appear to the incoming optical radiation as ‘gratings’ on the surface propagating at the speed of sound, the incoming radiation is Doppler shifted and gives rise to a change in the light frequency. This allows for two scattering possibilities involving the creation or annihilation of a phonon; that is, the Stokes and anti–Stokes scattering processes respectively. The scattering process is largely dependent on the dielectric constant of the material.

The velocity of sound is determined directly from the Brillouin shift, from this velocity shift, the elastic constants and velocity anisotropy, phase transitions as well as other

acoustic interactions with low frequency interactions can be determined.

The spectral width of the scattered light, examined with high spectral resolution, yields information about attenuation arising from the structural relaxations, anharmonicity among other possible mechanisms [69].

Apparatus

For all the SBS measurements carried our for the purpose of this thesis, a Sandercock (3+3) multipass tandem Fabry–Perot Interferometer (FPI) was used. Fig 4.5 shows a complete set–up schematic diagram of the apparatus. All measurements were carried out at room temperature in the backscattering and also in the 90° scattering geometries. A concise description of the instrument construction and mathematical treatment of SBS is given in references [68, 70]. The instrument is housed in the Laser Spectroscopy Laboratory in the School of Physics at the University of the Witwatersrand.

A schematic diagram of the SBS apparatus in a backscattering geometry is shown in fig 4.5. An intense Argon–ion laser source (λ = 514.5nm) was used throughout this work together with interferometric spectral analysis because the cross section of Brillouin scattering is very small therefore the intensity of the acoustically inelastic scattered optical signal is very weak. The figure shows how the exciting and scattered light are manipulated with the aid of mirrors and other components to direct the scattered light to the detector. The scattered light from the sample is frequency analyzed by the Fabry–Perot Interferometer (FPI). The FPI is an optical instrument commonly used for high resolution optical studies; it basically consists of two partially reflecting accurately parallel mirrors. It is used in the tandem and multipass mode to improve on the spectral resolution, contrast of spectral linewidths as well as reducing the signal-to-noise ratio. Using an FPI in this mode, weak Brillouin scattered light components can be separated from the intense Rayleigh scattered component efficiently. A silicon avalanche diode detector, attached to the FPI, was used to collect the data, which was recorded on a multichannel analyzer before being converted to a digital signal. The detector and multichannel analyzer are attached to a dedicated PC offering data display, manipulation and storage.

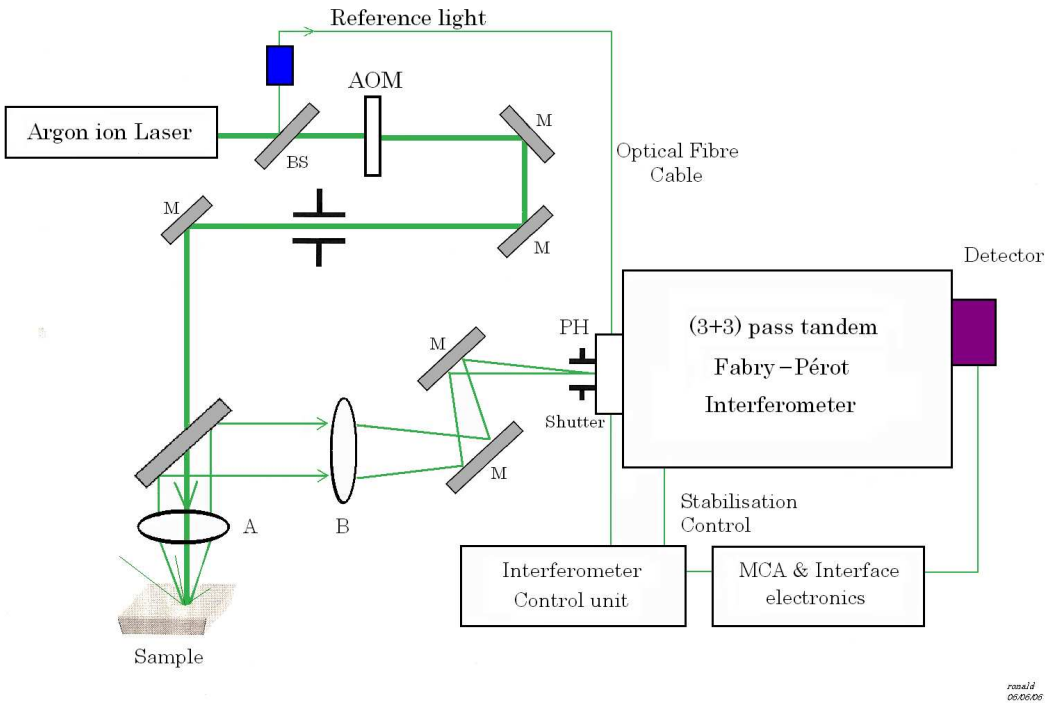

Figure 4.5: *A schematic diagram of the SBS instrument used in a backscattering geometry. The beam splitter (BS) extracts a small portion of the incident laser light (Reference light) that is fed to the detector by means of an optical fibre cable. The mirrors (M) manipulate the light from one point to another, altering their configuration changes the scattering geometry. The Acoustic-Optic Modulator (AOM) is used to to adjust the power of the laser light. The lenses (A & B) are used for scattered light collection and focusing. The shutter and pin-hole (PH) protect the detector. After [68,70].*

4.4.5 Scanning Electron Microscopy

Introduction

In a scanning electron microscope (SEM), a beam of electrons with energies up to 40 keV is finely focused at the surface of the specimen and scanned across it. On electron impact, some secondary electrons with energies of a few tens of electron volts are emitted and some of the high–energy incident electrons are backscattered. The intensity of both the secondary and backscattered electrons is very sensitive to the angle at which the electron beam strikes the surface; that is, to topographical features on the specimen. In this way, SEM can reveal the sample composition, crystallography and 3-D surface topographical images of high resolution which means that closely spaced features can be examined at a high magnification [71]. The information (on the surface properties of the

specimen) that can be obtained from the SEM experiments, includes the chemical elements, magnetic and electrical fields, voltage distribution, resistivity variation, electrical recombination fields, defect structures and light emitting properties [72, 73].

Apparatus

The SEM experiments in this work were done at the Electron Microscopy Unit at the University of the Witwatersrand. A schematic diagram showing how the electron microscope is constructed is illustrated in fig 4.6. The electrons are generated from a tungsten filament. They are accelerated to about 20 keV down the optical column through condenser and objective lenses. These lenses confine the electron beam to form into a fine beam spot as well as to focus the beam onto the sample surface. A scanning coil mechanism between the lenses raster scans the beam in the *x*- and *y*-directions to obtain a uniform illumination of the surface [71, 72].

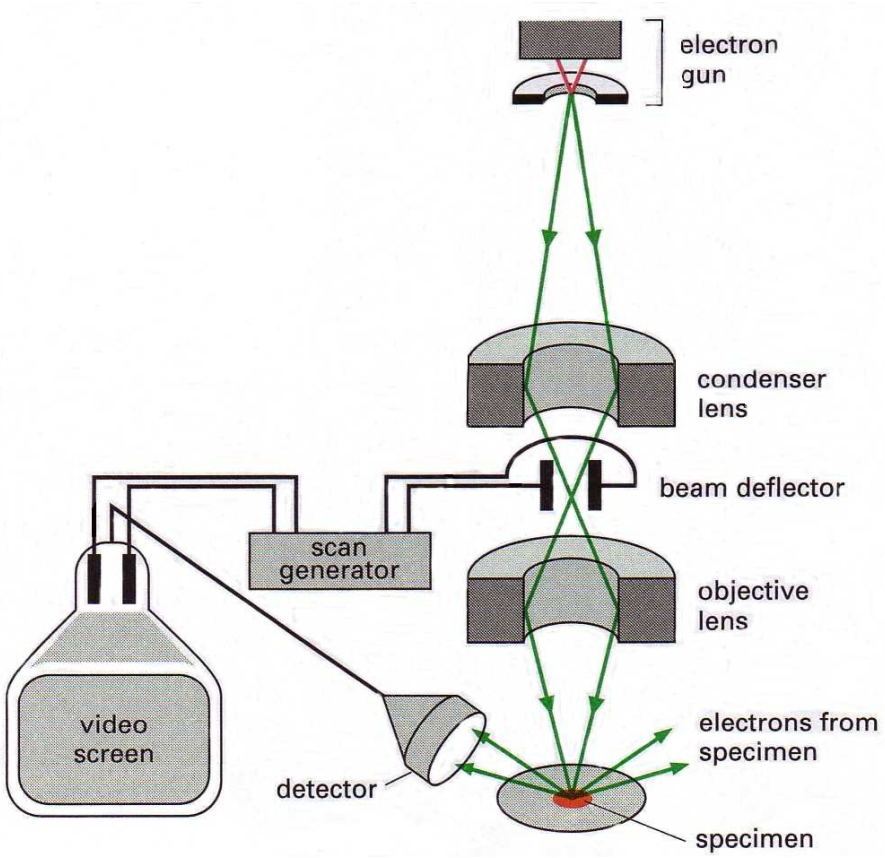

Figure 4.6: *The schematic diagram of the scanning electron microscope instrument*

Upon impact with the sample, several particles can be emitted (depending on the electron beam incident energy). In SEM experiments the secondary electrons of interest are backscattered electrons and secondary emitted electrons. In this case we were interested in the backscattered electrons, the intensity of which depends on the angle of incidence and on topography, surface conductivity, surface potential and magnetic fields. These are the properties we can therefore investigate using SEM [71].

When collected, the backscattered electrons induce a current in the collector, which is amplified and used to build up an image of the surface whose contrast relates to the topography and surface properties. The SEM equipment allows for the real–time monitoring of the image that is built up, it also has an inbuilt camera to capture the images.

Chapter 5

Results and Discussions

5.1 Introduction

Experimental results, characterization results as well as the simulation results are reported in this chapter. A complete analysis and discussion of the results is also presented herein, whilst the summary and conclusions derived from these results as well as suggestion for further studies are deferred to the next chapters. Most of the work described was carried out using alpha ion beams, however, proton beams were also used to investigate the probabilities of using smaller ions that caused the least lattice damage. A *SRIM2006* simulation program was used to help choose implant energies and assist in interpreting the results. Unless otherwise stated, 99.9% 'research grade' hot–pressed polycrystalline *h*BN powder samples supplied by Goodfellow (UK) were used throughout this study.

5.2 Preliminary Results

5.2.1 SRIM2006 Simulation

SRIM2006 was used to perform TRIM Monte Carlo calculations in order to predict the final implant depth distribution and the collision details of both the projectile ion and the recoil atoms. This information was used in selecting the implant energies as well as to help explain the results obtained.

Fig.s 5.1a and 5.1b show the range distribution of the He^+ implants in *h*BN for TRIM calculations performed at 200 keV and 1.2 MeV, respectively. The calculated projected range distributions of the implants are 0.882μm (fig 5.1a) and 2.68μm (fig 5.1b).

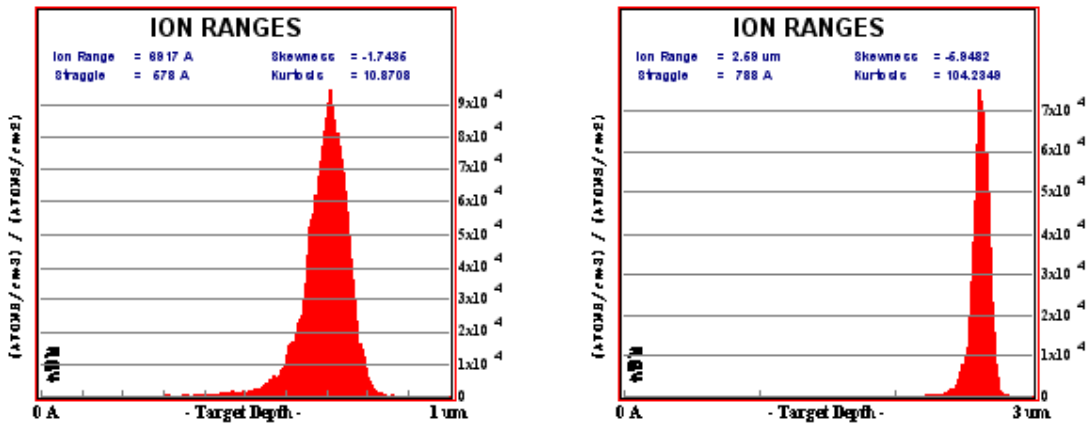

(a) (b)

Figure 5.1: *Ion range distribution profiled predicted for He^+ implanted into hBN at: [a] 200 keV, and [b] 1.2 MeV.*

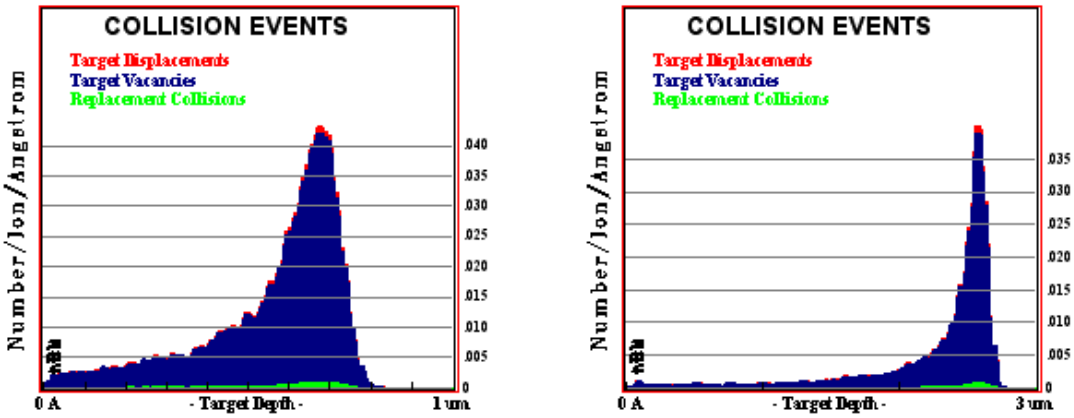

(a) (b)

Figure 5.2: *Collision details/damage profiles predicted for He^+ implanted into hBN at: [a] 200 keV, and [b] 1.2 MeV.*

Fig.s 5.2a and 5.2b show the profiles of the target displacements, target vacancies, and the replacement collisions as predicted by TRIM calculations performed at 200 keV and 1.2 MeV, respectively. The damage profiles also show the energy lost by an He^+ ion to nuclear collisions as it comes to rest in *h*BN. Whilst the damage profile created by the recoil atoms shows the density of vacancies created and the total energy lost to recoil atoms. TRIM calculations performed at 500 keV are shown in fig 4.1.

5.2.2 $\theta - 2\theta$ XRD measurements

Preliminary powder diffraction measurements were carried out on virgin samples and on samples implanted with 1.2 MeV He^+ particles to fluences of 1.0×10^{15} ions/cm^2 and 1.0×10^{16} ions/cm^2. 'Commercial grade' *h*BN samples were used. The measurements were carried out using the Bruker AXS Advanced D8 diffractometer. The detector was set to scan between 5° and 69.99°.

Fig 5.3 shows the XRD line profile obtained from the measurements. In addition to the broad feature appearing around 7°, numerous peaks (of high and low intensities) are observed.

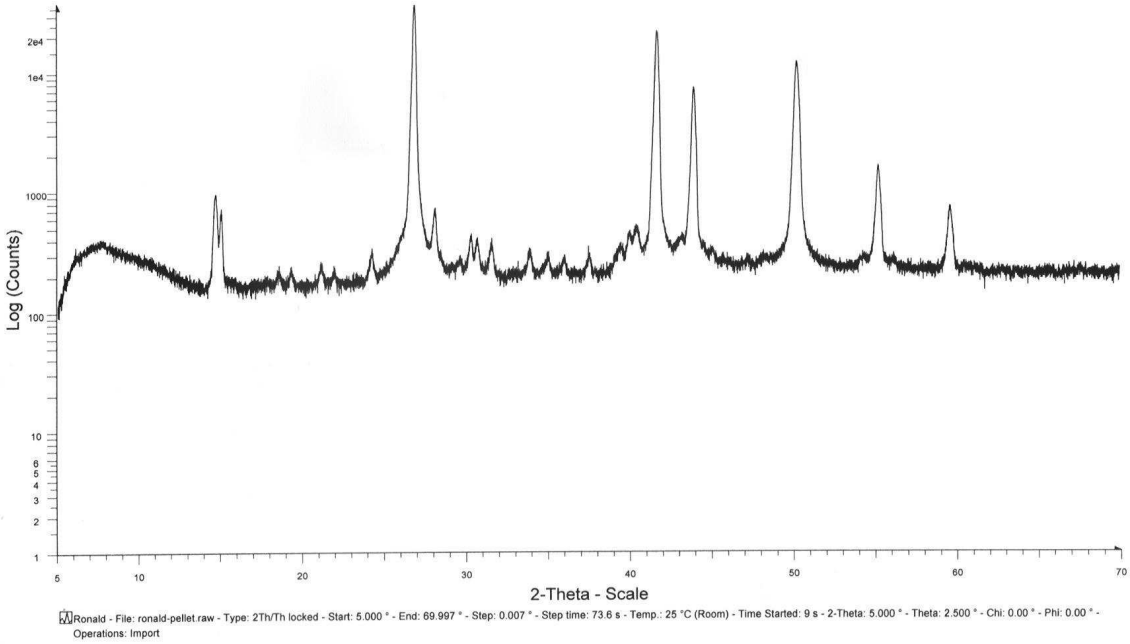

Figure 5.3: *The XRD line profiles measured for virgin and implanted 'commercial grade' hBN samples in the preliminary studies were observed to be similar. The implanted samples were implanted with 1.2 MeV He^+ particles to fluences of 1.0×10^{15} ions/cm^2 and 1.0×10^{16} ions/cm^2. Please note that the legend may not be legible on printed copies.*

5.2.3 SBS and SEM Results

SEM was used in this work mainly to investigate the surface topography. It became apparent to investigate the nature of the surface after the SBS experiments had failed to produce any results, it was observed that the samples are transparent to the incoming laser light due to the porosity of the samples. It was also observed that due to the high degree

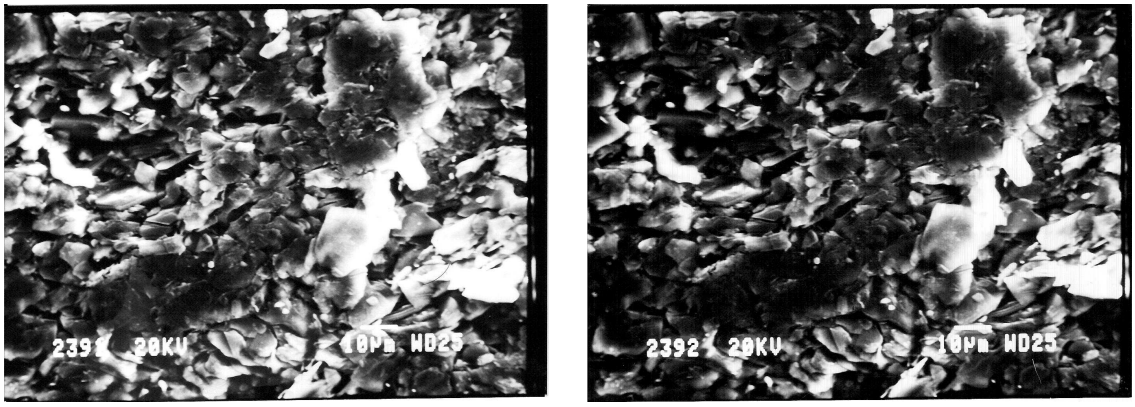

(a) (b)

Figure 5.4: *SEM micrographs showing the surface topography of the unimplanted samples used.*

of surface roughness, the light scattered was in all directions and hence the collected light was of the same magnitude as the background light, a meaningful spectrum could not be produced. In addition to that, we also wanted to detect any boric oxides, any other opportunistic compounds on the surface, and other binders that might have been included during the *h*BN synthesis process. Foreign compounds on the sample surface would have different conductivities as compared to the rest of the surface and hence different contrasts on the SEM micrographs. Fig 5.4 shows the SEM micrographs obtained from the measurements.

5.2.4 Discussion

The diffraction patterns observed for both the virgin and the 1.2 MeV He^+ implanted samples are similar. Thus, structural changes introduced by the ion implantation, if any, are below the detection limit of the technique or are being masked by the evidently high signal–to–noise ratio.

The diffraction pattern fig 5.3 is observed for both samples, and shows dominant peaks around 14.6°, 28.8°, 41.1°, 43.8°, 55.0°, and 59.5°. These peaks are characteristic of the *h*BN phase and are well documented in the reference pattern given in [74]. In addition to these, peaks appearing around 14°, 28°, 42°, 51°, and the broad escape peak centred on 7° may be due to silicon – possibly, from the sample holders used. There is also a possibility that the additional peaks appearing around 43.5° and 50.0° may be due to small amounts of *c*BN originally present in the samples. It was further noted that the samples used were hot–pressed *h*BN powder (conditions: 2000°C, 14MPa and binders to help form a

dense, strong engineering material [48]); under conditions these conditions, it is feasible that some *c*BN crystallites can precipitate and grow. The origins of the other numerous small peaks scattered across the profile could not be established, it is however suspected that they are due to binders, catalysts or/and other materials used in the manufacturing process.

Due to the sample's high degree of surface roughness and the material's transparency to laser, SBS measurement results on research grade samples could not be obtained. We further investigated the nature of the surfaces using SEM. The micrographs (fig 5.4) revealed that the surfaces exhibited a high degree of roughness and porosity as a result of the polycrystalline nature of the material as well as the hot–pressing process.

5.3 Raman Spectroscopy

We report and discuss the results obtained from the micro-Raman (μ-Raman) and two-dimensional, point–to–point Raman mapping (2D-Raman) measurements of virgin and implanted 'research grade' *h*BN samples.

5.3.1 Unimplanted *h*BN

μ–Raman

Fig 5.5 show the Raman spectra of unimplanted *h*BN measured at three different and arbitrary points on the sample surface. The spectra shows dominant Lorentzian–shaped peaks of high Raman intensity which are observed at 1365cm^{-1}.

Discussion

The observed peaks are consistent with the documented μ-Raman spectrum which is characteristic of a nominally–pure *h*BN with minimum internal stresses [75]. The baseline of spectrum A is lower than for spectra B and C. This is possibly due to the natural fluctuations of the Raman signal as a result of the randomly oriented interacting crystallites with a distribution of shapes and sizes. The *h*BN phase exhibits two phonon modes that are attributed to the E_{2g} symmetry vibration. Both modes are due to in–plane atomic displacements: the low-frequency mode (not measured in fig 5.5) which is characteristic of the 'rigid–layer shear' vibration ***between*** the basal plane appears around 52cm^{-1},

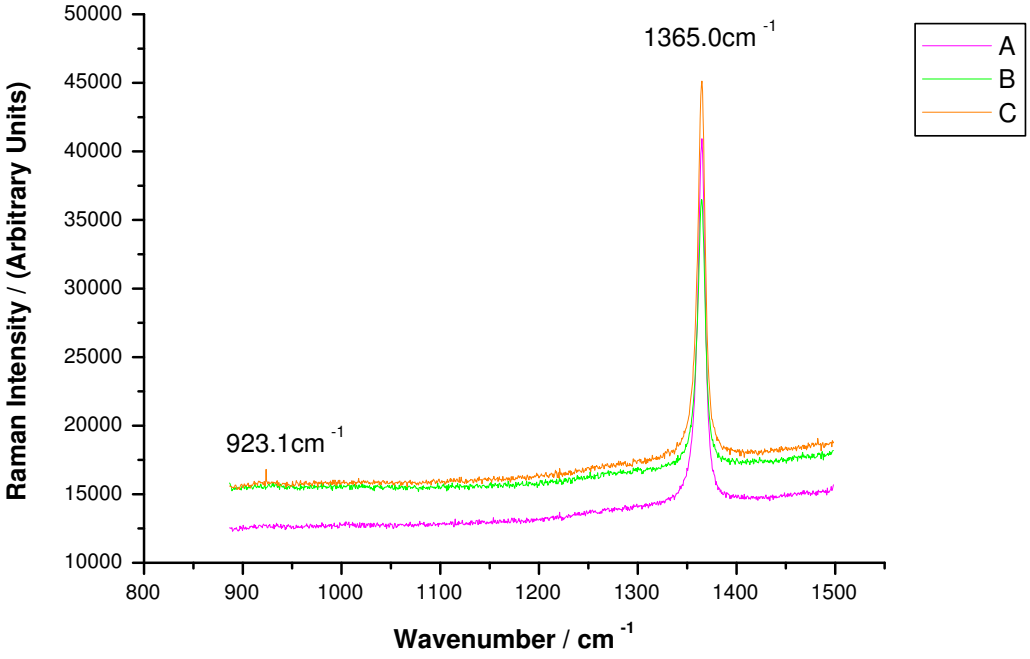

Figure 5.5: *The μ-Raman spectra measured at three different and arbitrary points on the surface of the unimplanted samples.*

whilst the high-frequency mode which is characteristic of a B — N bond stretching vibration ***within*** the basal plane appears around 1366cm^{-1} [76, 77, 78, 79].

2D–Raman

Fig.s 5.6 – 5.8 show the 2D-Raman maps of unimplanted samples measured on the surface. The 2D-Raman mapping measurements were performed using a software–controlled motorized X-Y microscope stage and automated spectral analysis. Here both the intensity map (fig 5.6), the position map (fig 5.7), and the width map (fig 5.8) are obtained from point-to-point measurements of the principal *h*BN μ-Raman peak at each of the 20×20 points on a $3000\mu\text{m} \times 3000\mu\text{m}$ wide matrix on the sample surface.

The intensity map (fig 5.6) shows the relative intensities of the measured 1365.4cm^{-1} Raman peaks plotted against the dimensions of the scanned matrix. The brightest and the darkest points on the 2D map correspond to the highest and lowest intensities of the principal *h*BN Raman peak measured, respectively. The measured values of the two extremes are given in table 5.1.

DIAGRAM	BRIGHTEST SPOT	DARKEST SPOT
FIG 5.6	16,500	8,500
FIG 5.7	1365.4cm^{-1}	1365.1cm^{-1}
FIG 5.8	9.0cm^{2}	8.6cm^{2}

Table 5.1: *Values corresponding to the measured brightest and darkest spots in fig.s 5.6 – 5.8.*

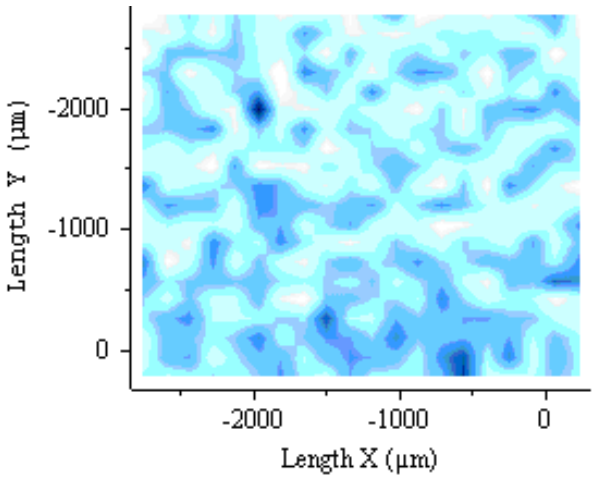

Figure 5.6: *The 2D-Raman intensity map of the 1365.4cm^{-1} Raman peak measured across the unimplanted sample surface.*

The peak position of the exciting laser line is taken to be 0cm^{-1}. The position map (fig 5.7) shows the relative positions of the measured individual μ-Raman peaks from the zero position. The contrast gives information on the shifts in the Raman lines from one another. The 2D-Raman maps are plotted against a 3000μm $\times$ 3000μm wide matrix of the scanned sample surface. The brightest spot and the darkest spot on the map correspond to the highest peak position and the lowest peak position of the principal *h*BN Raman line measured, respectively. In table 5.1, the values of the measured two extremes are given.

2D-Raman width maps show the spatial variation of the broadening of the μ-Raman lines across the scanned surface. Fig 5.8 shows that of *h*BN measured and plotted against the scanned 3000μm $\times$ 3000μm wide matrix of the sample surface. The colour contrast shows the distribution of the peak width, this information is vital in the assessment of how the crystallinity of the sample surface correlates with the radiation damage that the material has been exposed to. The brightest spot on the map and the darkest spot (given in table 5.1) on the map correspond to the highest and the least peak width values measured, respectively.

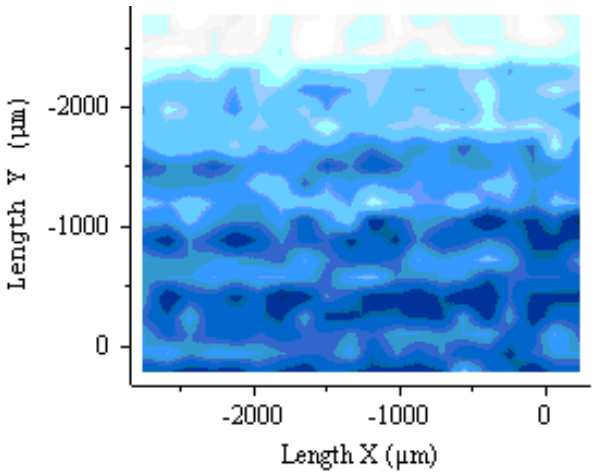

Figure 5.7: *The 2D-Raman position map showing the relative positions of the Raman peaks measured across the unimplanted hBN sample surface.*

Discussion

The 2D-Raman maps (fig.s 5.6 – 5.8) complement the μ-Raman spectra observed in the (fig 5.5). The small shifts in the positions, intensities and widths of the peaks that is observed 2D maps can be attributed to the natural fluctuations of the Raman signal as a result of the randomly oriented interacting crystallites with a distribution of shapes and sizes. It is thus perceived that the samples being characterized are nominally pure and that the sample's internal stresses are at a minimum [75].

5.3.2 1.2 MeV He^+ implanted *h*BN

The μ–Raman and 2D-Raman measurement results from different *h*BN samples implanted with 1.2 MeV He^+ ions to fluences of 1.0×10^{15} ions/cm^2 and 1.0×10^{16} ions/cm^2 using a 1.4 MeV Cockcroft–Walton accelerator are reported in this section.

μ–Raman

The μ-Raman spectra shown in fig 5.9 are for samples implanted to a fluence of 1.0×10^{15} ions/cm^2. The spectra *A, B* and *C* were measured from different spots in the centre of the implanted area of the sample whilst the spectra *D, E* and *F* were measured from different arbitrary spots outside the implanted area of the sample.

The μ-Raman spectra shown in fig 5.10 are for samples implanted to a fluence of 1.0×10^{16} ions/cm^2. The spectra *a, b, c* and *d* were measured from different arbitrary

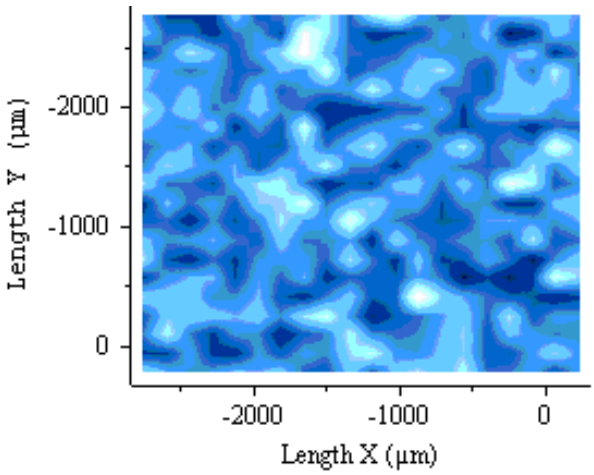

Figure 5.8: *The 2D-Raman width map showing the broadening of the 1365.4cm^{-1} Raman peak measured across the unimplanted hBN sample surface.*

spots on the sample surface in the region outside the implanted area, whilst *e, f, g, h, i, j* and *k* were measured from different arbitrary spots on the sample surface in the implanted region. Of particular interest is the broad feature observed for the *i* and *k* around 1296.6cm^{-1}, shown in fig 5.10 as an insert.

Discussion

Three μ-Raman features, two Lorentzian-shaped and one Gaussian-shaped, are observed in fig 5.9 whilst in addition to these three, a weaker and smaller Gaussian peak is observed in fig 5.10.

The narrow Lorentzian-shaped peaks appearing around 53cm^{-1} and 1367.3cm^{-1} are characteristic of the low- and high-frequency *h*BN phonon modes. These have been discussed already, see Section *5.3.1.* The comparable intensities of the Lorentzian peaks measured inside and outside the implanted region shows that, in both cases, the bombarded region is still predominantly *h*BN.

The μ-Raman spectra, *B* (in fig 5.9), and *f* and *j* (in fig 5.10) are Gaussian-shaped features, observed to be confined only to the implanted regions of the sample. They are centred around 752.9cm^{-1} and 760.2cm^{-1}, respectively. Notably, the intensity of this feature is twice as weak (lower intensity) for implantation at fluences of 1.0×10^{16} (fig 5.10) as compared to that observed for implantations at fluences of 1.0×10^{15} (fig 5.9). This is possibly because the larger extent of radiation damage introduced by the heavier bombardment at the surface greatly attenuates the scattered Raman signals. Though the

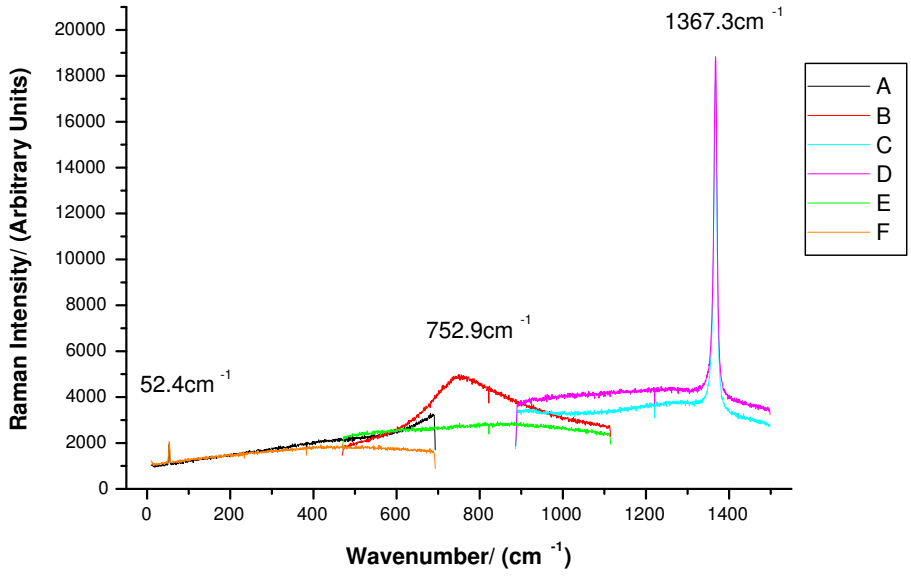

Figure 5.9: *The μ-Raman spectra taken at different points on the hBN sample that was implanted with 1.2 MeV He^+ ions to a fluence of 1.0×10^{15} ions/cm^2*

hexagonal phase retains its structure initially, heavier bombardment results in the distortion of the pre-existing ordered lattice structure. The broad feature is definitely a result of ion implantation as it is not evident in the Raman spectra of virgin samples, and its peak parameters (intensity, position and width) are affected by the implantation fluences as well as the macro- and micro-strains induced by ion bombardment.

The broad feature has been observed before by Sachdev and co–workers who attributed it to either crystalline or amorphous boron. The boron clusters are extended defects, appearing as the visible brown spot that forms on the sample surface during implantation [77, 80]. On the other hand, Jun Liu and co–workers observed that *r*BN Raman spectrum can be identified as *h*BN spectrum ***except*** for the extra peak that appears at 789cm^{-1} [81]. The later would suggest an *h*BN–to–*r*BN phase transformation to have taken place because for both fluences, the 789cm^{-1} peak lies within the broad feature's 'width'.

The fourth μ-Raman Gaussian feature observed only in fig 5.10 is much weaker, skewed, and relatively noisier. The feature appears around 1296.6cm^{-1}. It is also not observed in virgin samples and is therefore its origins are attributed to ion implantation. The room–temperature Raman spectrum of *c*BN has been measured previously by several investigators [76, 78, 82, 83]. The spectrum exhibits two strong Lorentzian-shaped peaks

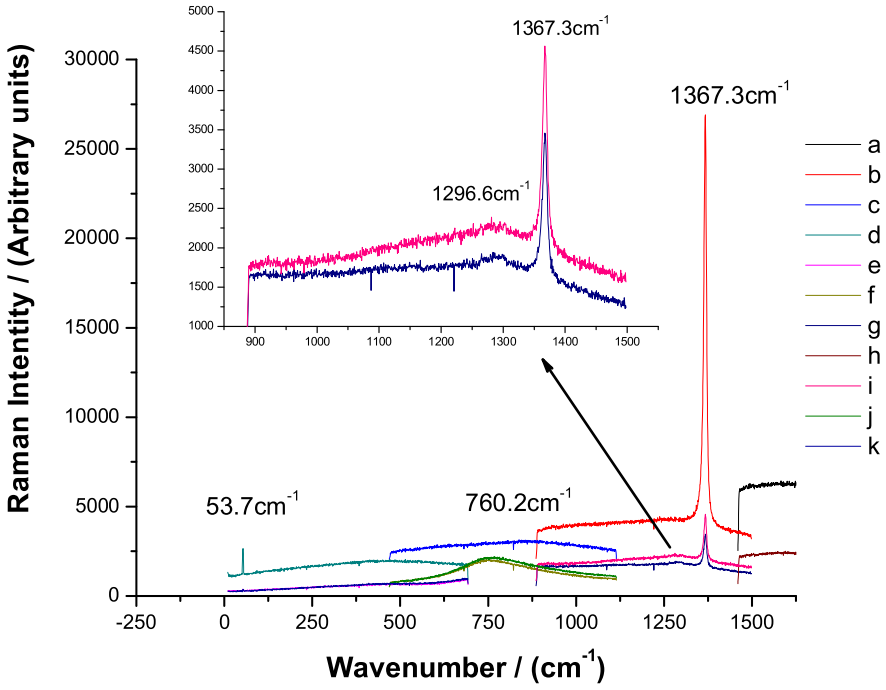

Figure 5.10: *The μ-Raman spectra taken at different points on the sample that was implanted to a fluence of 1.0×10^{16} ions/cm^2. The insert shows a weak 1296.6cm^{-1} peak observed.*

representing the transverse-optical phonon mode (TO) and longitudinal-optical phonon mode (LO) at 1057cm^{-1} and 1306cm^{-1}, respectively. On the other hand it has also been reported that for micro- and nano-crystal sized *c*BN, the TO and LO phonons degrade into a single, broader and rather asymmetrical phonon band 1285cm^{-1} [78].

2D-Raman

Fig.s 5.11 – 5.13 show the 2D-Raman maps obtained from the X-Y mapping measurements of the implanted *h*BN samples.

Fig 5.11 shows the 2-D Raman intensity maps obtained for the samples implanted to a fluences of 1.0×10^{15} ions/cm^2 (fig 5.11a), and 1.0×10^{16} ions/cm^2 (fig 5.11b); the maps were measured around the principal 1367.3cm^{-1} *h*BN Raman peak. The brightest and the darkest points on the map correspond to the highest and the lowest intensities of the peaks measured, respectively. The measured values of the two extremes are given in table 5.2.

Fig 5.12 shows the position maps obtained from 2-D Raman mapping measurements of the samples implanted to fluences of 1.0×10^{15} ions/cm^2 (fig 5.12a), and 1.0×10^{16}

DIAGRAM	FLUENCE (ions·cm^{-2})	BRIGHTEST SPOT	DARKEST SPOT
Fig 5.11a	10^{15}	30,000 counts	10,700 counts
Fig 5.11b	10^{16}	18,000 counts	1,500 counts
Fig 5.12a	10^{15}	1365.4cm^{-1}	1365.3cm^{-1}
Fig 5.12b	10^{16}	1365.8cm^{-1}	1366cm^{-1}
Fig 5.13a	10^{15}	8.9cm^{-1}	8.6cm^{-1}
Fig 5.13b	10^{16}	*	*

Table 5.2: *The values corresponding to the measured brightest and the darkest spots in fig.s 5.11 – 5.13.*

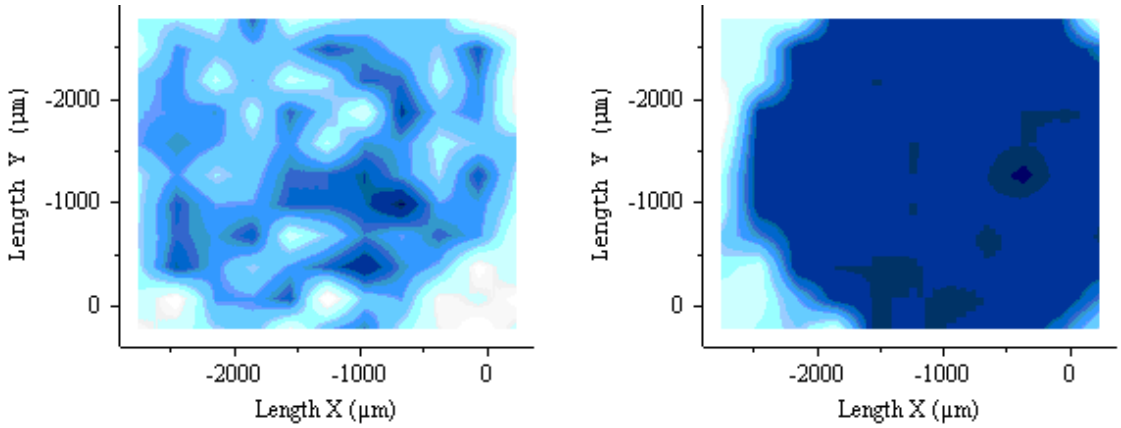

(a) (b)

Figure 5.11: *The 2D-Raman intensity maps of the sample implanted to fluences of: [a] 1.0×10^{15} ions/cm^2, and [b] 1.0×10^{16} ions/cm^2.*

ions/cm^2 (fig 5.12b). The brightest spot and the darkest spot on the map correspond to the highest peak position and the lowest peak position of the principal *h*BN Raman line measured, respectively. Table 5.2 gives the values of the measured two extremes.

Fig 5.13 shows the 2-D Raman width maps obtained for the samples implanted to fluences of 1.0×10^{15} ions/cm^2 (fig 5.13a), and 1.0×10^{16} ions/cm^2 (fig 5.13b). The brightest spot on the map and the darkest spot (given in table 5.2) on the map correspond to the highest and the least peak width values measured, respectively. The Raman width measurements for the 1.0×10^{16} ions/cm^2 fluence implanted samples (fig 5.13b) can not be used as the bright spot appearing on the map masks out the contrast of the map that was; the bright spot could possibly be detector saturation or something on the sample surface.

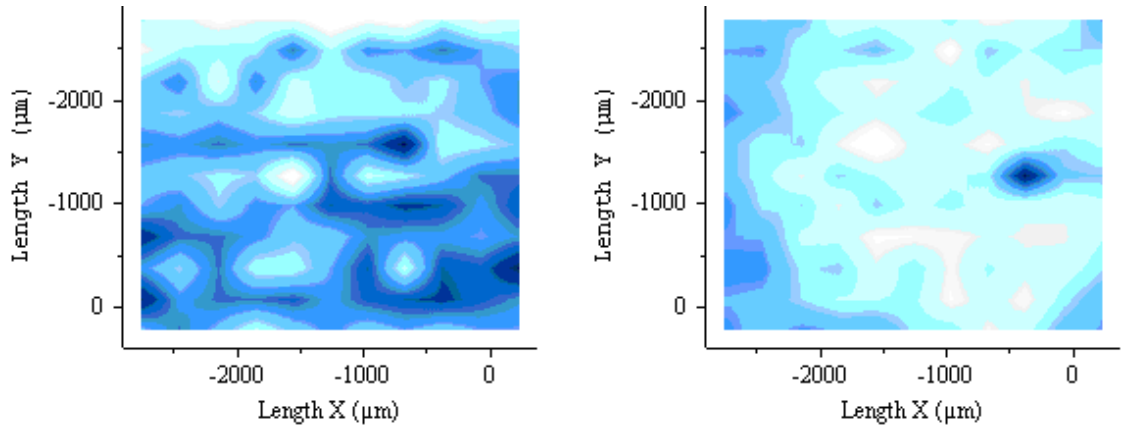

(a) (b)

Figure 5.12: *The 2D-Raman maps showing the relative positions of the principal Raman peaks measured on the sample implanted to fluences of: [a] 1.0×10^{15} ions/cm^2, and [b] 1.0×10^{16} ions/cm^2.*

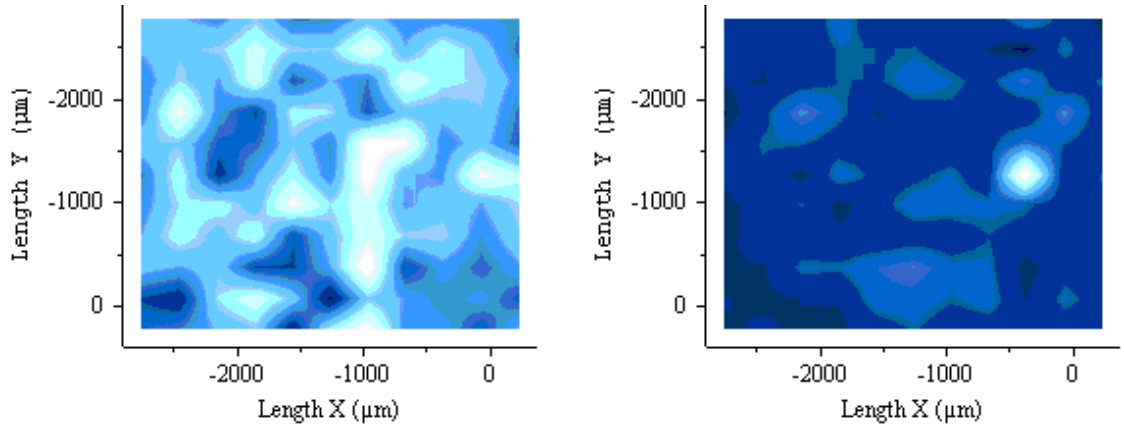

(a) (b)

Figure 5.13: *The 2D-Raman width map showing the broadening of the principal Raman line measured on the sample implanted to fluences of: [a] 1.0×10^{15} ions/cm^2, and [b], 1.0×10^{16} ions/cm^2.*

Discussion

The 2D-Raman maps are not perfectly centred on the implanted spot, but the implanted spot is however visible. The measured values of the peak position, and peak width shows that the material is still predominantly *h*BN – this result complements the μ–Raman spectra measured (see fig.s 5.9 and 5.10). The generally low Raman intensity, greater width and the wider peak position distributions in the irradiated regions can be

attributed to the implantation–induced residual stresses and the loss of crystallinity of the surface in this region, whilst retaining the initial phase bond order. The extent of this is more pronounced in the implanted region for the samples implanted to fluences of 1.0×10^{16} ions/cm^2, however, the peak position shifting and broadening of the Raman lines for both cases is clearly insignificant [75]. The 2D-Raman maps were not measured for the broad peak.

5.3.3 750 keV He^+ implanted *h*BN

μ–Raman Results and Discussion

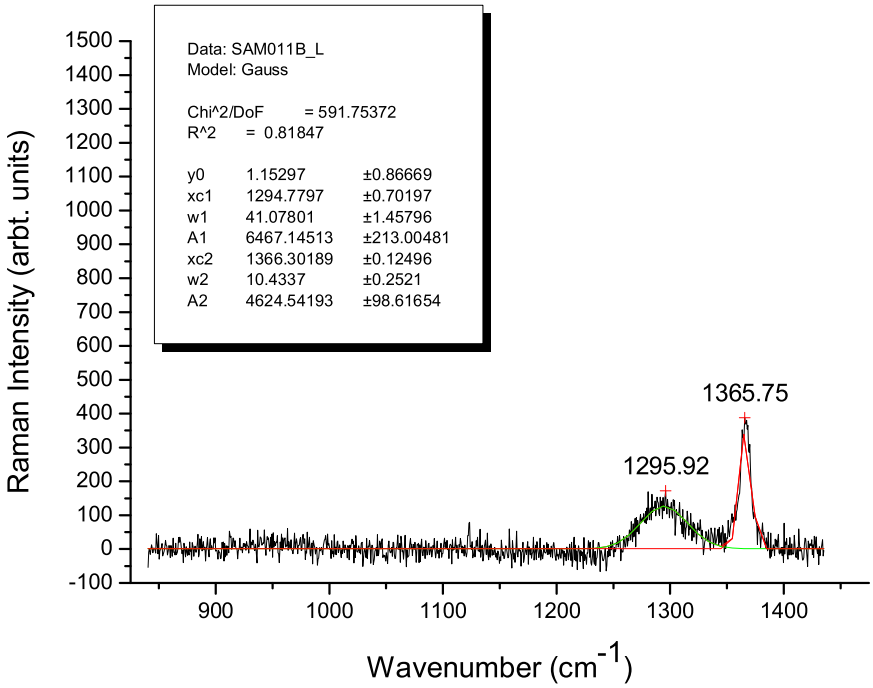

Figure 5.14: *The μ–Raman spectrum measured inside the irradiated region of the hBN sample that was implanted with 750 keV He^+ ions to a fluence of 2.0×10^{16} ions/cm^2. The red and green lines are the Lorentzian and Gaussian plot fits.*

Some μ–Raman measurements were carried out on an *h*BN sample that was implanted with 750 keV He^+ ions to a fluence of 2.0×10^{16} ions/cm^2. The measurements were made at twenty different points in a single line across the implanted sample's diameter. The μ–Raman spectra of all the twenty measured points is shown in fig B.1 in Appendix B. Fig

5.14 shows the μ–Raman spectrum measured inside the implanted region of the sample (point L).

Despite the low signal-to-noise ration, two noticeable features dominate the spectrum; a Lorentzian-shaped peak appearing at 1365.75cm^{-1} and a Gaussian-shaped peak centred at 1295.92cm^{-1}. The Gaussian-shaped peak is observed to be confined only to the implanted sections of the sample. The intensity of the Lorentzian-shaped peaks in the implanted regions is also observed to be severely attenuated. In general, the Raman signal measured in the implanted regions is characterised by a low signal-to-noise ratio. As discussed before (in Section *5.3.2*), the two peaks can be attributed to the residual *h*BN and to the nanocrystal sized *c*BN phases, respectively.

5.3.4 500 keV He^+ implanted *h*BN

The μ–Raman and 2D-Raman measurement results from different *h*BN samples implanted with 500 keV He^+ ions to fluences of 2.0×10^{16} ions/cm^2 and 1.0×10^{17} ions/cm^2 using the 1.4 MeV Cockcroft–Walton accelerator are reported in this section.

2D–Raman

Fig.s 5.15 – 5.17 show 2D-Raman maps measured around the primary *h*BN peak appearing at 1366cm^{-1}. Fig.s 5.18 – 5.20 are 2D-Raman maps measured around the broader and weaker Raman feature observed around 1290cm^{-1}. The broad feature is confined to the implanted regions and is more pronounced for the 2.0×10^{16} ions/cm^2 fluence implanted sample. The feature is much weaker, much broader, and characterized with larger measurement errors for the 1.0×10^{17} ions/cm^2 fluence implanted samples.

Fig 5.15 shows the intensity maps, of the primary *h*BN Raman peak at 1366cm^{-1}, for the samples implanted with 500 keV He^+ ions to fluences of 2.0×10^{16} ions/cm^2 (fig 5.15a) and 1.0×10^{17} ions/cm^2 (fig 5.15b). The brightest spot on the map corresponds to the highest Raman peak intensity on the map; the darkest one, to the least Raman peak intensity on the map. The measured highest and least Raman peak intensity values are given in table 5.3.

Figure 5.16 shows peak position maps of the primary *h*BN Raman line at 1366cm^{-1} for samples implanted with He^+ ions at 2.0×10^{16} ions/cm^2 (fig 5.15a) and 1.0×10^{17} ions/cm^2 (fig 5.16b) fluences. The lightest spot and the darkest spot on the map correspond to the highest peak position measured and the lowest peak position of the principal

DIAGRAM	FLUENCE (ions·cm^{-2})	BRIGHTEST SPOT	DARKEST SPOT
FIG 5.15a	2×10^{16}	43,000 counts	350 counts
FIG 5.15b	10^{17}	40,000 counts	100 counts
FIG 5.16a	2×10^{16}	1365.5cm^{-1}	1365cm^{-1}
FIG 5.16b	10^{17}	1366.6cm^{-1}	1364.7cm^{-1}
FIG 5.17a	2×10^{16}	11.4cm^{-1}	8.2cm^{-1}
FIG 5.17b	10^{17}	14.2cm^{-1}	7.2cm^{-1}

Table 5.3: *The values corresponding to the brightest and the darkest spots measured around the principal 1366cm^{-1} Raman peak in fig.s 5.15 – 5.17.*

*h*BN Raman line measured, respectively. The measured (highest and lowest) peak position values are given in table 5.3.

Figure 5.17 shows the 2-D Raman width maps obtained for the 2.0×10^{16} ions/cm^2 fluences (fig 5.17a), and the 1.0×10^{17} ions/cm^2 fluences (fig 5.17b) implanted samples. The darkest spot on the map corresponds to the least measured Raman peak width, and the opposite is true. The measured peak width values are given in table 5.3.

DIAGRAM	FLUENCE (ions·cm^{-2})	BRIGHTEST SPOT	DARKEST SPOT
FIG 5.18a	2×10^{16}	*	0 counts
FIG 5.18b	10^{17}	60 counts	0 counts
FIG 5.19a	2×10^{16}	1292cm^{-1}	1298cm^{-1}
FIG 5.19b	10^{17}	1290cm^{-1}	1300cm^{-1}
FIG 5.20a	2×10^{16}	*	*
FIG 5.20b	10^{17}	65cm^{-1}	*

Table 5.4: *The values corresponding to the brightest and the darkest spots measured around the 1290cm^{-1} Raman peak in fig.s 5.18 – 5.20.*

There also appears an extra weak and much broader Raman feature evident only within the irradiated region. Its intensity, position, and width were measured around 1290cm^{-1} and plotted against the 3000μm $\times$ 3000μm wide matrix of the sample surface for both fluences (2.0×10^{16} ions/cm^2 and 1.0×10^{17} ions/cm^2). The feature was characterized with larger measurement errors, especially for the 1.0×10^{17} ions/cm^2 fluence implanted samples, hence some values in table 5.3 are missing.

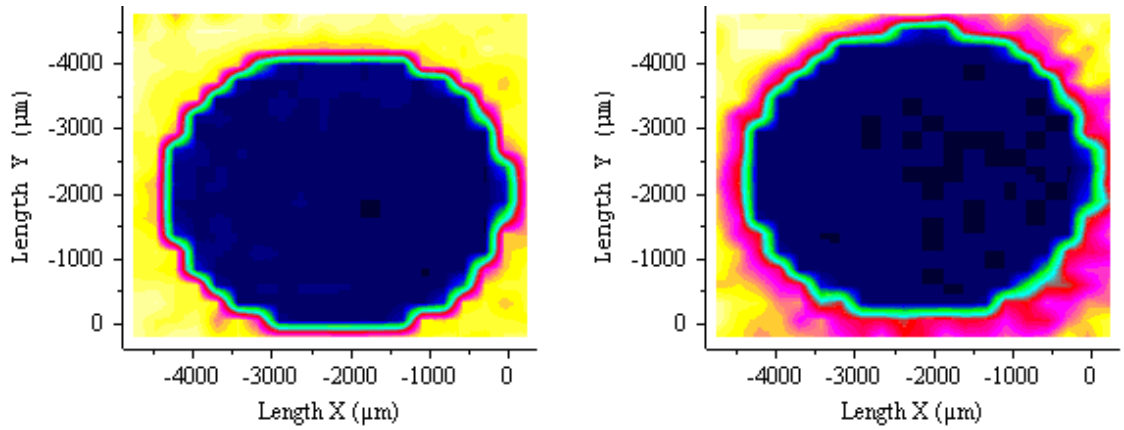

(a) (b)

Figure 5.15: *The 2D-Raman intensity maps measured for the samples implanted to fluences of: [a] 2.0×10^{16} ions/cm^2, and [b] 1.0×10^{17} ions/cm^2. The maps were measured around the principal 1366cm^{-1} Raman peak.*

Figure 5.18 shows the 2D-Raman measured intensity maps. The brightest spot on the map corresponds to the highest Raman peak intensity on the map; the darkest one, to the least Raman peak intensity on the map. The measured highest and least Raman peak intensity values are given in table 5.4. The measured peak intensity values for the green and red spots on the map are 100 counts and 290 counts for the samples implanted to fluences of 2.0×10^{16} ions/cm^2 (fig 5.18a). The yellow spots are erroneous; they are a result of the detector saturation.

Figure 5.19 shows the 2D-Raman position maps measured around the 1290cm^{-1} peak. The brightest spot on the map corresponds to the highest Raman peak position on the map; the darkest one, to the lowest Raman peak position on the map. The measured peak position values (highest and lowest) are given in table 5.4. Again, the yellow spots are erroneous; they are a result of the detector saturation.

Figure 5.20 shows the Raman width maps measured around 1290cm^{-1}. The darkest spot on the map corresponds to the least measured Raman peak width, and the opposite is true. The measured peak width values are given in table 5.4. For the samples implanted to a fluence of 2.0×10^{16} ions/cm^2 (fig 5.17a), the red spots on the map corresponds to 35cm^{-1}, and the green spots to 22cm^{-1}; whilst for the samples implanted at 1.0×10^{17} ions/cm^2 (fig 5.19b), the red spots correspond 40cm^{-1}, and the yellow spots correspond to 65cm^{-1}.

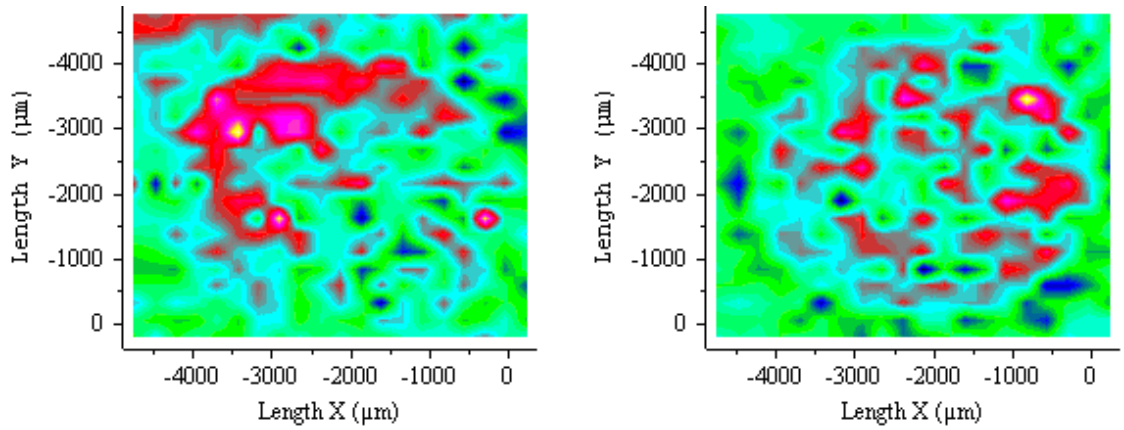

(a) (b)

Figure 5.16: *The 2D-Raman position maps measured for the sample implanted to fluences of: [a] 2.0×10^{16} ions/cm^2, and [b] 1.0×10^{17} ions/cm^2. The maps were measured around the principal 1366cm^{-1} Raman peak.*

Discussion

2D-Raman mapping measurements of the samples implanted to fluences of 2.0×10^{16} ions/cm^2 show two features. The principal Lorentzian *h*BN peak is observed around 1365cm^{-1} (fig 5.16a) with a maximum peak width of 11.4cm^{-1} in the implanted region (fig 5.17a). In addition to this peak, a Gaussian peak centred around 1290cm^{-1} (fig 5.19a) is observed. The broad feature is more pronounced for the samples implanted at 2.0×10^{16} ions/cm^2, much broader and weaker for samples implanted at 1.0×10^{17} ions/cm^2 and is only confined to the implanted region. Generally, the Raman measurements of the samples implanted to a fluence of 1.0×10^{17} ions/cm^2 show a significant decrease in the intensity of the Raman scattered signals from the irradiated region, considerable shifting and broadening in the primary Lorentzian *h*BN peaks as well as the broad feature being relatively weak and broader, it appears between 1281cm^{-1} and 1300cm^{-1}.

The map in fig 5.16b shows that the peak position differences are significant as compared to fig 5.16a; this can be attributed to induced residual stresses in the implanted sample surface. The maps 5.15 and 5.16 also show that the material is predominantly *h*BN and indicate a higher degree of radiation induced damage [75]. However, a closer analysis of the position maps 5.19 and 5.20 show that an *h*BN–to–nanocrystalline *c*BN (n-*c*BN) phase transformation resulted from the ion implantation.

The room–temperature Raman spectrum of *c*BN has been measured previously by several investigators [76, 78, 82, 83]. The spectrum of an *infinite single crystal* of black

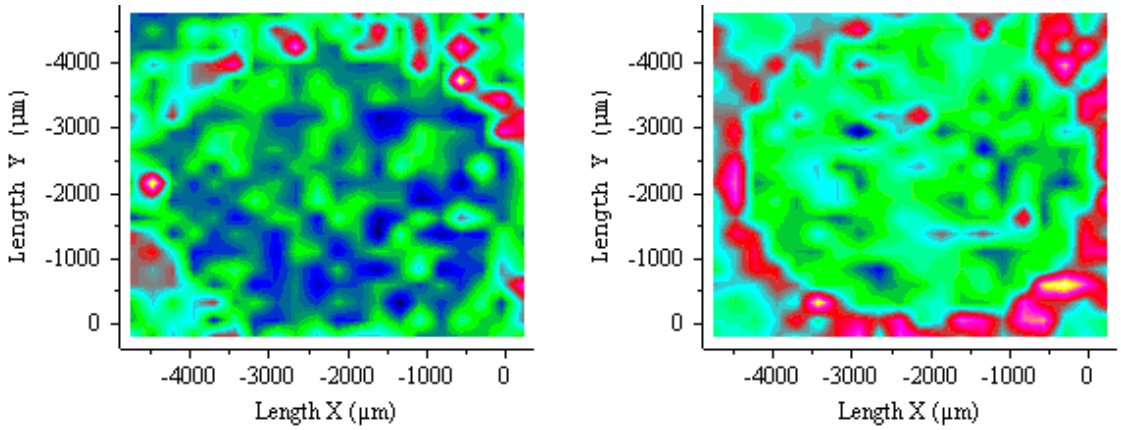

(a) (b)

Figure 5.17: *The 2D-Raman width maps of the sample implanted to fluences of: [a] 2.0×10^{16} ions/cm^2, and [b] 1.0×10^{17} ions/cm^2. The maps were measured around the principal 1366cm^{-1} Raman peak.*

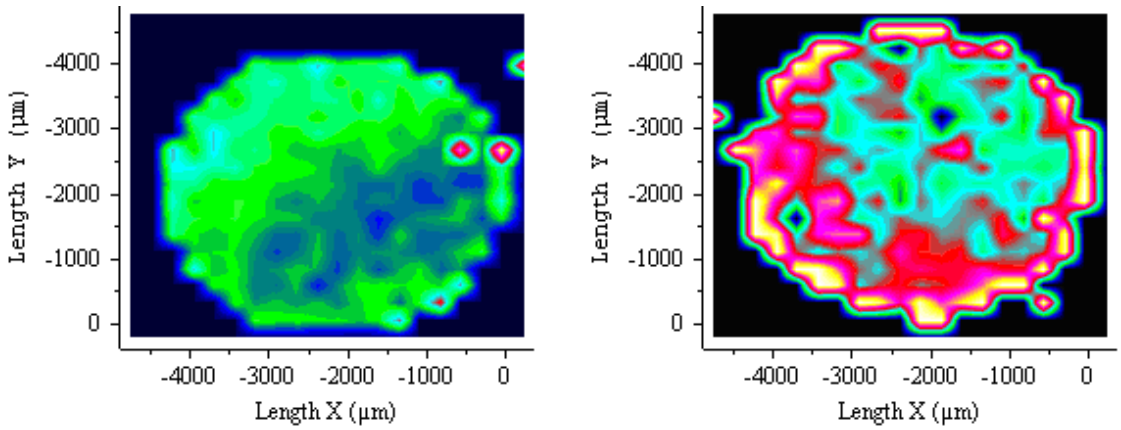

(a) (b)

Figure 5.18: *The extra 2D-Raman intensity maps of the sample implanted to fluences of: [a] 2.0×10^{16} ions/cm^2, and [b] 1.0×10^{17} ions/cm^2.*

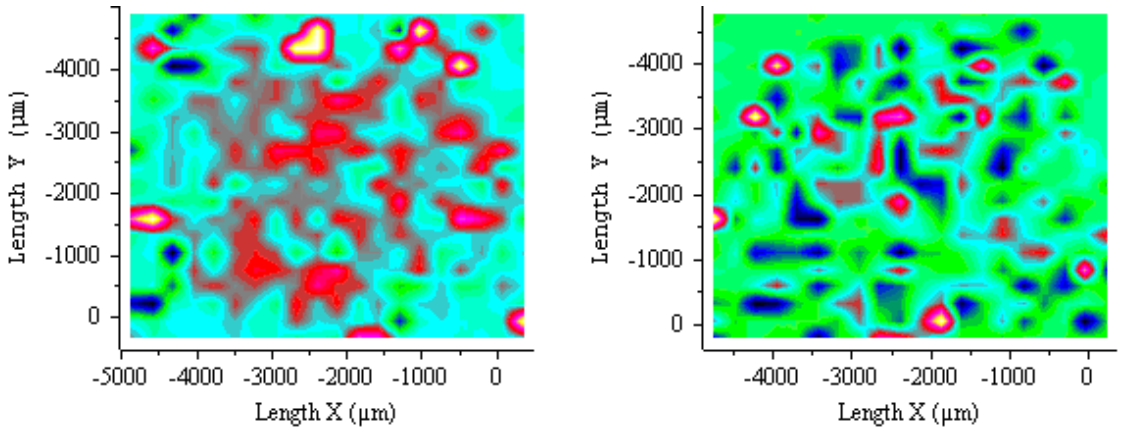

(a) (b)

Figure 5.19: *The extra 2D-Raman position maps of the sample implanted to fluences of: [a]* 2.0×10^{16} *ions/cm*^{2}*, and [b]* 1.0×10^{17} *ions/cm*^{2}*.*

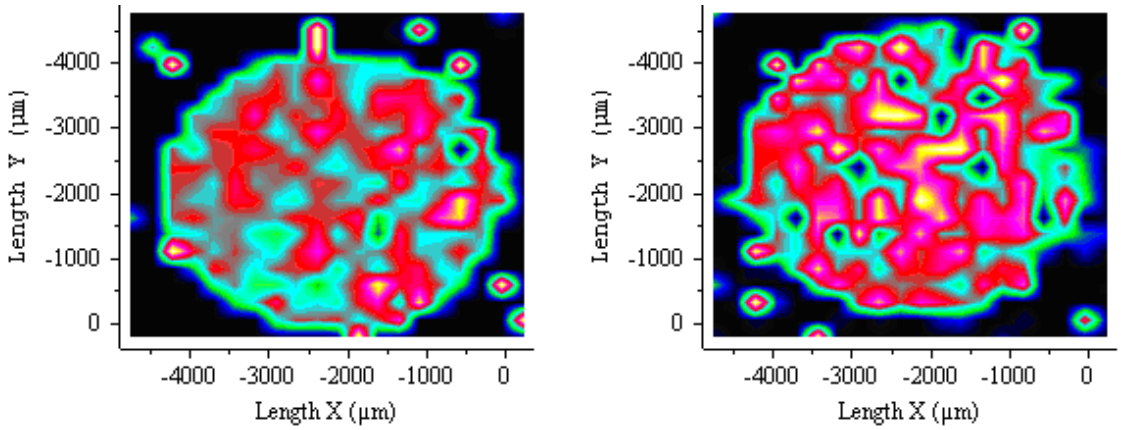

(a) (b)

Figure 5.20: *The extra 2D-Raman width maps of the sample implanted to fluences of: [a]* 2.0×10^{16} *ions/cm*^{2}*, and [b]* 1.0×10^{17} *ions/cm*^{2}*.*

*c*BN [76] exhibits two strong lines representing the Brillouin zone centre transverse-optical phonon mode (TO) and a longitudinal-optical phonon mode (LO) at 1057cm^{-1} and 1306cm^{-1}, respectively. It has also been reported that the Raman spectrum of *amorphous* BN shows an additional weaker and broader feature around 1260cm^{-1} and that *nanocrystalline c*BN (n-*c*BN) also exhibits a weak and broad feature centred on 1285cm^{-1} [78]. In fact, for the n-*c*BN phase the TO and LO phonons degrade into a single, broader and rather asymmetrical phonon band 1285cm^{-1}. Besides the low Raman scattering cross-section (due to the generally low light absorption of *c*BN because of the wide bandgap), the peak intensity is further lowered in the material due to phonon–confinement effects associated to small crystal size and high defect density [78, 82, 83]. The observed experimental data is in agreement with the theory described above.

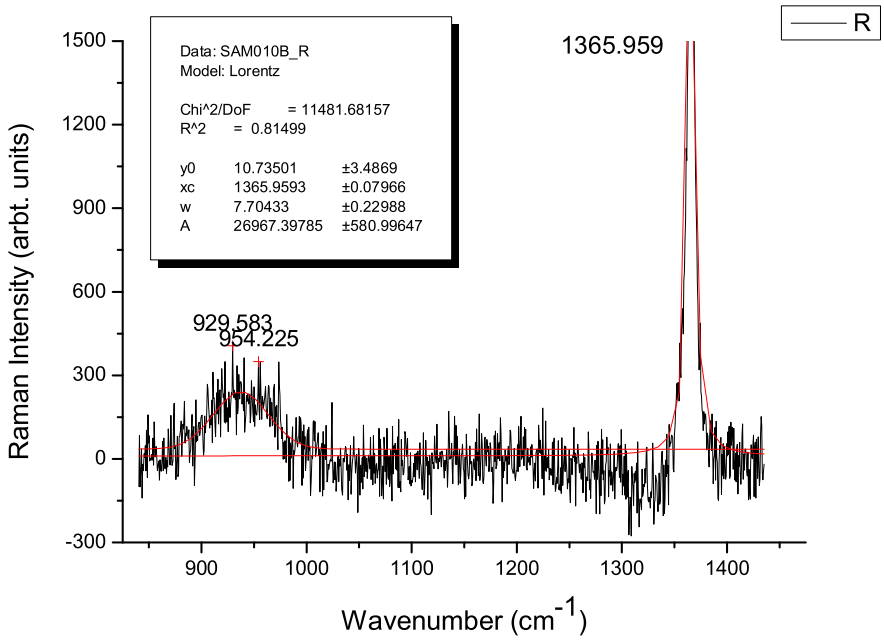

Figure 5.21: *The μ–Raman spectrum measured inside the irradiated region of the hBN sample that was implanted with 350 keV He^+ ions to a fluence of 1.0×10^{15} ions/cm^2. The red line is a Lorentzian fit.*

5.3.5 350 keV He^+ implanted *h*BN

μ–Raman Results and Discussion

The μ–Raman measurement results shown in this section were carried out on *h*BN samples that were implanted with 350 keV He^+ ions to a fluence of 1.0×10^{15} ions/cm^2 and 2.0×10^{16} ions/cm^2. In each case, the μ–Raman measurements were made at twenty different points in a single line across the implanted sample's diameter. The μ–Raman spectra of all the twenty measured points, for each case, are shown in fig B.2 and fig B.3 in Appendix B. Fig 5.21 shows the μ–Raman spectrum measured for the sample implanted to 1.0×10^{15} He^+ ions/cm^2; fig 5.22, that was implanted to 2.0×10^{16} He^+ ions/cm^2.

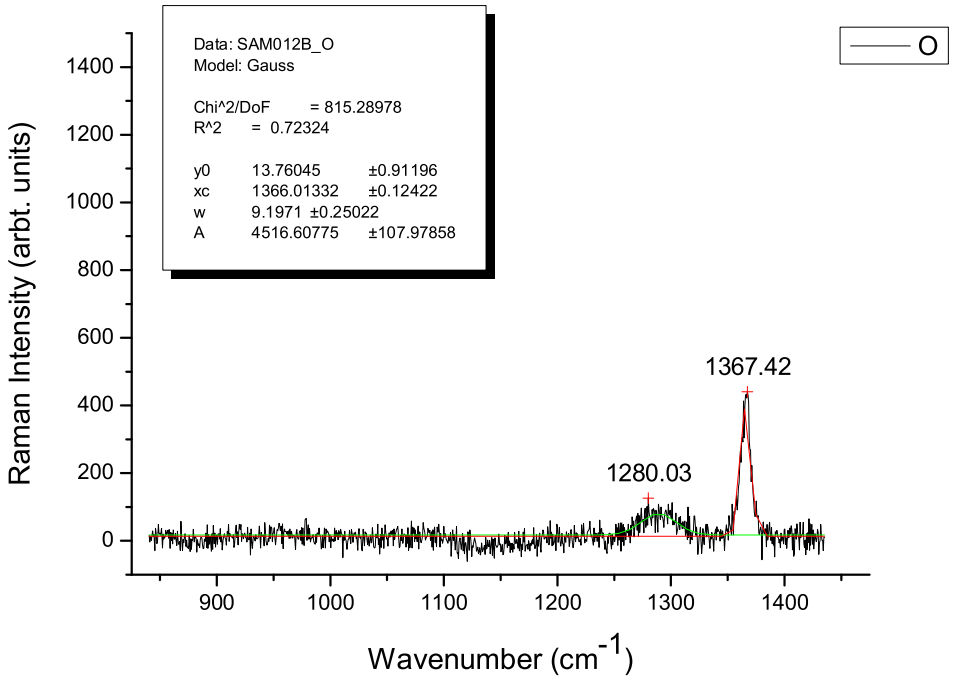

Figure 5.22: *The μ–Raman spectrum measured inside the irradiated region of the hBN sample that was implanted with 350 keV He^+ ions to a fluence of 2.0×10^{16} ions/cm^2. The red and green lines are the Lorentzian and Gaussian plot fits, respectively.*

In both cases, the Lorentzian-shaped peak appearing at 1365.75cm^{-1} is still dominant, even in the implanted sections of the sample. Although the Raman signal is heavily attenuated and slightly broadened, this shows that the implanted region remains predominantly *h*BN. A significant Gaussian-shaped peak centred at 1280.03cm^{-1} is observed in fig 5.22. As seen in the previous discussions, the Gaussian-shaped peak is observed to

be confined only to the implanted sections of the sample. Unlike in the previous discussions, a Gaussian-shaped peak centred around 929cm^{-1} is observed in fig 5.21, however, its origins could not be identified.

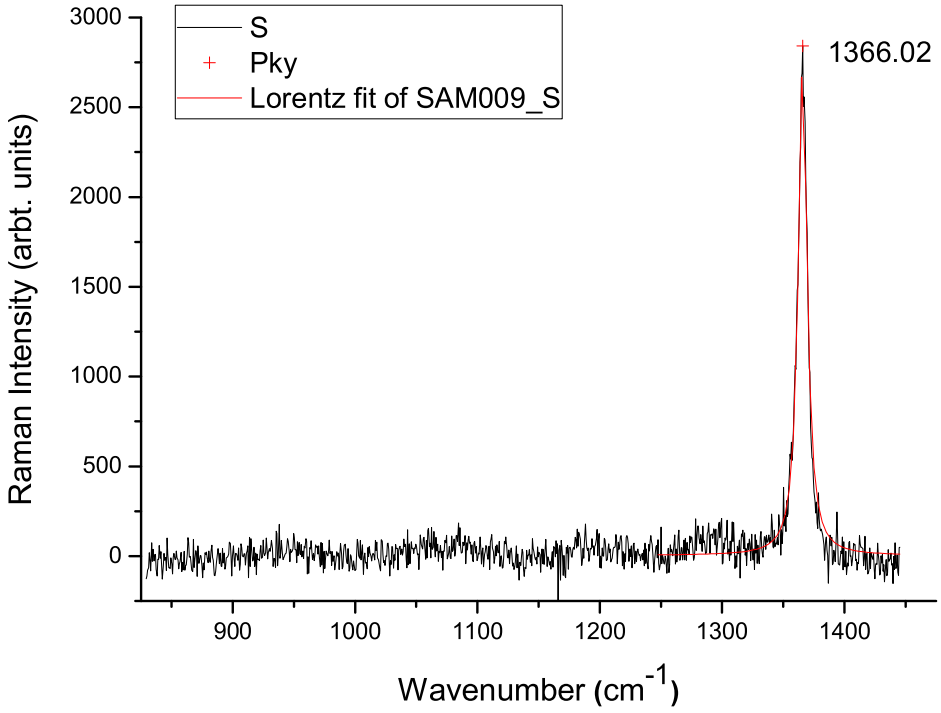

Figure 5.23: *The measured μ–Raman spectrum of the hBN sample that was implanted at 200 keV with 1.0×10^{15} He^+ ions/cm^2.*

5.3.6 200 keV He$^+$ implanted *h*BN

μ–Raman

Two *h*BN samples were implanted with 200 keV He$^+$ ions to fluences of 1.0×10^{15} ions/cm^2 and 2.0×10^{16} ions/cm^2. The μ–Raman profiles measured at twenty different points across the samples' implanted region are presented in this section. The μ–Raman profiles measured are shown in fig B.4 and fig B.5 in Appendix B. Fig 5.23 (S in B.4) and fig 5.24 (N in B.5) shows the typical magnified individual spectrum observed in the implanted regions.

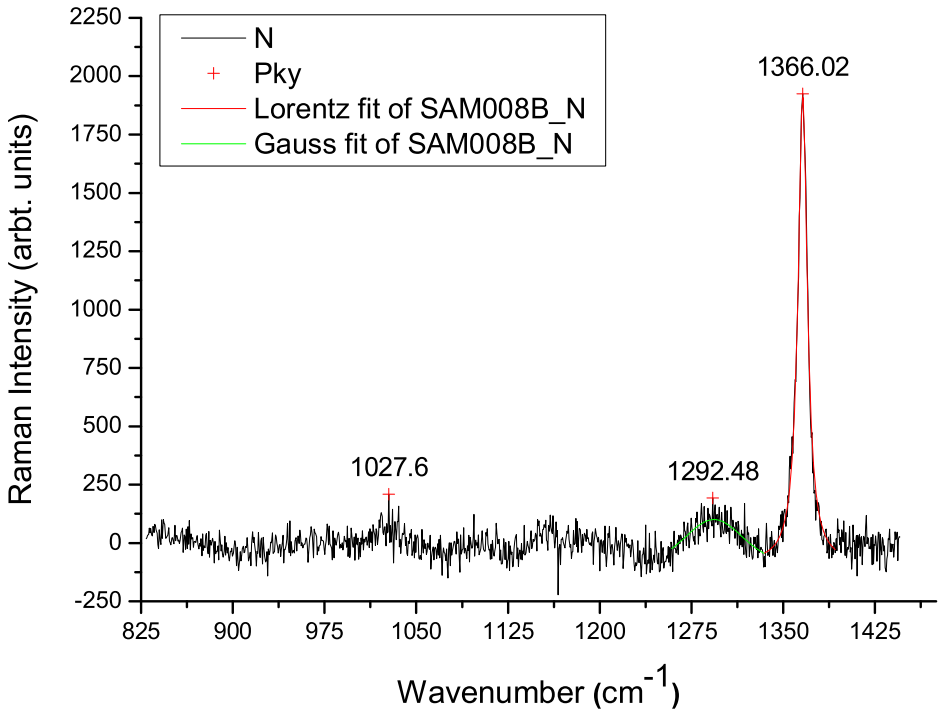

Figure 5.24: *One of the twenty μ–Raman profile measured at different points along an hBN sample surface that was implanted at 200 keV to fluences of 2.0×10^{16} ions/cm^2.*

Discussion

The expected intense Raman peaks are observed on either extreme of the spectra, outside the implanted regions. The Raman spectra measured in the implanted section of the samples, in both cases, are heavily attenuated. This is expected given the sample surface degradation as a result of implantation. However, the absence of other dominant features that were observed for He^+ implantations at 1.2 MeV and 500 kev (around 760cm^{-1} and 1290cm^{-1}) clearly shows that despite the massive irradiation, the initial *h*BN phase is retained. The evident darkness gradient of the implanted spot on the sample surface, and the observed unevenness of the individual, noisy μ–Raman spectra (e.g. fig 5.23) was attributed to the fact that the sample surfaces were not implanted uniformly as a consequence of two possible phenomena whose effects are characteristic of low energy ion implantations and/or their combination; firstly, the space–charge effect (see Section *4.3.2*) and secondly, the build-up of surface charge during implantation at low energies resulting in the repulsion of incoming ions by the surface being implanted.

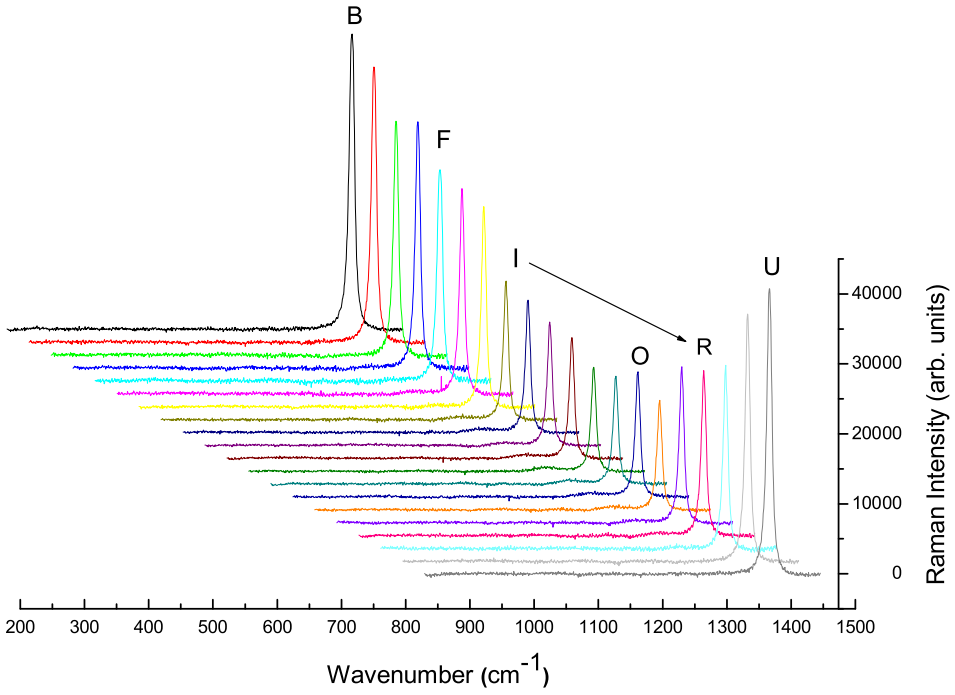

Figure 5.25: *The μ–Raman spectra measured at twenty different points in a single line along the irradiated sample's diameter for the sample that was implanted with 200 keV H^+ ions to fluences of 1.0×10^{15} ions/cm^2.*

5.3.7 200 keV H^+ implanted *h*BN

μ–Raman and Discussions

For purposes of comparison, some *h*BN sample were implanted with H^+ particles at 200 keV to fluences of 2.0×10^{16} and 2.0×10^{16} ions/cm^2. As before, the μ–Raman measurements were taken at twenty different points along a single line across the implanted region. Figs 5.25 and 5.26 show the μ–Raman profiles measured from all the twenty points from the samples that were implanted to doses 1.0×10^{15} and 2.0×10^{16} H^+ ions/cm^2, respectively. The peaks appearing on each extreme were measured on the unimplanted region. Fig 5.27 shows the μ–Raman spectrum measured inside the implanted region of the sample that was irradiated to fluences of 2.0×10^{16} H^+ ions/cm^2.

Unlike spectra measured for He^+ implanted samples where the Raman scattered signal were heavily attenuated; the profiles observed for the H^+ implanted samples show that there was less radiation damage on the sample surface. The measured μ–Raman

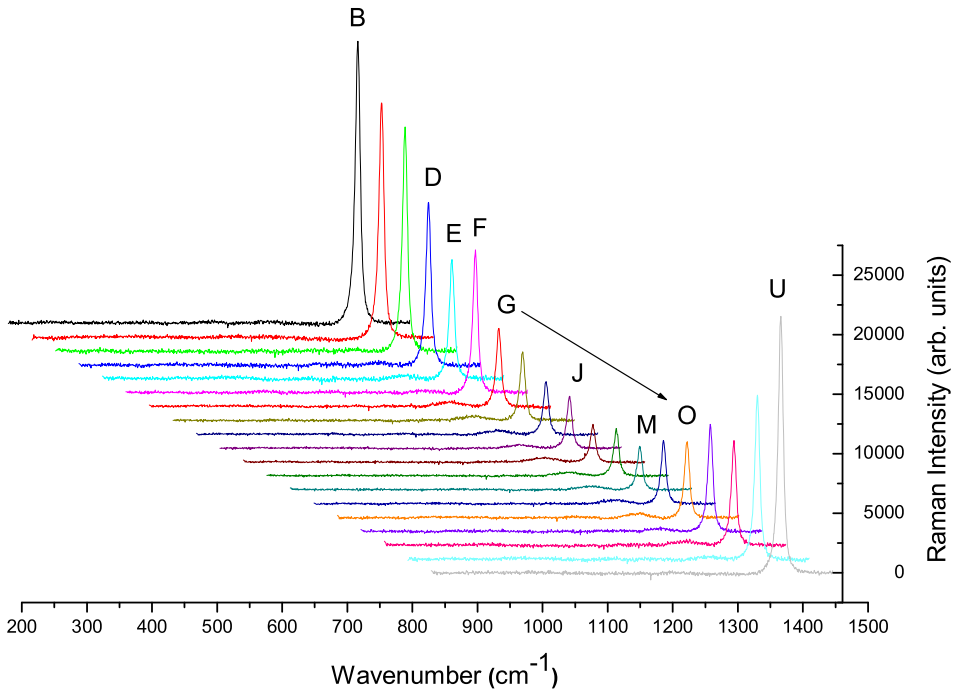

Figure 5.26: *The μ–Raman spectra measured at twenty different points in a single line along the irradiated sample's diameter for the sample that was implanted with 200 keV H^+ ions to fluences of 2.0×10^{16} ions/cm^2.*

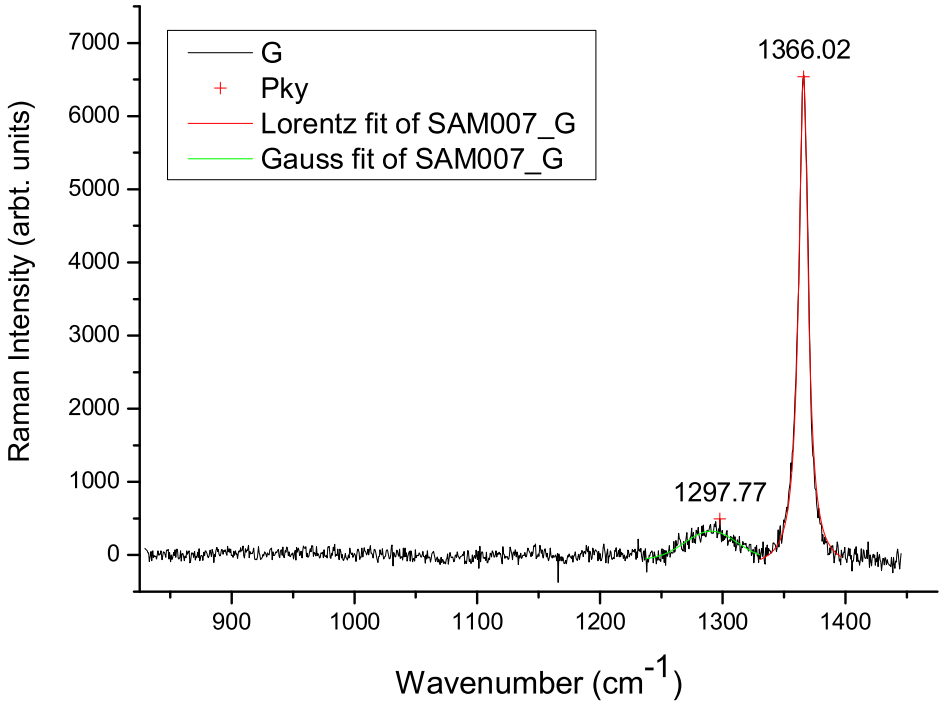

Figure 5.27: *The μ–Raman spectrum measured at an arbitrary point, inside the irradiated sample region for the sample that was implanted with 200 keV H^+ ions to fluences of 1.0×10^{15} ions/cm^2.*

spectra are similar to those that have been observed before. From the spectra, its evident the implanted region remains predominantly *h*BN. A significant Gaussian-shaped peak centred at 1290.13cm^{-1} is observed in fig 5.27. As seen in the previous discussions, the Gaussian-shaped peak is observed to be confined only to the implanted sections of the sample.

5.4 XRD Measurements

5.4.1 Unimplanted *h*BN

$\theta - 2\theta$–XRD and GIXRD

Powder diffraction $\theta/2\theta$ measurements were carried on virgin samples using the Bruker AXS Advanced D8 diffractometer. The instrument was run with the following settings and measurement conditions: Start Position [°2Th.]: 5,0100, End Position [°2Th.]: 89.997,

Step Size [°2Th.]: 0,0210.

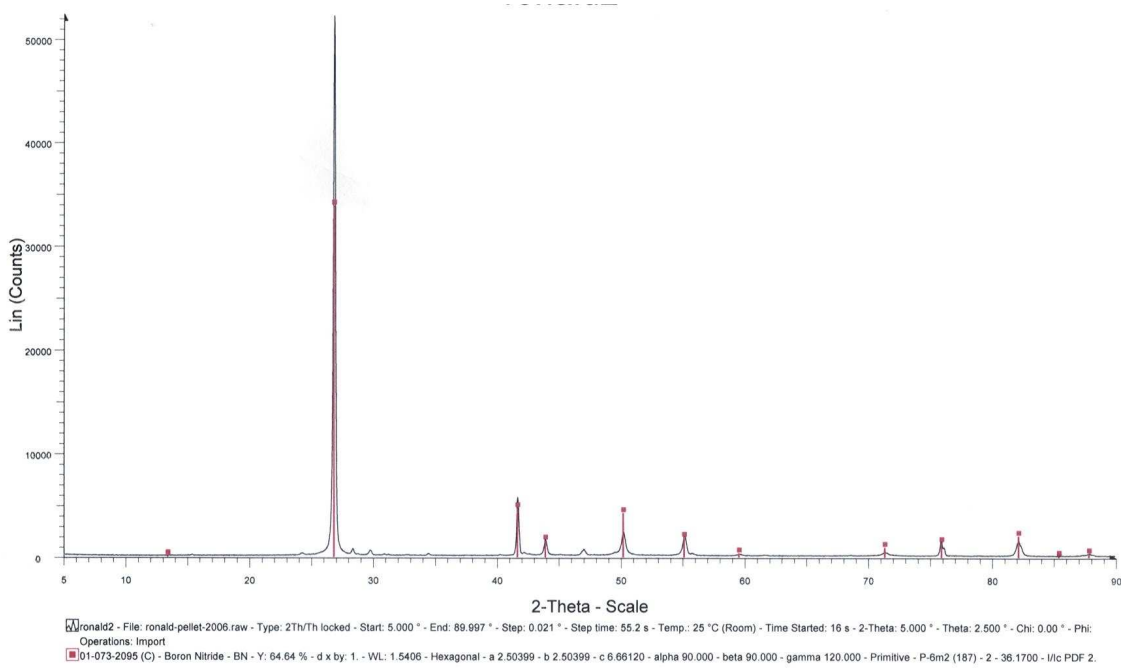

Figure 5.28: *The XRD line profile of unimplanted hBN samples (the black line) the red lines show the software matched peaks showing the positions where the documented hBN peaks should appear. Please note that the legend may not be legible on printed copies.*

The observed XRD line profile is shown in fig 5.28. The black line shows the XRD spectrum as obtained from the experiments whilst the red 'markers' show peak positions that the Bruker DIFFRAC^{plus} EVA software matched with the documented peak positions of *h*BN whose lattice parameters are $a = 2.5$Å and $c = 6.66$Å [74]. The matched peaks appear at the following peak positions: 26.8°, 41.6°, 43.9°, 50.0°, 59.5°, 71.3°, 75.9°, 81.1°, 85.3°, and 87.7°. There are, however, some unidentified peaks around 24°, 28.5°, 29.7° and 47°. Their intensities are small as compared to the dominant peaks; for the purposes of this work, they can be considered as insignificant.

The powder diffraction line profile obtained from GIXRD measurements is shown in fig 5.29. The measurements were done at 1° grazing incidence angle over a 20 hour exposure. The line profile is corrected for instrument drift and it shows a diffraction peak centred around 27° which is characteristic of the $h\text{BN}_{(002)}$ plane.

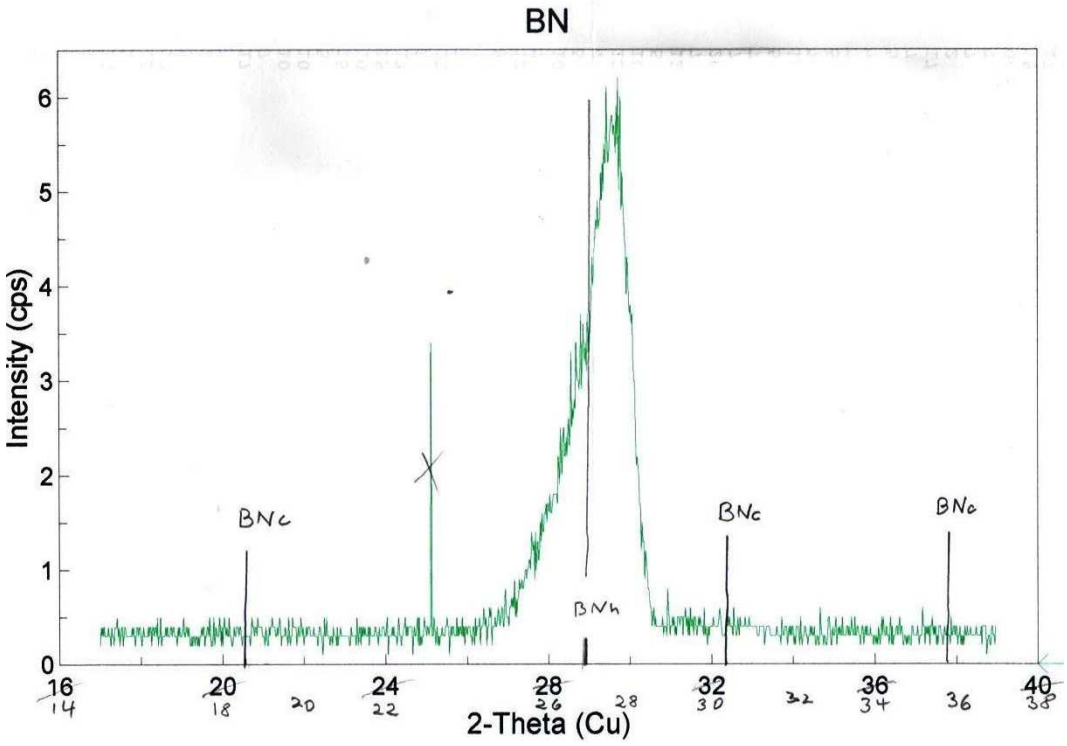

Figure 5.29: *The grazing angle XRD spectrum of unimplanted hBN collected at 1° grazing incidence and 20hours exposure (the spectrum is corrected for instrument drift).*

Discussions

The XRD line profile, fig.s 5.28, show narrow peaks appearing at the following peak positions: 26.8°, 41.6°, 43.9°, 50.0°, 59.5°, 71.3°, 75.9°, 81.1°, 85.3°, and 87.7°. The peak positions correspond to the following lattice planes: $h\mathrm{BN}_{(002)}$, $h\mathrm{BN}_{(100)}$, $h\mathrm{BN}_{(101)}$, $h\mathrm{BN}_{(102)}$, $h\mathrm{BN}_{(110)}$, and $h\mathrm{BN}_{(112)}$, respectively [45]. Unidentified peaks around 24°, 28°, 30°, and 47° have been observed. Their intensities are however much smaller as compared to the dominant peaks; for the purposes of this work, they can be considered as insignificant.

The GIXRD line profile, fig 5.29, shows that the material under investigation is predominantly hexagonal. The instrument used to carry out these measurements was still under calibration.

The Raman spectroscopy, XRD, and GIXRD measured results obtained are complementary; its evident that the samples under characterization are nominally–pure, they have minimum internal stresses and the material inhomogeneities are insignificant.

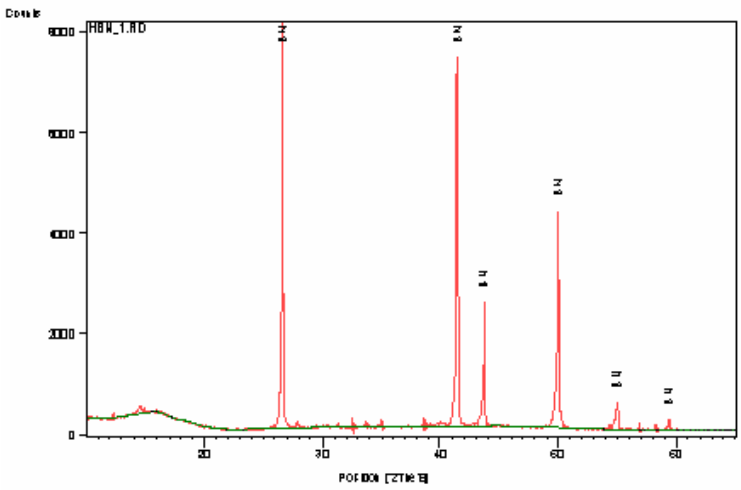

Figure 5.30: *The XRD spectra of hBN samples implanted with alpha particles to a fluence of* 1.0×10^{15} *ions/cm*^{2}.

5.4.2 1.2 MeV He^+ implanted *h*BN

$\theta - 2\theta$ XRD and GIXRD

$\theta - 2\theta$ XRD measurements were done on the implanted samples using the Philips PW1710 diffractometer. The measurements were carried out under the following instrument settings and measurement conditions: Start Position [°2Th.]: 10,0100, End Position [°2Th.]: 65,1300, Step Size [°2Th.]: 0,0200, Anode Material: Cu, Generator Settings: 40kV, 20mA, Goniometer Radius [mm]: 173,00.

The diffraction line profile measured for the 1.0×10^{15} ions/cm^2 implanted sample is shown in fig 5.30. The dominant and narrow peaks were observed at the following peak positions: 26.65°, 41.46°, 43.72°, 50.01°, 55.00° and 59.37°.

The diffraction line profile measured for the 1.0×10^{16} ions/cm^2 implanted sample is shown in fig 5.31. Dominant and narrow peaks were observed at the following peak positions: 26.61°, 41.42°, 43.68°, 49.97°, 54.96° and 59.34°.

The peaks positions are well documented and correspond to the *h*BN phase. The diffraction patterns (fig 5.30 and 5.31) are fairly similar. However, peak positions in fig 5.31 are slightly down-shifted and the peak intensities have decreased significantly. In addition to this, some small peaks: 48.85°, and 60.5° cropped up in fig 5.31, they could not be matched to *h*BN or any other BN modification.

The line profile observed from the GIXRD measurements is shown in fig 5.32. Dom-

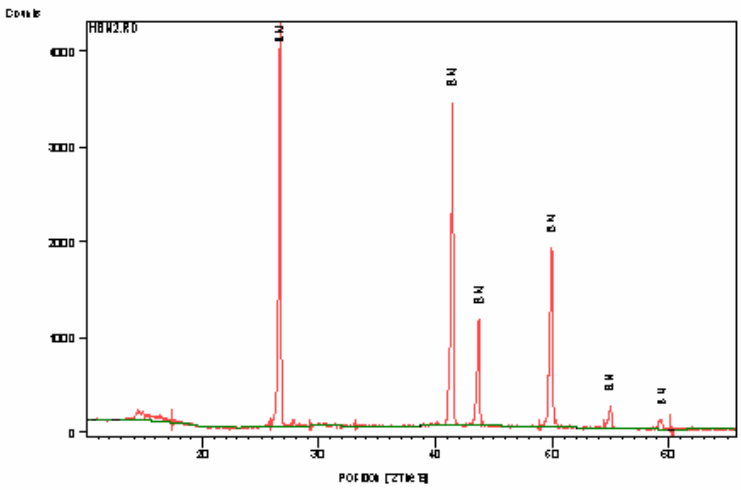

Figure 5.31: *The XRD spectra of hBN implanted with 1.2 MeV alpha particles at a* 1.0×10^{16} *ions/cm*^{2} *ion fluence.*

inant peaks were observed at the following peak positions: 26.8°, 41.8°, 43.0°, 47.0°, 49.4°, and 50.2°.

Discussion

The lattice parameters of hBN were determined to be 2.5Å and 3.33Å. The peak positions are well documented and correspond to the *h*BN phase [84] - (see also the discussion 5.2.4). XRD measurements carried out using the Bruker AXS Advanced D8 diffractometer produced a line profile similar to fig 5.28. Given the results obtained from the XRD measurements (fig.s 5.28, 5.30, 5.31, and 5.32) it is suggested that the amount of the radiation damage and the Raman detected phases (*r*BN and amorphous/crystalline boron clusters) is below the 5% detection limit.

5.4.3 500 keV He^+ implanted *h*BN

$\theta - 2\theta$ **XRD**

XRD measurements were done on the samples; the experiments were carried out using the Bruker AXS Advanced D8 diffractometer. The instrument was run with the following settings and measurement conditions: Start Position [°2Th.]: 5,0100, End Position [°2Th.]: 89.997, Step Size [°2Th.]: 0,0210.

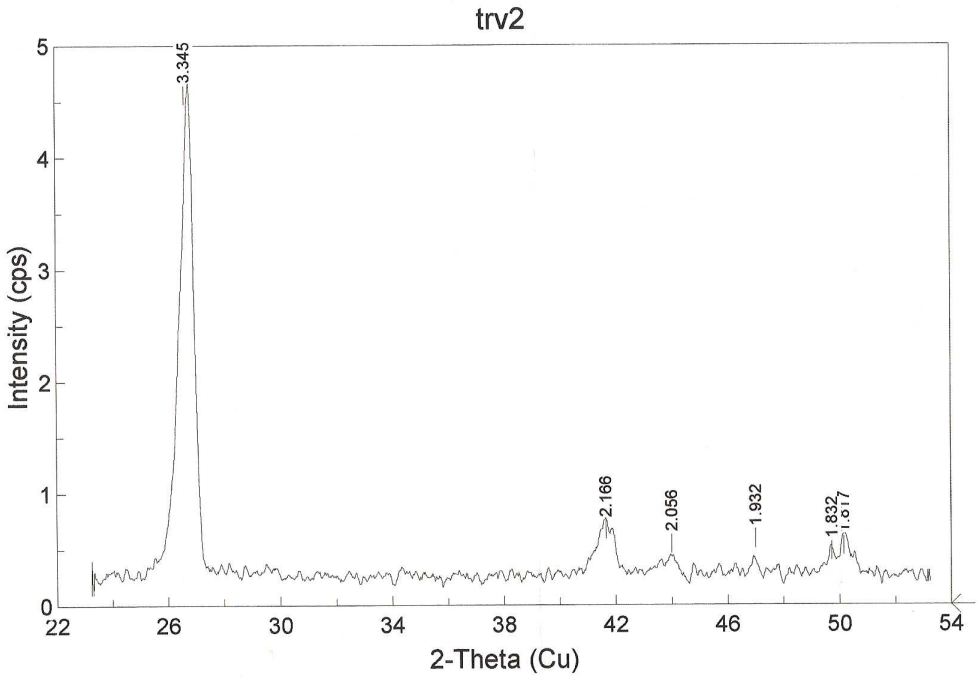

Figure 5.32: *The grazing angle XRD spectrum of implanted hBN collected at 1° grazing incidence and 20hours exposure*

The diffraction line profile obtained for the 2.0×10^{16} ions/cm^2 implanted sample is shown in fig 5.33. The dominant and narrow peaks were observed at the following positions: 27.0°, 41.8°, 44.2 °, 50.5°, 55.5° and 59.7°. The peak positions matched peak positions for *h*BN documented in the reference [84].

Discussion

The XRD diffraction pattern realized from measurements on the sample implanted to a fluence of 2.0×10^{16} ions/cm^2 (fig 5.33) shows peaks that are characteristic of the *h*BN phase [74]. However, the diffraction pattern peaks are evidently much broader than those obtained from XRD measurements on virgin and 1.2 MeV He^+ implanted samples (fig 5.28). A quick *SRIM2006* simulation of 500 keV He^+ implanted into *h*BN shows that the ion range is approximately 1.3μm and the mean projected range about 670Å. A similar simulation for 1.2 MeV He^+ shows an ion range of approximately 2.60μm and the mean projected range about 750Å, see also the discussion in Section *5.2.1.* Evidently, as the ion implant energy decreases the ion range becomes shallower whilst the nuclear stop-

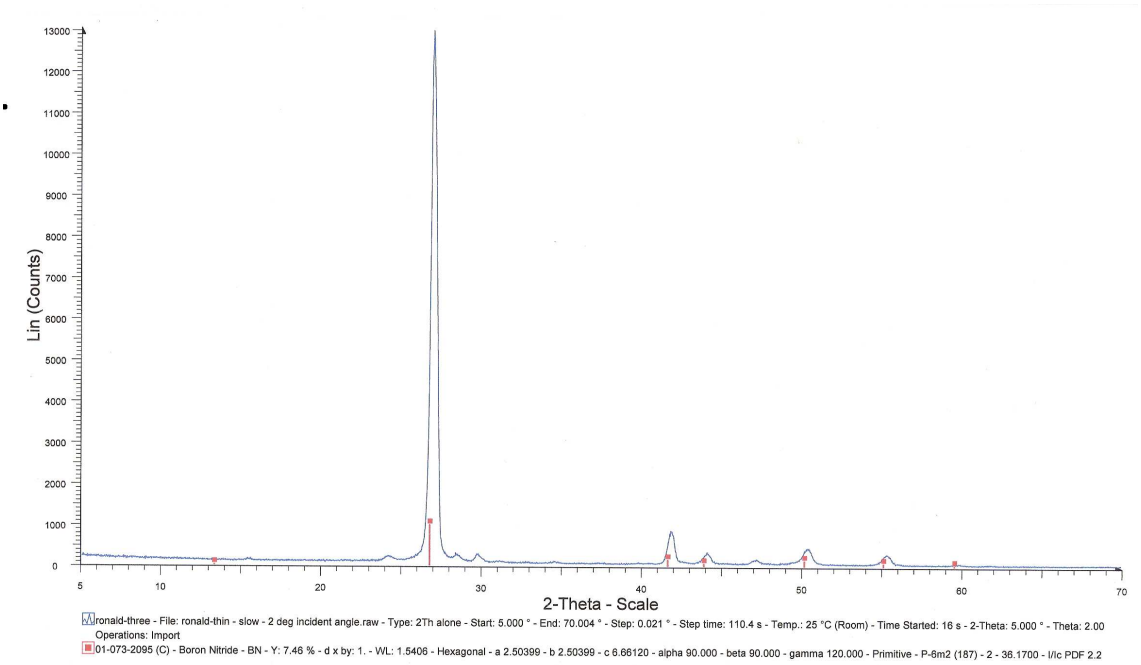

Figure 5.33: *The diffraction line profile obtained for the 2.0×10^{16} ions/cm^2 implanted hBN sample is shown in figure. Please note that the legend may not be legible on printed copies.*

ping which is the mechanism of extensive damage moves closer to the surface. Thus the broadening observed at lower energies is evidence of the shallow radiation–induced damage. However, the n-*c*BN phase, observed in Raman scattering measurements, was not detected in these XRD measurements, we suspect because the amount of the transformed material was probably well below the 5% detection limit of the diffractometer.

Chapter 6

Summary

Due to the very high detection limit of the XRD diffractometer used as well as the low x-ray scattering factor of the *c*BN nanocrystals (only 5% or more of the transformed *c*BN can be detected), μ-Raman and 2D-Raman scattering measurements were the main characterization techniques used in this work to identify the possible occurrence of the phase transformation.

FIG.	ION	ENERGY , DOSE (keV, ions/cm^2)	$I_{Lorentzian}$ (arbt. units)	$I_{Gaussian}$ (arbt. units)	I_G/I_L	Γ (cm^{-1})
5.25	H	200 , 1.0×10^{15}	—	—	—	—
5.27	H	200 , 2.0×10^{16}	22000.0	493.093	0.02241	1290.13
5.23	He	200 , 1.0×10^{15}	22647.1	—	—	—
5.24	He	200 , 5.0×10^{15}	22827.4	163.9	0.00718	1292.48
5.21	He	350 , 1.0×10^{15}	21352.0	—	—	—
5.22	He	350 , 2.0×10^{16}	18447.7	108.1	0.00586	1280.03
5.15A	He	500 , 2.0×10^{16}	43000.0	*	*	1292-1298
5.15B	He	500 , 1.0×10^{17}	40000.0	60	0.00150	1290-1300
5.14	He	750 , 2.0×10^{16}	28382.4	126.7	0.00446	1295.92
5.9	He	1200 , 1.0×10^{15}	18600.0	—	—	—
5.10	He	1200 , 2.0×10^{16}	26000.0	200	0.00769	1296.6

Table 6.1: *A summary of the μ-Raman and 2D-Raman results presented in Chapter 5. Γ is the position/wavenumber of the n-cBN Gaussian peak. The Gaussian peaks were normalized to the Lorentzian peaks that were measured outside the irradiated spot. * means the measured values were erroneous due to detector saturation.*

Ideally, the Raman spectrum of single crystal *c*BN exhibits two strong Lorentzian-shaped lines representing the Brillouin zone centre transverse-optical phonon mode and the longitudinal-optical phonon mode (at 1057cm^{-1} and 1306cm^{-1}, respectively. The *h*BN phase also exhibits two Lorentzian-shaped phonon modes that are attributed to the E_{2g} symmetry vibration at 52cm^{-1} (this is usually a tiny, sharp peak) and at 1367cm^{-1} (principal peak used for characterization). The broad Raman phonons observed around Ωcm^{-1} have been attributed to the presence of nanocrystals of *c*BN. The deviation from the ideal Lorentzian lineshapes have been observed by other researchers before and has been attributed to the phonon confinement effects.

Results obtained from the Raman scattering measurements carried out on He^+ and H^+ implanted *h*BN are summarized in table 6.1. Two graphs, fig 6.1 and fig 6.2 have been drawn from the values in the table.

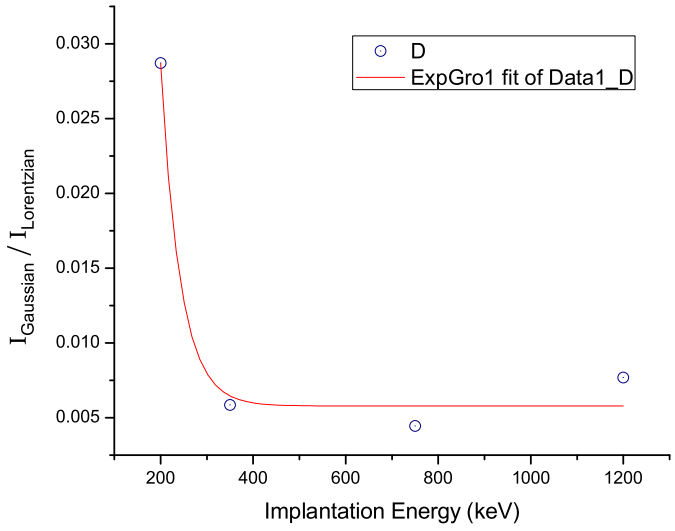

Figure 6.1: *The graph shows the normalized intensity of the Gaussian peaks plotted against the implantation energy. Note that for 200 keV He^+ the plotted value is an estinate; four times measured values, since the implantation dose at this energy is a quarter of 2.0×10^{16} ions/cm^2.*

Fig 6.1 shows the graph of the normalized n-*c*BN Gaussian peak intensities plotted against the implantation energies. The Gaussian peaks were normalized to the principal *h*BN Lorentzian peaks that were measured outside the irradiated spot.

- I_G/I_L roughly quantifies/estimates the amount of the *c*BN nanocrystals present in the implanted sample.

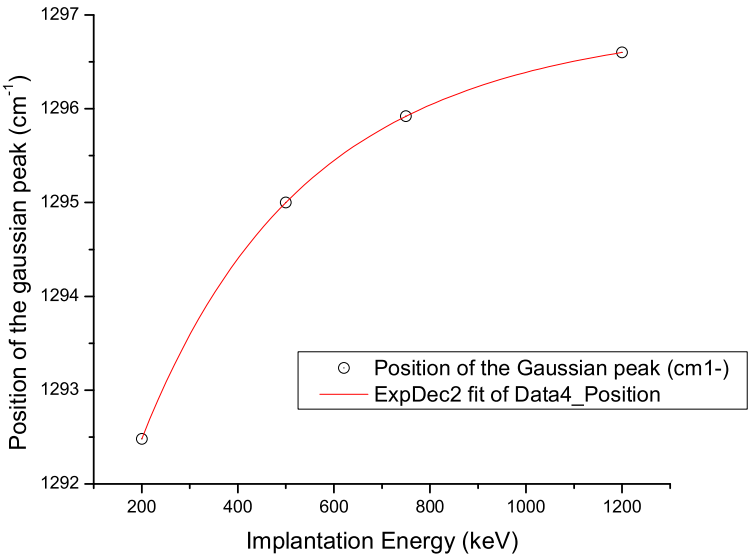

Figure 6.2: *The position/wavenumber of the n-cBN Gaussian peaks plotted against the implantation energy.*

- Greater quantities of the *c*BN nanocrystals are observed towards 200 keV. Given the SRIM2006 damage profiles (see fig 5.1 and 5.2), it appears that as the ion energy decreases the elastic damage profile comes closer to the surface to within the penetration depth of the probing Raman laser beam.

- The steep gradient of the plot towards the low implantation energies has been attributed to nuclear stopping induced phase transformation; that of the gentle slope towards the higher energies, to electronic stopping induced transformations.

Fig 6.2 shows the graph of the position of the Gaussian peaks plotted against the implantation energies.

- The plot is a second order exponential decay curve that shows an indication of saturation around 1300cm^{-1}. This might suggest that the nanocrystals observed at lower energies (thus nuclear stopping induced) are characterized with considerable disorder compared with those obtained at higher energies.

Chapter 7

Conclusions and Outlook

The possibilities of using ion implantation as a technique of introducing defects into *h*BN in order to influence a low–activation energy *h*BN–to–*c*BN phase transformation, under less extreme conditions, were investigated. Ion beam induced phase transformations to other BN modifications were also investigated. SEM, μ-Raman and 2D-Raman measurements, and XRD measurements were used to characterize the He^+ implanted samples.

The results obtained in this study show that nanocrystals of *c*BN (n-*c*BN) were successfully produced at room temperature by He^+ implantation of *h*BN at energies between 200keV and 1.2MeV for fluences of up to 10^{17} ions/cm^2. The conditions under which the n-*c*BN phase nucleates were beyond the scope of this study. However, there is a possibility that the transformation progresses as illustrated in fig 3.4 or from the disordered *h*BN phase.

- According to the plots fig 6.1 and 6.2 in Chapter 6, the *h*BN–to–*c*BN phase transformation was observed to be more favourable towards the low energies of implantation. This strongly suggests that the *h*BN to *c*BN phase transformation is greatly influenced with the nuclear stopping criteria.

- The optimum dose that influences the phase transformation was observed to be of the order of 10^{16} ions/cm^2. Implantations at doses above the optimum dose (of the order of 10^{17}) were observed to damage the sample extensively whilst implantations performed at a dose below the optimum dose, even at higher energies were observed not to have influenced the *h*BN to *c*BN phase transformation in any significant way.

- In addition to the n-*c*BN phase, structural transformations to the *r*BN and *a*BN

phases were observed. Amorphous/crystalline boron clusters, probably due to excess boron in the implanted region, were also observed. These were only observed for implantations done at 1.2MeV.

- The origins of the *h*BN-to-*r*BN transformation were attributed to the lateral shearing/shifting of the basal planes in response to the implantation induced stresses which results in slight changes in the packing sequence between the initial and final phases. The *a*BN phase observed (a phase which is characterized by atomic level disorder) was attributed to implantation induced disorder due to nuclear stopping. The observed amorphous/crystalline boron clusters were attributed to the agglomeration of elementary boron in the disordered phase or a result of excess boron following the evolution of nitrogen gas molecules.

For future research, we suggest the use of low energy implantations with heavier ion species such as O^+, N^+, C^+, and Ar^+ to investigate the nature of this phenomenon. We also suggest further theoretical modelling and experimental work to be focussed on the concise understanding of the dynamics and nature of the *h*BN to *c*BN structural transformation. In addition, the characterization of *c*BN is nontrivial; the conclusive phase and crystallinity identification requires application of several techniques including Infrared reflectance spectroscopy, Fourier-transform infrared spectroscopy, electron and X-ray diffraction, transmission electron microscopy, electron energy-loss spectroscopy, and possibly synchrotron radiation based methods to complement the μ-Raman and 2D-Raman scattering measurements.

Appendix A

Raman Spectroscopy Theory

A.1 Introduction

The Appendix discusses the theory of Raman scattering process. The discussion is partly based on the series of lectures presented by RM Erasmus [85] and S. Ndiaye [86].

When a material is illuminated, some light will be transmitted, some will be absorbed and a very small fraction will be scattered. The scattering is a result of inhomogeinities in the material such as molecular vibrations and defects. Most of the scattered light will be scattered elastically, that is the frequency and energy of the incident and the scattered light will be the same. This scattering process is called *Rayleigh scattering*. An even smaller fraction of the scattered light, typically about 10^{-7}, will be inelastically scattered. This scattering process is known as the *Raman effect*. The incident light radiation undergoes an energy change, the difference between the incident light energy E_{inc} and the energy of the Raman scattered light is equal to the energy involved in changing the molecule's vibrational state from ν_i to ν_j and the energy difference is called the Raman shift [ref]. In other words the shift in frequency of the incident light is due to the interaction of the photons of light with the phonons (vibrations and rotations of the molecules) in the material being investigated [60].

Raman spectroscopy is a non–destructive characterization technique that is based on analyzing the Raman scattered light. The Raman shift profiles (data plots of intensity against frequency/wavenumber) that are drawn from the Raman spectroscopy gives information on the vibrational spectrum of material, this can be used to 'fingerprint' the phase structure of the material because the vibrational spectrum is unique and characteristic of a unique bonding environment [30]. In this work Raman spectroscopy is an important

tool that detects the structural modifications that are brought about by the implantation of different ionic species as well as the structural stresses that correspond to them most importantly, it is a vital tool in revealing the possible occurrence of a phase transformation [30]. The Raman spectroscopy also gives information on the material's chemical composition, phase structure, an estimate of the grain size (for polycrystalline materials) and temperature [83].

A.2 Raman Effect

Raman scattering is primarily concerned with lattice dynamics. It can be treated in two ways, either classically or quantum mechanically.

A.2.1 Classical Treatment

Classically, the Raman effect can be viewed as arising from the interaction of the incident electromagnetic radiation with the dipole moment of the molecules of the illuminated material. Both the oscillating electric and magnetic field components of the electromagnetic radiation are capable of interacting with the molecule but the magnetic component has a negligible effect on the molecule's dipole moment.

When a polarizable molecule is exposed to an external oscillating electric field, $\vec{E}_j$, the molecule's equilibrium electronic distribution changes. As a result, induced dipoles are created around molecules. If the induced dipoles, under the influence of the external electric field, undergo a normal molecular vibration; the induced dipoles can cause radiation. The aim in Raman spectroscopy is to excite these induced molecular vibrations to gain information on the bonding environment of the molecules in the material.

The external oscillating electric field of incident frequency, ω_{inc}, the position vector, $\vec{r}$, the wavevector, $\vec{q}_{inc}$, and time t can be expressed as:-

$$\vec{E}_j = \vec{E}_j^o \cdot \cos(\vec{q}_{inc} \cdot \vec{r} - \omega_{inc} t) \tag{A.1}$$

The normal coordinate, ξ_k, of the molecular vibration is characterized by the normal frequency, ω_k, and wavevector, $\vec{q}_k$. The normal coordinate can be represented as:-

$$\xi_k = \xi_k^o \cos(\vec{q}_k \cdot \vec{r} - \omega_k t) \tag{A.2}$$

The induced dipole moment, μ_i, can be described in terms of a power series of of the influencing external electric field and the ease of polarization of the molecules, the

polarizability (α). Equation A.3 shows that in practice, μ_i is a non-linear quantity. The non-linearity is a result of the anisotropy, a property of the illuminated material.

$$\mu_i = \mu_i^{(1)} + \mu_i^{(2)} + \mu_i^{(3)} + (\text{ 'higher order terms' }) \tag{A.3}$$

where $\mu_i^{(m)}$ is given by:-

$$\begin{aligned} \mu_i^{(1)} &= \tilde{\alpha}_{ij} E_j \\ \mu_i^{(2)} &= \frac{1}{2}\tilde{\beta}_{ijk} E_j E_k \\ \mu_i^{(3)} &= \frac{1}{6}\tilde{\gamma}_{ijkl} E_j E_k E_l \end{aligned} \tag{A.4}$$

E_j, E_{jk}, and E_{jkl} are components of the exciting electric field. Whilst, $\tilde{\alpha}_{ij}$, $\tilde{\beta}_{ijk}$, and $\tilde{\gamma}_{ijkl}$ are all different polarization tensors of the 2^{nd}, the 3^{rd}, and the 4^{th} rank respectively. Polarizability is an intrinsic property of a material. The variation of the instantaneous polarizability tensor, $\tilde{\alpha}_{ij}$, with the normal vibration is non-linear and given in equation A.5 as a Taylor series. The 'higher order terms' arise from the first and second order hyper–polarizability tensors; $\tilde{\beta}_{ijk}$ and $\tilde{\gamma}_{ijkl}$ (whose magnitudes are both very small compared to the polarizability tensor, $\tilde{\alpha}_{ij}$):-

$$\alpha_{ij}(\omega_{inc}, q_k) = \alpha_{ij}^o(\omega_{inc}) + \left(\frac{\partial \alpha_{ij}(\omega_{inc}, q_k)}{\partial \xi_k}\right) \cdot \xi_k + (\text{ 'higher order terms' }) \tag{A.5}$$

From equations A.1, A.2, A.4, and A.5, the induced dipole moment (equation A.3) of a molecule under the influence of electromagnetic radiation becomes:-

$$\begin{aligned} \vec{\mu}_i = \Big[\tilde{\alpha}_{ij}^o(\omega_{inc}) + \left(\frac{\partial \tilde{\alpha}_{ij}(\omega_{inc}, q_k)}{\partial \xi_k}\right) \cdot \xi_k^o \cos(\vec{q}_k \cdot \vec{r} - \omega_k t) \\ + (\text{ 'higher order terms' })\Big] \cdot \vec{E}_j^o \cos(\vec{q}_{inc} \cdot \vec{r} - \omega_{inc} t) \end{aligned} \tag{A.6}$$

The '*first term*' in equation A.6 is simply the product of the polarizability in equilibrium configuration, $\tilde{\alpha}_{ij}^o(\omega_{inc})$ and the external electric field $\vec{E}_j$. The term is dependent only on the incidence radiation frequency, ω_{inc}; it relates to the elastic Rayleigh scattering of the incident radiation. It is the most probable process. The '*higher order terms*' referred to in equation A.6 are a result of the non–linear change in the polarizability arising from the non–linear anharmonic coupled molecular oscillations resulting in combinational frequencies, the term is also known as the Hyper–Raman scattering term.

The '*second term*' in equation A.6 is the term if greatest interest; it relates to the Raman scattering effect. When simplified it looks like:-

$$\frac{\partial\tilde{\alpha}_{ij}(\omega_{inc}, q_k)}{\partial\xi} \cdot \frac{\xi_k^o \cdot \vec{E}_k^o}{2} \cdot \Big\{ \cos[(q_{inc} + q_k) \cdot \vec{r} - (\omega_k - \omega_{inc})t\ )] + \cos[(q_k - q_{inc})\vec{r} - (\omega_{inc} - \omega_k)t\ ]\Big\} \tag{A.7}$$

The equation A.7 shows that the Raman scattering process is accompanied by a net $q_{inc} \pm q_k$ frequency shift. The frequency shift is characteristic of the molecule and provides a basis for Raman spectroscopy [87]. Of critical importance is the partial differential part of the term; $\frac{\partial\tilde{\alpha}_{ij}(\omega_{inc},q_k)}{\partial\xi}$ that gives the change in the spatial variation of the polarizability of the light excited molecule. This term is known as the classical Raman effect *selection rule*. If $\frac{\partial\tilde{\alpha}_{ij}(\omega_{inc},q_k)}{\partial\xi} \neq 0$, then the inelastically scattered Raman modes are observed with intensities proportional to the square of this term, else if this term is zero, then the molecule can not be polarized and the Raman effect can not be observed, in such a case the material is deemed Raman–inactive. If the polarizability of a molecule changes as it rotates or vibrates, incident radiation of frequency ω_{inc}, according to classical theory, should produce scattered radiation.

A.2.2 Quantum Mechanical Treatment

From a quantum mechanical perspective, the Raman effect can be considered, in principle, as a light–matter interaction where the incident photon interacts with the phonon in matter. The phonons can either be vibrational, rotational modes or a combination of both. The basis of this treatment comes from the understanding that the electronic, vibrational and rotational states of a molecule are considered to be quantized; fig A.1 illustrates this [ref]. The energy of a vibrational energy level depends on things like molecular structure, environment, atomic mass, bond order, molecular geometry and hydrogen bonding. All these affect the vibrational force constant which in turn dictates the vibrational energy.

The direct transition from one vibrational (or rotational) state ν_n to another $\nu_{n\pm1}$ gives rise to an IR spectrum and the direct transition from any state n to the virtual state[¶] and relaxation back to that state gives rise to the Rayleigh scattering, this process has a large cross–section. Raman scattering can arise as a result of a change in the vibrational or

[¶]an imaginary state lower than the real excited electronic state; that is, no stationary state of the molecule exists for this virtual energy state.

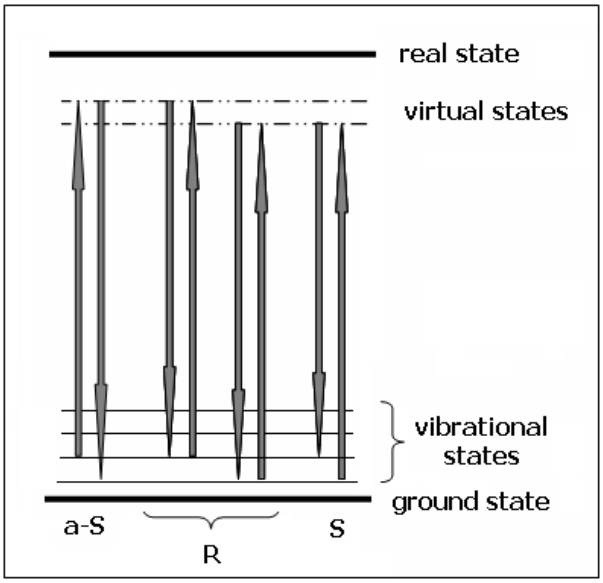

Figure A.1: *An illustration of the Rayleigh (R), anti-Stokes (a-S) and Stokes (S) Raman scattering processes, each electronic has several vibrational states, in turn, each vibrational state has several rotational energy states (not shown here).*

rotational or electronic energy states of a molecule in a vibrational state to a virtual state and the subsequent relaxation transition to another vibrational or rotational state almost simultaneously. The molecule can either gain or lose energy in the anti-Stokes and Stokes process respectively. The progression of the transition is governed by the quantum mechanical selection rules.

The scattering process is viewed as the creation and annihilation of vibrational excitations (phonons) by photons and the resultant Raman frequency shift equals the frequency of the phonon created or annihilated. It is perceivable that since the Raman effect is a two photon process. The permitted transitions are; for a vibrational transition $\nu = 1 \leftarrow 0$ (Stokes transition) and $\nu = 1 \rightarrow 0$ (anti-Stokes transition), hence the overall vibrational transitions obeys the $\Delta\nu = \pm 1$ selection rule. For rotational transitions, 'each rotational 'photon' transition obeys the $\Delta J = \pm 1$ transition, therefore it follows that the overall transition obeys $\Delta J = 0, \pm 2$, since this process is a two photon process where $\Delta J = 0$ corresponds to Rayleigh scattering, $\Delta J = 2$ to Stokes scattering and $\Delta J = -2$ to an anti–Stokes scattering transition. Where J is the total angular momentum quantum number and ν is the vibrational quantum number.

Appendix B

Some spectrum presented in the main text (fig 5.14 and fig 5.21 – 5.24) are extracts derived from a group of spectrum (fig B.1 – B.5, respectively, shown in this section for entirety) measured at twenty different points in a single line along the implanted sample's diameter.

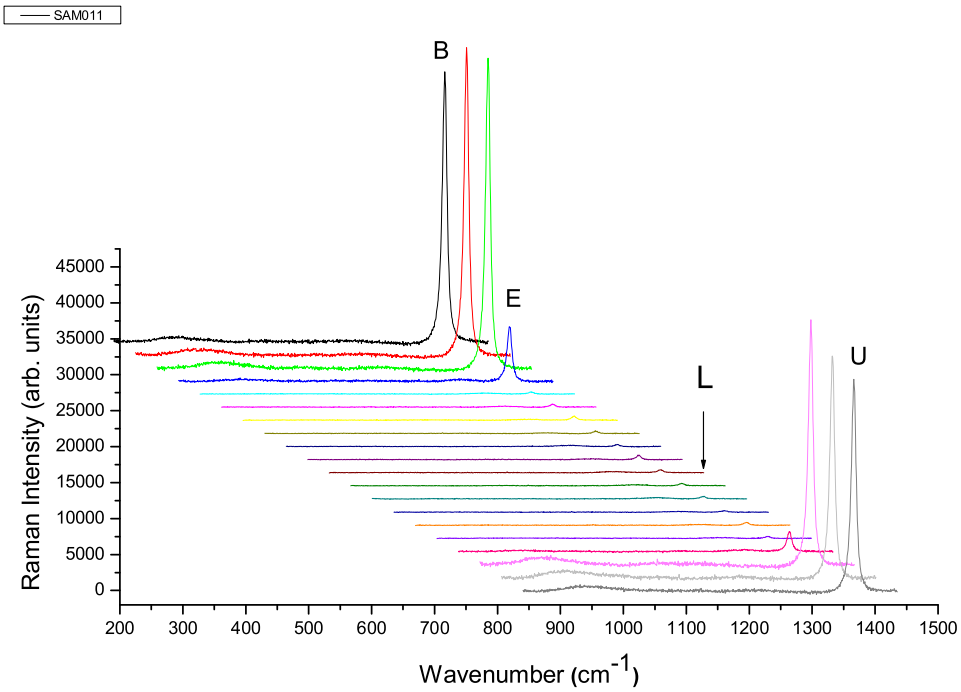

Figure B.1: *The μ–Raman spectra measured at twenty different points in a single line along the implanted sample's diameter. The hBN sample was implanted with 850 keV He^+ ions to a fluence of 2.0×10^{16} ions/cm^2. The spectrum marked L is shown in fig 5.14. Notice the severity of the Raman signal attenuation in the implanted sections.*

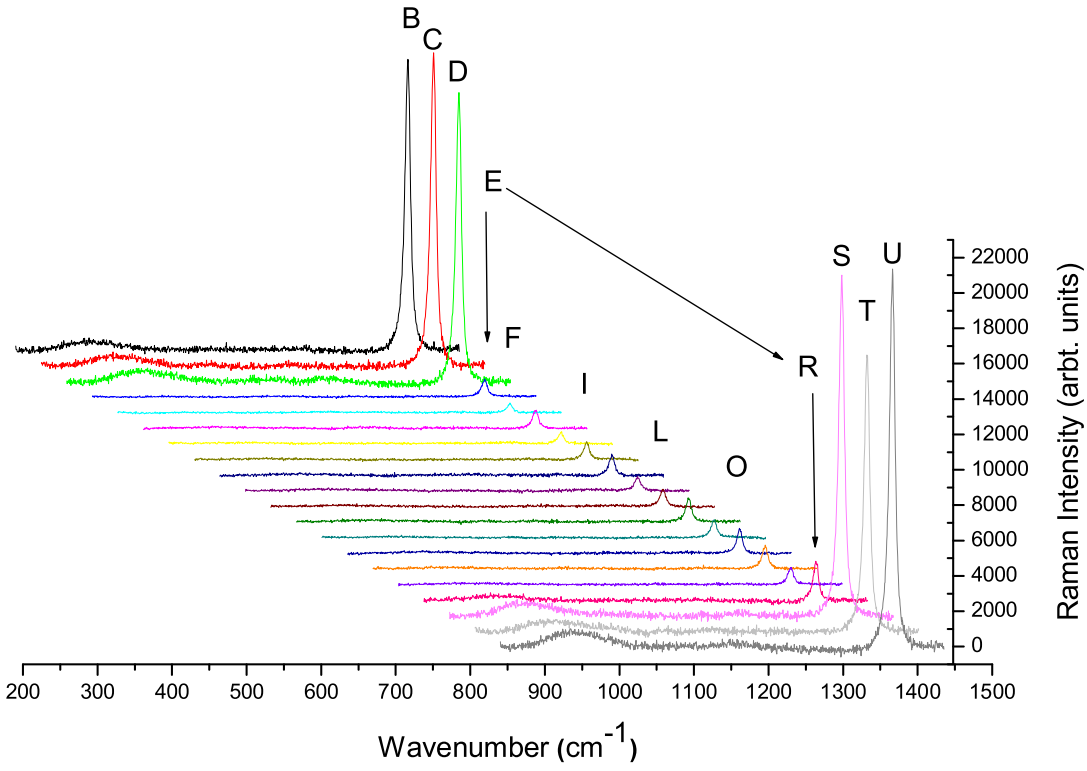

Figure B.2: *The μ–Raman spectra measured at twenty different points in a single line along the implanted sample's diameter. The hBN sample was implanted with 350 keV He^+ ions to a fluence of 2.0×10^{16} ions/cm^2. The spectrum marked R is shown in fig 5.21. Notice the absence of the Gaussian-shaped peak about 1285cm^{-1}.*

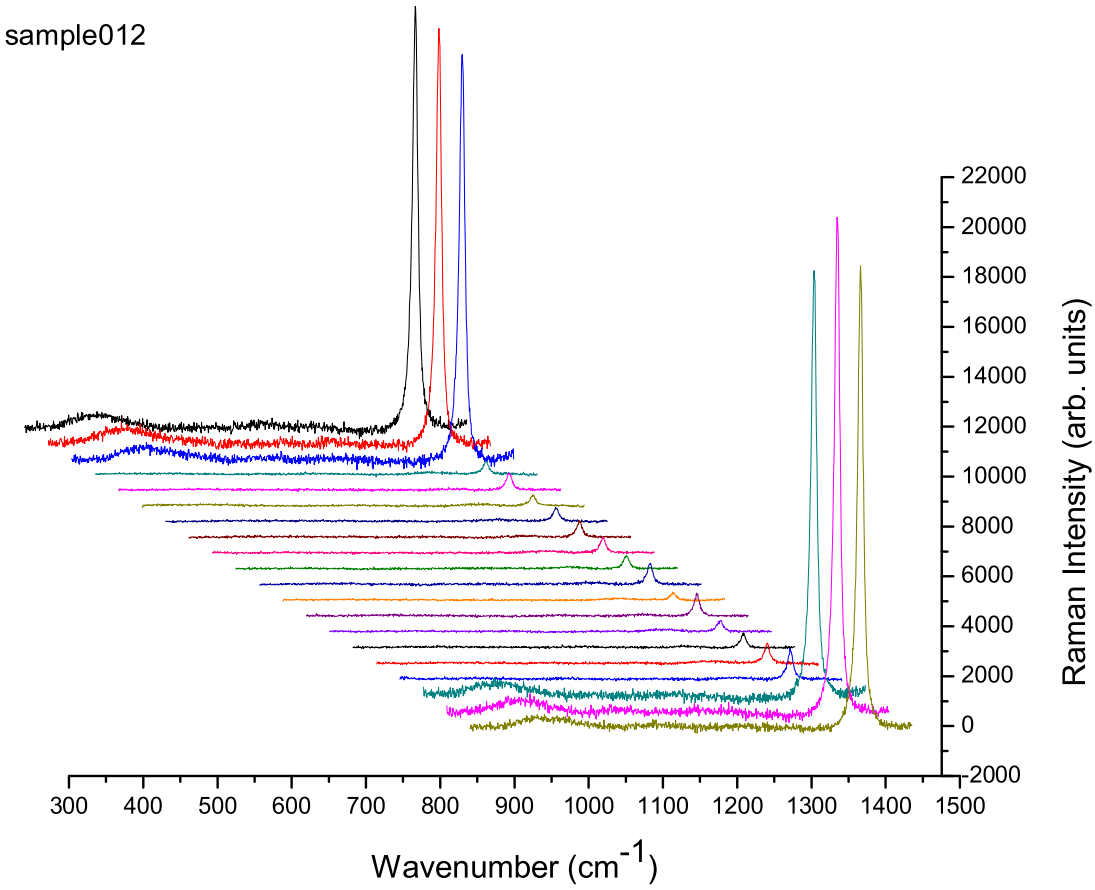

Figure B.3: *The μ–Raman spectra measured at twenty different points in a single line along the implanted sample's diameter. The hBN sample was implanted with 350 keV He^+ ions to a fluence of 2.0×10^{16} ions/cm^2.*

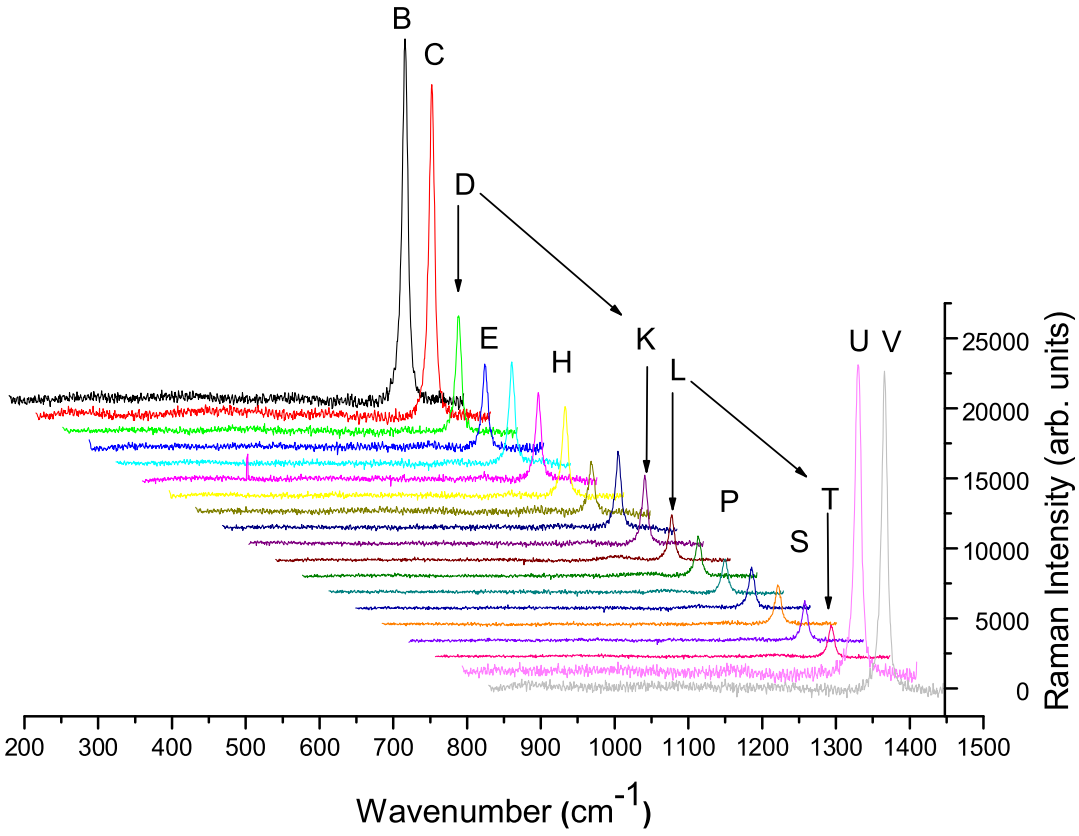

Figure B.4: *The μ–Raman spectra measured at different points as a function of position across the implanted diameter of an hBN sample implanted to fluences of* 1.0×10^{15} He^{+}/cm^{2} *at 200keV.*

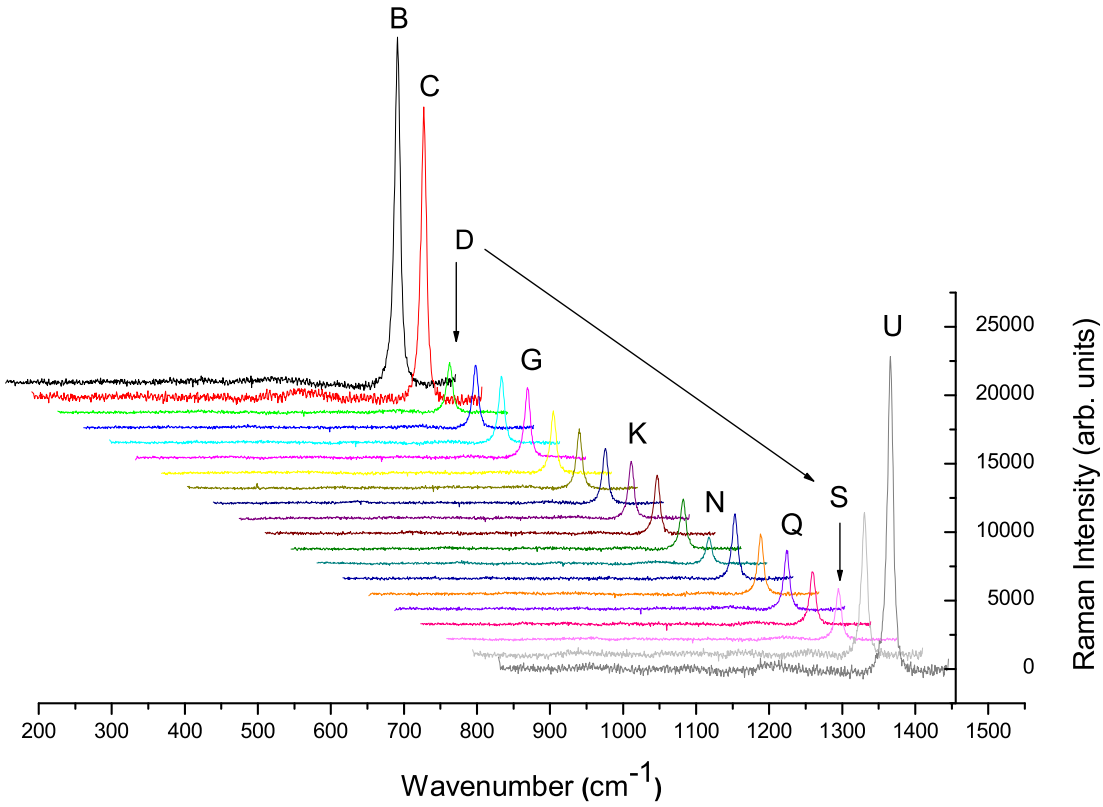

Figure B.5: *The μ–Raman spectra measured at different points as a function of position across the implanted diameter of an hBN sample implanted to fluences of* 5.0×10^{15} He^{+}/cm^{2} *at 200keV.*

Bibliography

[1] J. F. Prins, *Ion-implanted structures and doped layers in diamond*, Mater. Sci. Rep. **7**, 271 (1992).

[2] J. S. Williams, *Materials modification with ion beams*, Rep. Prog. Phys **9**, 491 (1986).

[3] M. S. Dresselhaus and R. Kalish, *Ion Implantation in Diamond, Graphite, and Related Materials*, Springer Series in Material Science 22, Springer - Verlag, 1992.

[4] M. Nastasi, J. Mayer, and J. K. Hirvonen, *Ion-Solid Interactions: Fundamentals and Applications*, Cambridge University Press, 1996.

[5] F. Banhart, *Irradiation effects in carbon nanostructure*, Rep. Prog. Phys. **62**, 1181 (1999).

[6] R. A. Spits, *Dynamical Behaviour of Implanted Ions in Diamond*, Master's thesis, University of the Witwatersrand, School of Physics, 1990.

[7] J. W. Mayer, L. Eriksson, and J. A. Davies, *Ion Implantation in Semiconductors*, Academic Press Inc., New York, 1970.

[8] P. Sigmund, *Stopping powers in perspective*, Nucl. Instr. and Meth. B **135**, 1 (1998).

[9] P. D. Townsend, J. C. Kelly, and N. E. W. Hartley, *Ion Implantation Sputtering and their Applications*, Academic Press Inc., 1976.

[10] J. F. Ziegler, *Ion Implantation Physics*, in *Handbook of Ion Implantation*, edited by J. F. Ziegler, chapter 1, pages 1–68, North Holland, 1992.

[11] J. Gyulai, *Radiation Damage and Annealing in Ion Implantation*, in *Handbook of Ion Implantation*, edited by J. F. Ziegler, chapter 2, pages 69–118, North Holland, 1992.

[12] J. F. Prins, *Ion implantation of diamond for electronic applications*, Semicon. Sci. Technol. **18**, S27 (2003).

[13] J. F. Prins, *Modification, Doping and Devices in Implanted Diamond*, in *Properties of Natural and Synthetic Diamond*, edited by J. Field, chaper 8, pages 301–341, Academic Press Limited, 1992.

[14] R. A. Spits, T. E. Derry, J. F. Prins, and J. P. F. Sellschop, *Depth profiling of implanted ^{13}C in diamond as a function of implantation temperature*, Nucl. Instr. and Meth. B **51**, 247 (1990).

[15] S. O. Kucheyev, J. S. Williams, and S. J. Pearton, *Ion implantation into GaN*, Mater. Sci. Eng. R. **33**, 51 (2001).

[16] T. E. Derry, R. A. Spits, and J. P. F. Sellschop, *Ion beam studies of the static and dynamic properties of dopants in diamond*, Mater. Sci. Eng. B **11**, 249 (1992).

[17] S. O. Kucheyev, *Ion-Beam Processes in Group III-Nitride*, PhD thesis, Australian National University, Research School of Physical Sciences and Engineering, 2002.

[18] C. Ronning, E. P. Carlson, and R. F. Davis, *II into GaN*, Phys. Rep. **351**, 349 (2001).

[19] J. F. Prins, T. E. Derry, and J. P. F. Sellschop, *Volume expansion of diamond during ion implantation*, Phys Rev. B **34**, 8870 (1986).

[20] R. Simonton and F. Sinclair, *Channelling Effects in Ion Implantation*, in *Handbook of Ion Implantation*, edited by J. F. Ziegler, chapter 3, pages 119–221, North Holland, 1992.

[21] M. L. Swanson, *The study of lattice defects by channelling*, Rep. Prog. Phys. **45**, 47 (1983).

[22] R. C. DeVries, *General Electric Company Corporate Research and Development Report No. 72CRD178*, 1972.

[23] S. N. Tkachev, V. L. Solozhenko, P. V. Zinin, M. H. Manghanani, and L. C. Ming, *Elastic moduli of the superhard cubic BC_2N by Brillouin scattering*, Phys. Rev. B **68**, 052104 (2003).

[24] J. H. Edgar, *Crystal Structure, Mechanical Properties and Thermal Properties of BN*, in *Properties of Group III Nitrides*, edited by J. H. Edgar, chapter 1.2, pages 7–21, INSPEC, The Institution of Electrical Engineers, London, United Kingdom, 1994.

[25] V. L. Solozhenko, *Synthesis of Superhard Phases (In Situ Studies)*, in *High-Pressure Crystallography*, edited by A. Katrusiak and P. McMillan, pages 411–428, Kluwer Academic Publishers, Netherlands, 2004.

[26] A. V. Kanaev, J. P. Petitet, L. Museur, V. Marine, V. L. Solozhenko, and V. Zafiropulos, *Femtosecond and ultraviolet laser irradiation of graphite-like hexagonal boron nitride*, J. Appl. Phy. **96**, 4483 (2004).

[27] L. Liu, Y. P. Feng, and Z. X. Shen, *Structural and electronic properties of hBN*, Phys. Rev. B **68**, 104102.1 (2003).

[28] L. Vel, G. Demazeau, and J. Etourneau, *Cubic boron nitride: synthesis, physiochemical properties and applications*, Mater. Sci. Eng. B **10**, 149 (1991).

[29] J. Y. Huang, H. Yasuda, and H. Mori, *HRTEM and EELS studies on the amorphization of hexagonal boron nitride induced by ball milling*, J. Am. Ceram. Soc. **83**, 403409 (2000).

[30] P. B. Mirkarimi, K. F. McCarty, and D. L. Merlin, *Review of advances in cubic boron nitride film synthesis*, Mater. Sci. Eng. R **21**, 47 (1997).

[31] V. L. Solozhenko, *New concept of BN phase diagram: an applied aspect*, Diamond Relat. Mater. **4**, 1 (1994).

[32] V. L. Solozhenko, *Current trends in the phase of boron nitride*, J. Hard Mater. **6**, 51 (1995).

[33] V. L. Solozhenko, *Phase diagram of boron nitride*, Doklady Phys. Chem **301**, 592 (1988).

[34] V. Z. Turkevich, *Phase diagrams and synthesis of cubic boron nitride*, J. Phys.: Condens. Mater **14**, 1096310968 (2002).

[35] V. L. Solozhenko, A. G. Lazarenko, J. P. Petitet, and A. V. Kanaev, *Bang gap energy of graphite-like hexagonal boron nitride*, J. Phys. Chem. Solids **62**, 1331 (2001).

[36] V. L. Solozhenko, *Wide Band Gap Electronic Materials,* in *Thermodynamic Properties of Boron Nitride*, pages 377–392, Kluwer Academic Publishers, 1995.

[37] T. E. Mosuang, *Defects and Defect Processes in Some Ultra-Hard Nitride*, PhD thesis, University of the Witwatersrand, School of Physics, 2003.

[38] T. E. Mosuang and J. E. Lowther, *Relative stability of cubic and different hexagonal forms of boron nitride,* J. Phys. Chem. Solids **63**, 363 (2002).

[39] K. T. Park, K. Terakura, and N. Hamada, *Band-structure calculations for boron nitrides with three different crystal structures,* J. Phys. C.: Solid State Phys. **20**, 1241 (1987).

[40] J. H. Edgar, *Common Crystal Structures of Group III–Nitrides,* in *Properties of Group III Nitrides*, edited by J. H. Edgar, chapter 1.1, pages 3–6, INSPEC, The Institution of Electrical Engineers, London, United Kingdom, 1994.

[41] B. P. Singh, V. L. Solozhenko, and G. Will, *On the low-pressure synthesis of cubic boron nitride,* Diamond Relat. Mater. **4**, 1193 (1995).

[42] G. Will, G. Nover, and J. von der Gonna, *New experimental results on the phase diagram of boron nitride,* J. Solid State Chem. **154**, 280 (2000).

[43] G. J. Ackland, *High-pressure phases of group IV and III-V semiconductors,* Rep. Prog. Phys. **64**, 483 (2001).

[44] A. O. Sezer and J. I. Brand, *Chemical vapor deposition of boron carbide,* Mater. Sci. Eng. B **79**, 191 (2001).

[45] V. L. Solozhenko, G. Will, and F. Elf, *Isothermal compression of hexagonal graphite – like boron nitride up to 12GPa,* Solid State Comm. **96**, 1 (1995).

[46] V. L. Solozhenko, S. N. Dub, and N. Novikov, *Mechanical properties of cubic BC_2N a new superhard phase,* Diamond Relat. Mater. **10**, 2228 (2001).

[47] I. Bello, C. Y. Chan, W. J. Zhand, Y. M. Chong, K. M. Leung, S. T. Lee, and Y. Lifshitz, *Deposition of thick cubic boron nitride films: The route to practical applications,* Diamond Relat. Mater. **14**, 1154 (2005).

[48] D. A. Lelonis, *Boron nitride powder – a review*, General Electrics: Advanced Ceramics, USA, 2003 (see also www.advceramics.com).

[49] J. Huang and Y. T. Zhu, *Advances in the synthesis and characterization of boron nitride*, Defect and Diffusion Forum **186-7**, 1 (2000).

[50] A. V. Kurdyumov, V. F. Britun, and I. A. Petrusha, *Structural mechanisms of rhombohedral BN transformations into diamond-like phases*, Diamond Relat. Mater. **5**, 1229 (1996).

[51] V. F. Britun and A. V. Kurdyumov, *Crystal defect generation during diffusionless transformations of boron nitride by puckering mechanism*, J.Mater. Sci. **34**, 5677 (1999).

[52] D. Demazeau, *High pressure in solid-state chemistry*, J. Phys. C.: Condens. Mater **14**, 11031 (2002).

[53] S. K. Singhal, J. von der Gonna, G. Nover, H. J. Meurer, and B. P. Singh, *Synthesis of cubic boron nitride at reduced pressures in the presence of* $Co[(NH_3)_6]Cl_3$ *and* NH_4F, Diamond Relat. Mater. **14**, 1389 1394 (2005).

[54] R. Smoluchowski, *Phase Transformation in Solids*, in *Handbook of Physics*, edited by A. U. Condon and O. Odishaw, pages 8–105, McGraw-Hill Book Co., London, 1967.

[55] E. Vlodarchic and R. Trebinski, *Transformations of graphite and boron nitride in shock waves*, Shock Waves **7**, 231 (1997).

[56] J. F. Ziegler, *SRIM-2003*, Nucl. Instr. and Meth. B: – Proceedings of the Sixteenth International Conference on Ion Beam Analysis, June 2004 **219-220**, 1027 (2004), See also the SRIM 2003 website – http://www.srim.org.

[57] D. B. Rebuli, *Oxygen on diamond surfaces*, Master's thesis, University of the Witwatersrand, School of Physics, 1999.

[58] D. B. Rebuli, *Electron emission in charged particle interactions with diamond surfaces*, PhD thesis, University of the Witwatersrand, School of Physics, 2003.

[59] C. G. Smallman, *Lattice Site Location And Migration Of Implanted Fluorine In Diamond*, Master's thesis, University of the Witwatersrand, School of Physics, 1992.

[60] D. A. Long, *Raman Spectroscopy*, McGraw-Hill, 1977.

[61] T. Erdogan and V. Mizrahi, *Thin-Film Filters for Raman Spectroscopy*, Spectroscopy **19**, 113 (2004).

[62] S. Nakashima, *Raman imaging of semiconductor materials: characterization of static and dynamic properties*, J. Phys.: Condens. Mater **16**, S25S37 (2004).

[63] J. I. Langford and D. Louer, *Powder diffraction*, Rep. Prog. Phys **69**, 131234 (1996).

[64] M. Birkholz, *Thin Film Analysis by X-Ray Scattering*, J. Wiley and Sons, 2005.

[65] M. Prutton, *Introduction to Surface Physics*, Oxford Science Publication, 1994.

[66] R. D. Tarey, R. S. Rastogi, and K. L. Chopra, *Characterization of thin films by grazing incidence X-ray diffraction*, The Rigaku Journal **4**, 11 (1987).

[67] P. Dutta, *Grazing incidence X-ray diffraction*, Current Science **78**, 1478 (2000).

[68] P. R. Stoddart, *Surface Brillouin Scattering Studies of High-Temperature Elasticity*, PhD thesis, University of the Witwatersrand, School of Physics, 1999.

[69] A. S. Pine, *Brillouin Scattering in Semiconductors*, in *Light Scattering in Solids*, edited by M. Cardona, Topics in Applied Physics, pages 253–273, Academic Press, 1975.

[70] K. E. Rammutla, *Light Scattering and Computational Studies on Superionic Compounds*, PhD thesis, University of the Witwatersrand, School of Physics, 2001.

[71] J. I. Goldstein, D. E. Newbury, P. Echlin, D. C. Joy, C. Fiori, and E. Lifchin, *Scanning Electron Microscopy and X-Ray Microanalysis*, Plenun Press - New York, 1981.

[72] G. R. Booker, *The Instrument in Modern Diffraction and Imaging Techniques in Material Science*, in *Scanning Electron Microscopy*, edited by S. Amelinckx et. al., Proceedings of the International Summer Course on Material science - 1969, North-Holland Publishing Company, Antwerp, Belgium, 1970.

[73] G. R. Booker, *Applications in Modern Diffraction and Imaging Techniques in Material Science*, in *Scanning Electron Microscopy*, edited by S. Amelinckx et. al., Proceedings of the International Summer Course on Material science - 1969, North-Holland Publishing Company, Antwerp, Belgium, 1970.

[74] *PDF-2 database 01-073-2095*.

[75] R. Erasmus, *Personal communication*, 2005.

[76] P. V. Huong, *Structural studies of diamond films and ultra hard materials by Raman and micro-Raman spectroscopies*, Diamond Relat. Mater. **1**, 33 (1991).

[77] H. Sachdev, R. Haubner, H. Noth, and B. Lux, *Investigation of the c-BN/h-BN phase transformation at normal pressure*, Diamond Relat. Mater. **6**, 286 (1997).

[78] T. Werninghaus, J. Hahn, F. Ritcher, and D. R. T. Zahn, *Raman spectroscopy investigation size effects in cubic boron nitride*, Appl. Phys. Lett. **70**, 958 (1997).

[79] R. J. Nemanich, S. A. Aolin, and R. M. Martin, *Light scattering in boron nitride microcrystals*, Phys. Rev. B **23**, 6348 (1981).

[80] H. Sachdev, *Influence of impurities on the morphology and Raman spectra of cubic boron nitride*, Diamond Relat. Mater. **12**, 1275 (2003).

[81] J. Liu, Y. K. Vohra, J. T. Tarvin, and S. S. Vagarali, *Cubic-to-rhombohedral transformation in boron nitride induced by laser heating: in situ Raman-spectroscopy studies*, Phys. Rev. B **51**, 8591 (1995).

[82] P. Parayanthal and F. H. Pollak, *Raman scattering in alloy semiconductors: Spatial Correlation Model*, Phys. Rev. Lett. **52**, 1822 (1984).

[83] H. Herchen and M. A. Cappelli, *Temperature dependence of the cubic boron nitride Raman lines*, Phys. Rev. B **23**, 6348 (1981).

[84] *PDF-2 database 01-085-1*.

[85] R. Erasmus, *CMRE: Material Characterisation Course – Optical Methods for Materials Characterisation*, Course Notes, 2003.

[86] S. Ndiaye, *Introduction to the Fundamentals of Raman Scattering*, Course Notes, 2004.

[87] D. W. Ball, *Theory of Raman spectroscopy*, Spectroscopy **32**, 16 (2001).